

DESIGN OF INTEGRATED GASIFIER AND STEAM METHANE REFORMER

**MODELLING, SIMULATION AND DESIGN OF
AN INTEGRATED GASIFIER AND STEAM
METHANE REFORMER FOR
POLYGENERATION**

By
JAFFER GHOUSE, B. TECH.

*Submitted to the School of Graduate Studies
in partial fulfillment of the requirements for the degree of
Doctor of Philosophy*

McMASTER UNIVERSITY

© Copyright by Jaffer Ghouse, May 2016

TITLE: Modelling, Simulation and Design of an Integrated Gasifier
and Steam Methane Reformer for Polygeneration

AUTHOR: Jaffer Ghouse, B.Tech.

Anna University, Chennai, India

DEGREE: Doctor of Philosophy (2016), Chemical Engineering

SUPERVISOR: Dr. Thomas A. Adams II

NUMBER OF PAGES: 154

*Dedicated to my parents, Farida and Ghouse, for their unconditional love,
encouragement and support*

ABSTRACT

While the quest of the human civilization continues towards a more sustainable energy resource, current energy conversion technologies need to be improved such that the rate of environmental impact that has occurred due to the rapid industrialization since the 20th century is mitigated. This search has motivated research into new energy conversion technologies that aim to reduce the environmental impact by either improving the efficiencies of existing technologies, developing new technologies with zero emissions or by improving reliability and reducing the cost of renewable energy. Process intensification through process integration is one of the areas of active research that improves the system efficiency by exploiting the synergies that exist between different processes. This thesis considers the design and operational feasibility of heat integrating two conventional industrial processes – gasification and steam reforming of methane for application in polygeneration. To this end, complex mathematical models that describe the integrated system are developed to study different design prospects and to determine if the device can be safely operated in a plant producing electricity, liquid fuels and hydrogen. The designs proposed in this thesis show that significant methane conversion comparable to industrial reformers can be achieved while providing the required cooling duty to the gasifier. The proposed integrated system produces hydrogen rich reformer synthesis gas (hydrogen and carbon monoxide) that can be blended with the hydrogen lean coal synthesis gas providing flexibility to change the molar H₂/CO ratio necessary for different downstream processes in a polygeneration plant. Moreover, the results show that the integration helps improve plant carbon efficiency and reduce CO₂ emissions. The major contribution of this thesis is the development of designs based on representative mathematical models that are safe to operate for producing several chemicals in polygeneration plants.

ACKNOWLEDGEMENTS

In my arduous but intellectually fulfilling journey of five years in graduate school, I am grateful to several remarkable individuals in my life that have made this thesis a reality. First and foremost, I owe my sincerest gratitude to my supervisor, Dr. Thomas A. Adams II. If it weren't for his encouragement and motivation, I would have been writing this section as part of a Master's thesis. Dr. Adams has constantly helped me with his excellent guidance to scale heights that I deemed to be impossible. He will always remain one of the most inspiring people with whom I have had the fortune to work with and who would have contributed to whatever success I achieve in my life ahead.

I would like to thank my committee members, Dr. Vladimir Mahalec and Dr. Marlyn Lightstone, for their insightful questions and suggestions that have only improved the quality of this work. To the department staff over the years – Kathy Goodram, Melissa Vasil, Lynn Falkiner, Cathie Roberts, Michelle Whalen and Kristina Trollip – I am thankful for their patience when assisting with applications for financial awards and graduate school formalities.

I would also like to thank all my teachers from kindergarten to my Ph.D. degree who have nurtured and shaped my intellectual capacity.

One of the most rewarding experiences during my Ph.D. has been the opportunity to meet, know and be inspired by brilliant people from Canada and around the globe. The following people deserve special mention: Jake Nease, Alicia Pascall, Yaser Khojasteh, Chinedu Okoli, Brandon Corbett, Kushlani Wijesekera, Vida Meidenshahi, Zhiwen Chong, Yanan Cao, Ian Washington, Pedro Castillo, Shailesh Patel and Mudassir Rashid. To my friends from India: Prem Ramanujam, Deepak Kumarappa, Yogesh Chinta, Smriti Shyamal, and Abhinav Garg – thank you for being my home away from home.

I reserve my gratitude to a very special and important person to the last, my mother. She has overcome several hardships and made numerous sacrifices as a single parent for the past seventeen years in helping me reach where I am today. She truly has been a testament to the adage – *“Behind every successful man, there is a woman”*.

I would also like to remember my late father at this juncture who was my inspiration to be a Chemical Engineer and whose values continue to guide me even in his absence.

Thank You!

TABLE OF CONTENTS

ABSTRACT.....	v
ACKNOWLEDGEMENTS.....	vii
TABLE OF CONTENTS.....	viii
LIST OF FIGURES	xii
LIST OF TABLES.....	xv
RESEARCH CONTRIBUTIONS	xvi
CHAPTER 1	1
1.1 Energy Mix in the Coming Decades	2
1.2 Key Technologies	2
1.2.1 Gasification.....	2
1.2.2 Steam Reforming of Methane.....	4
1.2.3 Polygeneration	4
1.3 Motivation for the Proposed Integrated Design.....	5
1.4 Research Objectives.....	6
1.5 Thesis Structure	7
1.6 References.....	8
CHAPTER 2	10
2.1 Introduction.....	11
2.2 Model Development.....	13
2.2.1 Gas Phase Mass Balance.....	15
2.2.2 Gas Phase Momentum Balance.....	15
2.2.3 Gas Phase Energy Balance.....	16
2.2.4 Gas Phase Boundary Conditions.....	17
2.2.5 Gas Phase Correlations	17
2.2.6 Catalyst Phase Mass Balance.....	18
2.2.7 Catalyst Phase Energy Balance.....	19
2.2.8 Catalyst Phase Boundary Conditions.....	20

2.2.9 Tube Wall Model	20
2.2.10 SMR Kinetics	21
2.2.11 Simulation Strategy	23
2.3 Model Validation	23
2.4 Results and Discussion	26
2.4.1 Dynamic Simulation Using Case 1 for Tube Wall Model	26
2.4.2 Dynamic Simulation Using Case 2 for Tube Wall Model	27
2.4.3 Effect of Feed Disturbance	30
2.5 Conclusions.....	35
2.6 Acknowledgements.....	35
2.7 Nomenclature	36
2.8 References.....	41
CHAPTER 3	44
3.1 Introduction.....	45
3.2 Materials and Methods.....	47
3.2.1 RSC Shell Model Description.....	48
3.2.2 Shell Gas Phase Mass Balance.....	48
3.2.3 Shell Gas Phase Energy Balance	49
3.2.4 SMR Model.....	51
3.2.5 Tube Wall Model	51
3.2.6 Tube Wall Boundary Conditions	51
3.2.7 Refractory Model	52
3.2.8 Refractory Boundary Conditions	53
3.3 Model Validation for Independent Systems.....	54
3.4 Determination of Design Parameters for the Hybrid System.....	57
3.5 Numerical Analysis and Grid Independence Test.....	58
3.6 Results and Discussion	60
3.6.1 Performance of Co-current and Counter-current Configurations	60
3.6.2 Other Design Options	65
3.6.3 Sensitivity Analysis on Performance	66

3.7 Conclusions.....	68
3.8 Acknowledgements.....	69
3.9 Nomenclature.....	69
3.10 References.....	72
CHAPTER 4	77
4.1 Introduction.....	78
4.2 Flexibility in Syngas Yield and H ₂ /CO ratio at Steady-state	80
4.3 From Steady-state to Dynamic Simulations.....	82
4.4 Changes to Tube Side Variables	83
4.4.1 Effect of Feed Inlet Temperature	83
4.4.2 Operating at a Lower Steam to Carbon Ratio	86
4.4.3 Operating the Reformer at Reduced Capacity	89
4.5 Changes to Shell Side Variables	92
4.5.1 Fluctuations in Gasifier Exit Temperature	92
4.5.2 Disturbance in the Gasifier Syngas Flowrates	95
4.5.3 Step Decrease in Gasifier Feed (50% drop).....	96
4.6 Open Loop Start-up of the Co-current Configuration.....	98
4.7 Conclusions.....	103
4.8 Acknowledgements.....	104
4.9 References.....	105
CHAPTER 5	107
5.1 Extension of the integrated design to a biomass gasifier	108
5.2 The Need for Optimal Designs	108
5.2.1 Estimating the Capital Cost	110
5.2.2 Deterministic Optimisation Using gPROMS	111
5.2.3 Implementation of Meta-heuristic Programming on gPROMS Models	112
5.2.4 Optimization Results using NLP Solver in gPROMS.....	113
5.2.5 Optimization Results using Meta-Heuristic Algorithms – DE and PSO	114
5.2.6 Effect of Compact Designs on Performance.....	115
5.3 Conclusions.....	118

5.4 References.....	119
CHAPTER 6	120
6.1 Conclusions.....	121
6.2 Recommended Future Work	123
6.3 References.....	125
APPENDIX.....	126

LIST OF FIGURES

Figure 1: Different potential uses of the proposed integrated system in a polygeneration plant	6
Figure 2: Key temporal and spatial variables considered in the proposed multi-scale SMR model	14
Figure 3: Comparison of percentage conversion of CH ₄ and H ₂ mole fraction at exit (dry basis) between reported values and the proposed model prediction (case 1).....	24
Figure 4: Comparison of percentage conversion of CH ₄ and H ₂ mole fraction at exit (dry basis) between reported values and model prediction (case 2 with T _{w,o} = 1200 K and T _{w,o} = 1150 K)...	26
Figure 5: Dynamic profiles for gas phase mole fractions at the exit(left), and core catalyst temperature and temperature difference between catalyst core and gas phase ($\Delta T = T_{cat} - T_{gas}$) at selected points down the length of the reactor (expressed as the axial distance Z divided by the reactor length L) for case 1	27
Figure 6: Dynamic profiles for catalyst core temperature, temperature difference between the catalyst core and the gas phase ($\Delta T = T_{cat} - T_{gas}$) and temperature of tube inner wall at selected points down the length of the reactor (expressed as the axial distance Z divided by the reactor length L) for case 2.....	28
Figure 7: Steady state profiles for the temperature of the tube inner wall and the temperature difference between the outer wall and inner wall of the tube for case 2 ($\Delta T = T_{w,o} - T_{w,i}$).....	29
Figure 8: Dynamic profiles for concentration of CH ₄ and temperature in the catalyst pellet at an axial distance of 6 m for case 2.....	30
Figure 9: The difference in methane conversion (ΔX_{CH_4}) and inner tube wall temperature ($\Delta T_{w,i}$) between new and previous steady state values for a step increase in feed temperature by 100 K.	31
Figure 10: Dynamic profiles for catalyst core and tube inner wall temperature at various axial positions for a step increase in inlet feed temperature by 100 K at t=900 s	32
Figure 11: The difference in methane conversion (ΔX_{CH_4}) and inner tube wall temperature ($\Delta T_{w,i}$) between new and previous steady state values for a step decrease in feed molar flow rate by 50%	33
Figure 12: Dynamic profiles for catalyst core and tube inner wall temperature at various axial positions for a step decrease in inlet feed molar flow rate by 50% at t=900s.....	33
Figure 13: Dynamic profiles for mole fraction (CH ₄ , CO, CO ₂) at the exit, catalyst core temperature and the inner tube wall temperature for a trip in inlet steam supply for 60s from t=900s to t=960s.....	34
Figure 14: Proposed concept of integrating RSC of an entrained-bed gasifier with SMR	47
Figure 15: RSC model validation using data sets 1 and 2	56

Figure 16: Placement of tubes within the RSC shell	58
Figure 17: Determination of the optimal numerical grid size	60
Figure 18: Axial profiles of gas temperature and conversion in co-current and counter-current configuration	62
Figure 19: Axial profiles of refractory temperature, outer tube wall temperature and heat flux through tube wall for co-current and counter-current configuration	63
Figure 20: Sensitivity analysis for co-current configuration.....	68
Figure 21: Syngas yields with different H ₂ /CO ratios for co-current configuration.....	81
Figure 22: Syngas yields with different H ₂ /CO ratios for counter-current configuration.....	81
Figure 23: Effect of step change of both +50 K and -50 K in inlet temperature for co-current configuration on (a) exit gas temperature leaving the tube and shell, (b) axial tube wall temperature, (c) catalyst core temperature at the inlet, exit, and halfway point and (d) axial methane conversion	84
Figure 24: Effect of step change of both +50 K and -50 K in inlet temperature for counter-current configuration on (a) exit gas temperature leaving the tube and shell, (b) axial tube wall temperature, (c) catalyst core temperature at the inlet, exit, and halfway point and (d) axial methane conversion	85
Figure 25: Effect of 50% reduction in inlet steam supply for co-current configuration on (a) exit gas temperature leaving the tube and shell, (b) tube wall temperature at the inlet, exit, and halfway point, (c) catalyst core temperature at the inlet, exit, and halfway point and (d) axial methane conversion.....	87
Figure 26: Effect of 50% reduction in inlet steam supply for counter-current configuration on (a) exit gas temperature leaving the tube and shell, (b) tube wall temperature at the inlet, exit, and halfway point, (c) catalyst core temperature at the inlet, exit, and halfway point and (d) axial methane conversion	88
Figure 27: Effect of step decrease in total SMR feed by 25% for co-current configuration on (a) exit gas temperature leaving the tube and shell, (b) tube wall temperature at the inlet, exit, and halfway point, (c) catalyst core temperature at the inlet, exit, and halfway point and (d) axial methane conversion	90
Figure 28: Effect of reduced SMR feed on syngas yield and H ₂ /CO ratio for co-current configuration.....	91
Figure 29: Effect of step decrease in total SMR feed by 25% for counter-current configuration on (a) exit gas temperature leaving the tube and shell, (b) tube wall temperature at the inlet, exit, and halfway point, (c) catalyst core temperature at the inlet, exit, and halfway point and (d) axial methane conversion	91
Figure 30: Effect of +25 K disturbance in inlet shell temperature for 300s in co-current configuration on (a) tube gas temperature at different axial points, (b) exit shell gas temperature, (c) tube wall temperature at the inlet, exit, and halfway point, (d) catalyst core temperature at the inlet, exit, and halfway point, (e) exit tube syngas mole fraction and (f) exit shell syngas mole fraction.....	93

Figure 31: Effect of +25 K disturbance in inlet shell temperature for 300s in counter-current configuration on (a) tube gas temperature at different axial points, (b) exit shell gas temperature, (c) tube wall temperature at the inlet, exit, and halfway point, (d) catalyst core temperature at the inlet, exit, and halfway point, (e) exit tube syngas mole fraction and (f) exit shell syngas mole fraction	94
Figure 32: Effect of 5% disturbance in inlet shell flow rate for 300s in co-current configuration on (a) exit gas temperature leaving the tube and shell, (b) tube wall temperature at the inlet, exit, and halfway point, (c) catalyst core temperature at the inlet, exit, and halfway point and (d) tube side exit syngas mole fraction	95
Figure 33: Effect of 5% disturbance in inlet shell flow rate for 300s in counter-current configuration on (a) exit gas temperature leaving the tube and shell, (b) tube wall temperature at the inlet, exit, and halfway point, (c) catalyst core temperature at the inlet, exit, and halfway point and (d) tube side exit syngas mole fraction.....	96
Figure 34: Effect of step decrease in coal-derived syngas feed by 50% for co-current configuration on (a) exit gas temperature leaving the tube and shell, (b) tube wall temperature at the inlet, exit, and halfway point, (c) catalyst core temperature at the inlet, exit, and halfway point and (d) axial methane conversion	97
Figure 35: Effect of step decrease in coal-derived syngas feed by 50% for counter-current configuration on (a) exit gas temperature leaving the tube and shell, (b) tube wall temperature at the inlet, exit, and halfway point, (c) catalyst core temperature at the inlet, exit, and halfway point and (d) axial methane conversion	98
Figure 36: Shell gas and reformer gas temperature profiles during start-up.....	101
Figure 37: Tube gas mole fraction profiles at reformer exit during start-up.....	102
Figure 38: Catalyst core temperature profiles along the reformer tubes during start-up	102
Figure 39: Maximum tube wall temperature profile during start-up	103
Figure 40: Design variables for the proposed co-current integrated RSC-SMR design	109
Figure 41: Meta-heuristic programming implementation on a gPROMS model.....	112
Figure 42: Effect of parallel computing on wall clock time	113
Figure 43: Effect of tube diameter on (A) tube gas phase pressure, (B) tube gas phase Reynolds number, (C) heat transferred from gas to catalyst and (D) mass transfer coefficient of CH ₄ from gas to catalyst.....	117
Figure 44: Effect of RSC diameter on (A) tube gas phase pressure, (B) tube gas phase Reynolds number, (C) heat transferred from gas to catalyst and (D) mass transfer coefficient of CH ₄ from gas to catalyst.....	118

LIST OF TABLES

Table 1: Different gasifier types with corresponding operating characteristics.....	3
Table 2: Model validation reference for feed conditions and parameters.....	25
Table 3: Available RSC shell dimensions.....	55
Table 4: Operating conditions for integrated RSC-SMR system.....	61
Table 5: Co-current performance with different SMR tube thickness and length	65
Table 6: Feed and production capacity at steady-state for co-current and counter-current designs	80
Table 7: Base-case design parameters for an integrated SMR and biomass gasifier	108
Table 8: Lower and upper bounds for the design parameters	111
Table 9: Optimal solutions using NLP solver in gPROMS	114
Table 10: Optimal solutions of the high-conversion scenario using DE and PSO	115
Table 11: Effect of tube diameter on design and operating parameters.....	116
Table 12: Effect of RSC diameter on design and operating parameters	117

RESEARCH CONTRIBUTIONS

- Developed a dynamic, multi-scale, heterogeneous model for catalytic steam methane reforming reactors that allows for particle level tracking in concentration and temperature without using a catalyst specific effectiveness factor – a first for steam methane reforming models. The pure first-principles model was validated with industrial data without the need to estimate any model parameters.
- Developed a dynamic and distributed model for the radiant syngas cooler of an entrained-bed gasifier and coupled it with the reforming model to simulate and study the performance of a novel integrated gasifier and steam methane reformer. The model was implemented and simulated in gPROMS.
- Established base-case designs for the proposed integrated coal-based system for two different flow configurations; co-current and counter-current. The designs allow for a minimum methane conversion of 80% and satisfy the cooling requirements of an entrained-bed gasifier without violating any operating constraints. A sensitivity analysis was done to understand the effect of model parameters and assumptions on system performance.
- Analyzed the dynamic operability of the integrated system under open-loop to identify limitations of the design for flexible polygeneration.
- Design heuristics that were established in this work were utilised to extend the integrated design to a biomass based gasifier.
- A procedure to find optimal designs was established by applying both deterministic and stochastic techniques.

CHAPTER 1

Introduction

1.1 Energy Mix in the Coming Decades

The demand for energy in the world has only grown since the industrial revolution and will continue to grow with increasing world population in the coming years. It is estimated that the world population will grow to 8.5 billion in 2030 from the present 7.3 billion [1] – an increase of 16% in fourteen years. BP’s energy outlook [2] predicts that the global demand for energy will grow by 34% by the year 2035. A similar conclusion is also provided by the International Energy Agency in its energy outlook report where the energy demand is projected to grow by 33% by the year 2040 [3]. It is projected that the fossil fuel triumvirate of oil, coal and gas will contribute around 80% to the entire energy mix in 2035 with gas being the fastest growing fuel growing at a rate of 1.8% per annum [2]. Though the share of renewables in the energy mix is projected to grow, the growth of non-OECD economies, especially India and China, will help maintain the position of fossil fuels as the major energy source. This projected growth will invariably impact the combined efforts of countries around the globe to curtail the associated carbon emissions. To meet the International Energy Agency’s (IEA) target of reducing CO₂ emissions such that the change in global average temperature is limited to 2°C by the year 2050 [4], new technologies will have to be developed that utilise the fossil fuels more efficiently with reduced emissions compared to the status quo.

1.2 Key Technologies

Three key technologies are pertinent to this work – Gasification, Steam Reforming of Methane and Polygeneration. In the following sections, a brief introduction about each of these technologies is presented. It should be noted that there might be a possible overlap in the descriptions provided with the introduction sections of subsequent chapters owing to the “sandwich” format of this thesis.

1.2.1 Gasification

Gasification is the process of converting carbon based solid fossil fuels in the presence of limited oxygen and steam to a mixture of products containing hydrogen, carbon monoxide, carbon dioxide, hydrocarbons, volatiles and slag. The history of gasification dates back to the production of town gas in the early nineteenth century that was utilised for lighting purposes [5]. Modern industrial applications of gasification began with the production of synthesis gas, a mixture of hydrogen and carbon monoxide, that was used in the production of synthetic ammonia in Germany [5]. Today, synthesis gas derived

from gasification is used for electricity generation, liquid fuels and chemicals production, and as a source of hydrogen. The solid fossil feedstock to gasification can be coal, biomass, petroleum or oil sands coke, waste (municipal solid waste) or a combination of any of these resources. Of the afore-mentioned feedstock options, coal has been a dominant option owing to its abundant availability and prior process knowledge. Based on the type of feed, the characteristics of the product synthesis gas change. For example, the synthesis gas H₂/CO molar ratio ranges from 0.75-1.1 depending upon coal/biomass feed [6], which generally needs to be upgraded to a higher H₂/CO ratio depending on the application (for example, Fischer-Tropsch (FT) synthesis requires a feed ratio of 2 [6]). Coal gasification is an integral part of the power generation industry in the form of Integrated Coal Gasification Combined Cycle (IGCC) [7]. Also, coal gasification is used in the production of liquid fuels via Fischer-Tropsch synthesis route and speciality chemicals like dimethyl ether, methanol, formaldehyde, oxo-alcohols and mono-ethylene glycols [5]. The FT synthesis, which had its origins during the Second World War to produce liquid fuels from coal when access to crude oil was limited to Germany [8] has grown ever since and is currently used at the industrial scale efficiently to produce liquid fuels at Sasol in South Africa from 1955 and of late in China [5], [8]. Gasifier reactors are classified on the basis of fluid flow and bed type as Fluidized Bed (FB), Entrained Bed (EB) and Moving Bed (MB) gasifiers. Each of these gasifiers differs in their operating conditions, feedstock acceptability and carbon conversion. A brief description on the key operating characteristics of each along with some commercially operating gasifiers are listed and compared in Table 1[5].

Table 1: Different gasifier types with corresponding operating characteristics

Operating characteristic	Fluidized Bed	Moving Bed	Entrained Bed
Description	Well stirred reactor with coal particles fluidized by oxygen/air	Counter-current flow where coal is heated by hot gases flowing upwards	Co-current flow of coal and oxygen/air
Gas temperature	900-1050°C	450-650°C	1250-1600°C
Coal feed location	Top	Top	Top
Oxygen/Air feed location	Bottom	Bottom	Top
Oxidant requirement	Moderate	Low	High
Steam requirement	Moderate	Low	Low
Carbon conversion	Low	Low	High
Acceptability of fines	Good	Limited	Unlimited
Ash conditions	Dry/Agglomerating	Dry/Slagging	Slagging
Commercial gasifiers	CFB, TRIG, U-Gas, HTW, Winkler	Lurgi, SEDIN, BGL	Shell, GE, Siemens, KT

1.2.2 Steam Reforming of Methane

An alternative but prominent route for producing synthesis gas is via steam reforming of hydrocarbons. A variety of hydrocarbons can be used, but methane is the preferred feedstock in most of the hydrogen production facilities in the world [9]. Steam reforming of methane is an endothermic catalytic process where the heat required is supplied by combustion of fuel to the reactant gases (steam and methane) within multiple tubes placed inside a furnace that are called Steam Methane Reformers (SMR). Unlike coal-derived synthesis gas, the product synthesis gas from the reforming process has a higher molar H_2/CO ratio [10]. The high molar H_2/CO ratio is an advantage for standalone hydrogen production but also a disadvantage when it is used as a feed for liquid fuels production in FT synthesis which requires an inlet H_2/CO ratio of only 2. Therefore, autothermal reforming is preferred for such applications where the product H_2/CO ratio is typically in that range. However, the autothermal reformers require high purity oxygen necessitating the need to have an air separation unit on site which is capital intensive.

1.2.3 Polygeneration

The growing need to achieve energy independence amid fluctuating market conditions has motivated research into new type of plants called polygeneration plants. Adams and Ghose [11] define polygeneration as “a thermochemical process which simultaneously produces at least two different products in non-trivial quantities, but is not a petroleum refining process, a co-generation process, or a tri-generation process, and at least one product is a chemical or fuel, and at least one is electricity”. Polygeneration plants provide flexibility amid fluctuating market conditions through a diverse product portfolio that consists of electricity, hydrogen, synthetic fuels and speciality chemicals. Even though a polygeneration plant produces different products, the raw material for all the products is synthesis gas. As explained previously, the synthesis gas molar composition requirement varies with different types of processes. The coal/bio-mass derived synthesis gas is therefore upgraded either by water gas shift reactions or blended with hydrogen rich synthesis gas from reforming reactions from an external SMR or an autothermal reformer. To make these polygeneration plants highly efficient and reliable, there is a need to look at new technologies that can integrate different processes efficiently.

1.3 Motivation for the Proposed Integrated Design

Adams and Barton [6] explored integrating natural gas steam reforming with coal gasification and showed (at the systems level) that integrating the Radiant Syngas Cooler (RSC) in an entrained-bed gasifier and SMR in a single unit as shown in Figure 1 is efficient. The entrained-bed gasifier was used as the preferred gasifier owing to its wide market adoption, ability to handle different feedstocks, and high operating temperatures. The integrated system resulted in an increase in the total system efficiency (compared to non-integrated equivalent processes) by up to 2 percentage points and an increase in net present value of up to \$100 million for many cases. The concept was based on the high temperature coal-derived synthesis gas exiting the gasifier which had to be cooled (conventional cooling involved steam generation) and the endothermic reactions of steam methane reforming that required heat to drive the reactions. The integration strategy also provided flexibility to resolve the issue of the desired synthesis gas molar H_2/CO ratio in polygeneration plants based on the intended application. The proposed configuration also envisioned dynamic operational capability – a key characteristic of a polygeneration plant. Dynamic operational capability is attractive because there are significant potential economic advantages if the products of downstream processes can be changed periodically to respond to market demands and prices [12]. Currently, this is difficult to do in part because the gasifier which forms the upstream part of the plant exhibits poor dynamic operability. However, by integrating SMR and RSC of the gasifier into one unit, it is possible to change syngas production quality and rate dynamically while keeping the gasifier itself at steady state.

Though Adams and Barton [6] showed that this integrated system was both feasible and attractive from a systems-level techno-economic perspective for coal based plants, the device itself was never designed or studied in any level of detail. The authors acknowledged the need to develop and study the integrated RSC-SMR device in order to determine key design parameters, product yields and qualities, conversion efficiencies, controllability, dynamic operating envelopes, and other performance criteria. Therefore, the primary focus is to develop rigorous first-principle based multi-scale, dynamic, heterogeneous model that can aid in addressing the afore-mentioned issues and also analyze the shortcomings of the proposed system in the design space, if any. The model will also be used to study open loop dynamic responses that will aid in the design of a robust control strategy. To the best of our knowledge, this is the first such work to propose a specific design for the integrated RSC/SMR concept, develop a corresponding model, and study its performance.

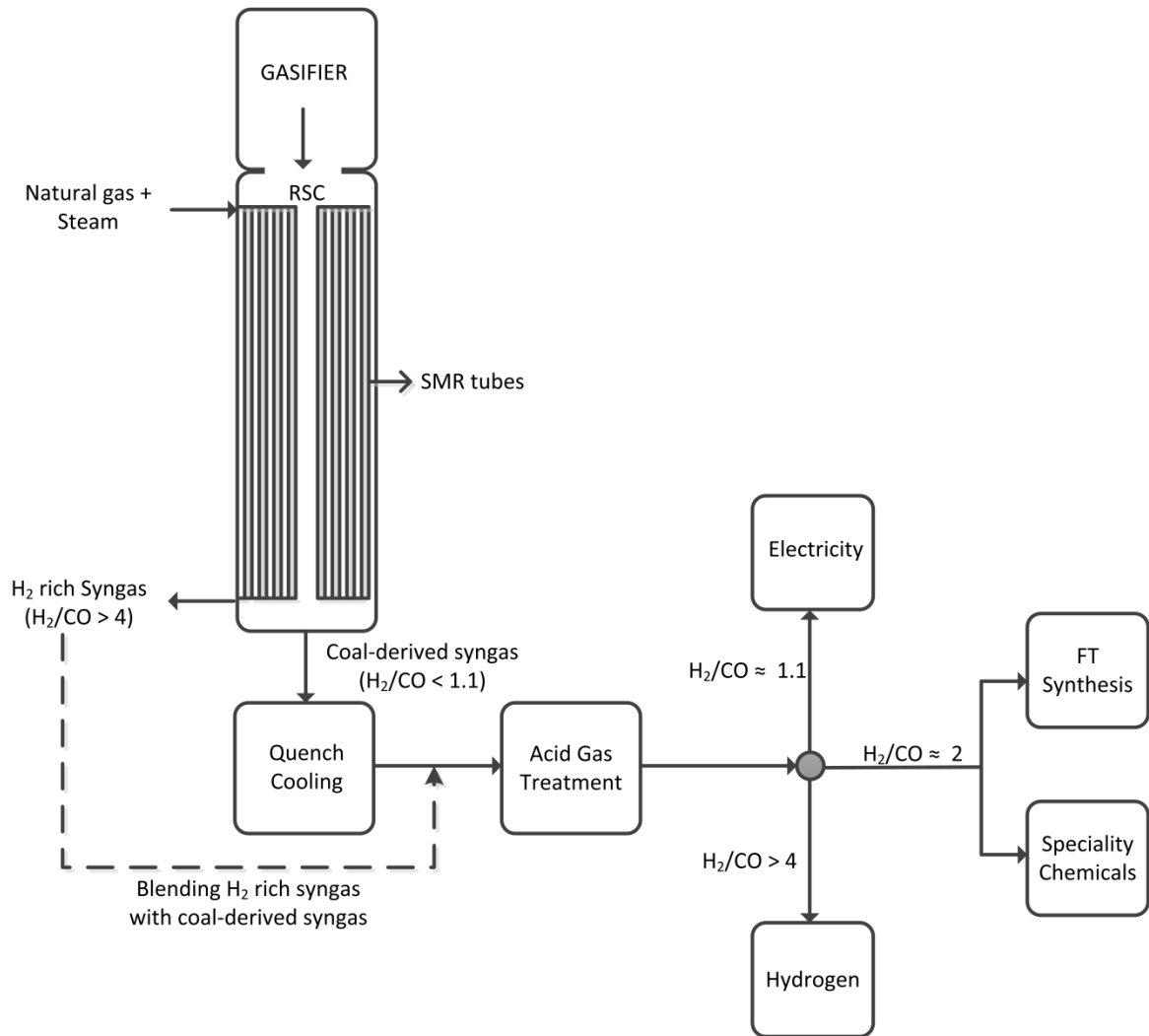


Figure 1: Different potential uses of the proposed integrated system in a polygeneration plant

1.4 Research Objectives

The primary objectives of this thesis are as follows:

- Demonstrate the feasibility of the proposed integrated system for coal-based gasifiers
- Develop a base-case design of the integrated system that can provide the required cooling duty and achieve significant methane conversion
- Analyze dynamic operational capabilities and establish start-up procedures of the integrated system

- Determine optimal designs (if any) to improve upon the base-case performance

1.5 Thesis Structure

This thesis consists of six chapters including the introduction and conclusion. A brief summary for each of the chapters and publications therein is given below:

Chapter 2 presents the development of a multi-scale, dynamic, two-dimensional, heterogeneous model for catalytic steam methane reforming reactors. The model developed from first-principles, accounts for diffusional limitations for both mass and energy within large industrial-scale catalyst particles. The diffusional limitations have been incorporated, not by the conventional method of computing effectiveness factor, but by accounting for the transfer of species as a function of the concentration and temperature gradient existing between the gas phase and catalyst surface along the reactor length. The model has also been validated with available industrial steady-state data from literature. The chapter also presents the results of the dynamic studies done to determine the effects of disturbances in feed on catalyst core and tube wall temperatures. The contents of this chapter have been published in the *International Journal of Hydrogen Energy* after peer review [13].

Chapter 3 presents the novel process intensification design for the proposed integrated system. The feasibility studies are done by first developing a rigorous, dynamic, multi-dimensional model and then using the model to study the performance of the integrated system. The model developed for the radiant syngas cooler has been validated with available data on commercially operating entrained-bed gasifiers. This chapter also establishes specific design heuristics for the integrated radiant syngas cooler and steam methane reformer. Two different flow configurations (co-current and counter-current) are explored, their performance in terms of methane conversion, cooling duty provided and CO₂ emissions avoided are analyzed. Furthermore, a sensitivity analysis has been done to study the impact of model and design parameters on model prediction. The contents of this chapter have been published in the journal *Fuel Processing Technology* [14], and the result and models have been used for control studies that resulted in two other publications in *Chemical Engineering Research and Design* [15], [16] after peer review.

Chapter 4 investigates the transient properties of the proposed integrated gasifier and steam methane reformer. The base-case designs that were established in Chapter 3 are subjected to operating transients to study the flexibility for polygeneration and the feasibility to transition to new operating steady-states. Each system (co-current and

counter-current), under open loop, is subjected to changes in key variables of the SMR feed on the tube side and disturbances to variables of the coal-derived syngas on the RSC side to determine the dynamics and stability of the integrated system. In addition, the key variables that are more likely to violate the design limit in the event of a disturbance are identified thus aiding in the design of an effective control system. A realistic start-up procedure is also established for the integrated system based on current industrial practices that are employed for entrained-bed gasifiers and steam methane reformers. The contents of this chapter have been submitted for peer review in the *AIChE* journal.

Chapter 5 presents a base-case co-current design of the integrated system for a biomass based polygeneration system. The chapter presents a methodology to optimize the base-case designs using both deterministic and stochastic techniques. The co-current design for a biomass gasifier is used as a case study to compare the efficacy of the NLP solver within gPROMS and stochastic techniques like Particle Swarm Optimization and Differential Evolution. The contents of this chapter have been published after peer review in *Computer Aided Chemical Engineering*.

Chapter 6 presents the final conclusions and future directions for this work.

1.6 References

- [1] “World population projected to reach 9.7 billion by 2050,” *United Nations - Department of Economic and Social Affairs*, 2015. [Online]. Available: <http://www.un.org/en/development/desa/news/population/2015-report.html>. [Accessed: 17-Jun-2016].
- [2] “The BP Energy Outlook: Transition to a lower carbon future,” 2016.
- [3] International Energy Agency, “World Energy Outlook 2015 - Executive Summary,” 2015.
- [4] “Scenarios and projections,” *International Energy Agency*. [Online]. Available: <http://www.iea.org/publications/scenariosandprojections/>.
- [5] C. Higman and S. Tam, “Advances in Coal Gasification, Hydrogenation, and Gas Treating for the Production of Chemicals and Fuels,” *Chem. Rev.*, vol. 114, no. 3, pp. 1673–1708, Oct. 2013.

- [6] T. A. Adams II and P. I. Barton, "Combining coal gasification and natural gas reforming for efficient polygeneration," *Fuel Process. Technol.*, vol. 92, no. 3, pp. 639–655, Mar. 2011.
- [7] P. J. Robinson and W. L. Luyben, "Simple Dynamic Gasifier Model That Runs in Aspen Dynamics," *Ind. Eng. Chem. Res.*, vol. 47, no. 20, pp. 7784–7792, Oct. 2008.
- [8] C. Forsberg, "Future hydrogen markets for large-scale hydrogen production systems," *Int. J. Hydrogen Energy*, vol. 32, no. 4, pp. 431–439, Mar. 2007.
- [9] J. K. Rajesh, S. K. Gupta, G. P. Rangaiah, and A. K. Ray, "Multiobjective Optimization of Steam Reformer Performance Using Genetic Algorithm," *Ind. Eng. Chem. Res.*, vol. 39, no. 3, pp. 706–717, 2000.
- [10] D. J. Wilhelm, D. R. Simbeck, A. D. Karp, and R. L. Dickenson, "Syngas production for gas-to-liquids applications: technologies, issues and outlook," *Fuel Process. Technol.*, vol. 71, no. 1–3, pp. 139–148, Jun. 2001.
- [11] T. A. Adams and J. H. Ghouse, "Polygeneration of fuels and chemicals," *Curr. Opin. Chem. Eng.*, vol. 10, pp. 87–93, 2015.
- [12] Y. Chen, T. A. Adams II, and P. I. Barton, "Optimal Design and Operation of Flexible Energy Polygeneration Systems," *Ind. Eng. Chem. Res.*, vol. 50, pp. 4553–4566, 2011.
- [13] J. H. Ghouse and T. A. Adams II, "A multi-scale dynamic two-dimensional heterogeneous model for catalytic steam methane reforming reactors," *Int. J. Hydrogen Energy*, vol. 38, no. 24, pp. 9984–9999, Aug. 2013.
- [14] J. H. Ghouse, D. Seepersad, and T. A. Adams, "Modelling, simulation and design of an integrated radiant syngas cooler and steam methane reformer for use with coal gasification," *Fuel Process. Technol.*, vol. 138, pp. 378–389, 2015.
- [15] D. Seepersad, J. H. Ghouse, and T. A. Adams, "Dynamic simulation and control of an integrated gasifier/reformer system. Part I: Agile case design and control," *Chem. Eng. Res. Des.*, vol. 100, pp. 481–496, 2015.
- [16] D. Seepersad, J. H. Ghouse, and T. A. Adams II, "Dynamic simulation and control of an integrated gasifier/reformer system. Part II: Discrete and model predictive control," *Chem. Eng. Res. Des.*, vol. 100, pp. 497–508, 2015.

CHAPTER 2

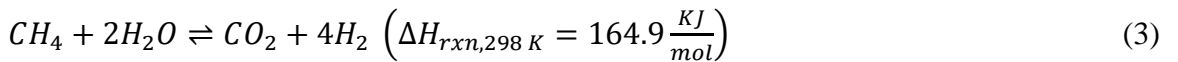
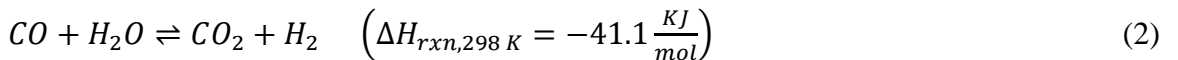
A multi-scale dynamic two-dimensional heterogeneous model for catalytic steam methane reforming reactors

The contents of this chapter have been published in the following peer reviewed journal:

J.H. Ghouse, T.A. Adams II, A multi-scale dynamic two-dimensional model for catalytic steam methane reforming reactors, Int. J. Hydrog. Energy 38 (24) (Aug. 2013) 9984-9999.

2.1 Introduction

Growing energy needs have increased the demand for large scale hydrogen production facilities in petroleum refineries to small-scale on-site generation units for fuel cell systems. Recent interests in polygeneration plants with gasification, power generation and gas-to-liquid units signify the importance of synthesis gas for producing synthetic fuels and electricity [1,2]. Several routes are available for producing hydrogen/synthesis gas; however, steam reforming of hydrocarbons has been the most industrially cost-effective method [3]. Natural gas has been a primary source of hydrocarbon feedstock for steam reforming to produce synthesis gas with a high H₂/CO molar ratio, accounting for more than 75% of operational plants [4–6]. Steam methane reforming (SMR) is carried out in multiple tubes, packed with catalyst, that are placed within a side-fired or a top-fired furnace with operating temperatures ranging from 750°C to 950°C [7,8]. Today SMR process accounts for more than 40% of the hydrogen produced globally [7]. The SMR reaction is catalytic, highly endothermic, and equilibrium-limited which proceeds as follows [9]:



Several models for SMR reactors are available in the literature ranging from 1D steady-state homogenous models to dynamic heterogeneous models. Singh and Saraf [10] developed a 1D steady-state homogenous model where radiant heat transfer from side-fired furnace units was modelled by linking radiation, conduction and convection heat transfer from the furnace gas through the tube walls to the tube gas respectively. Xu and Froment [11] used a 1D steady-state heterogeneous model with intrinsic reaction rate equations that accounted for diffusional limitations to simulate an industrial steam

reformer. Similar modelling work was done by Soliman et al. [12] for both top fired and side fired reformers. Elnashaie et al. [9] and Rajesh et al. [4] have extensively reviewed previous work in this area.

Among the dynamic models, Kvamsdal et al. [13] used a pseudo-homogenous model to simulate trips in steam and feed to the system and predicted the corresponding effect on the outer tube wall temperature. Nandasana et al. [14], citing a need for a model with more details considered, presented a dynamic heterogeneous model by modifying the steady-state 1D model of Rajesh et al. [4] and reported results for three simulated disturbances in inlet feed temperature, feed rate of natural gas and furnace gas temperature. The model was also used to determine optimal operating conditions to negate the effect of aforementioned disturbances. More recently, Pantoleontos et al. [7] presented a model which improved upon the steady-state 1D heterogeneous model of Xu and Froment [11], by including dynamic and axial dispersion terms. The authors also present a detailed review on how apparent reaction rates have been represented by relating intrinsic rates to effectiveness factors, constant or varying, in preceding SMR modelling works.

In all of the previous works cited here, diffusional limitations have been accounted by a unique effectiveness factor specific to a particular catalyst represented by [11]:

$$\eta_i = \frac{\text{apparent rate}}{\text{intrinsic rate}} = \frac{\int_0^V r_i(p_{c,i})\rho_c(\frac{dV}{V})}{r_i(p_{surf,i})\rho_c} \quad (4)$$

where r_i is the rate of reaction for component i , $p_{c,i}$ is the partial pressure of component i inside the solid catalyst, $p_{surf,i}$ is the partial pressure of component i on catalyst surface, V is the volume of catalyst and ρ_c is the density of the catalyst. In the above expression, the intrinsic rate is computed as a function of the catalyst surface/bulk gas phase conditions which would be applicable in the absence of diffusional resistance inside the catalyst pellet, while the apparent rate is computed as a function of actual conditions inside the catalyst particle with diffusional resistance. In other words, the effectiveness factor will be unity if the catalyst pellet has no diffusional resistance. The effectiveness factor does not account for the concentration gradient existing between the bulk phase and catalyst surface. At steady-state conditions, the bulk gas phase concentration may be equal to the concentration at the catalyst surface, but that condition is not valid when a concentration gradient exists during transient modes of operation. The effectiveness factor is even less accurate for the slow composition and temperature transients which occur in large, industrial-scale catalyst particles (large particles are generally utilised to

reduce the pressure drop across the reactor). Furthermore, constant effectiveness factors that are used for homogeneous models need to be determined via experimental studies and vary with the type of catalyst being used. Instead, the model presented in this work is generic such that it requires only the catalyst porosity, tortuosity and pellet density as inputs to account for diffusional limitations in the system. The dynamic model presented in this work incorporates the mass transfer of components to the catalyst surface as a function of the concentration gradient existing between the bulk gas phase and the catalyst surface. Also, the reaction rates are computed at conditions within the catalyst pellet, thereby excluding the need for a unique effectiveness factor.

The other common assumption made in all of the previously published models is the assumption of isothermal conditions inside the catalyst particle which is again applicable only at steady-state operating conditions and for small particles. For example, Nandasana et al. [14] identified a need to compare results obtained from such simplified models with more rigorous models that account for the catalyst temperature as a function of time, radial position and axial position. To our knowledge, attempts have not been made to explore the shortcomings of such assumptions in SMR modelling. Furthermore, Adams and Barton [15], developed a similar model for water gas shift (WGS) reactors and showed that catalyst core temperatures in the WGS reactor could peak briefly by as much as 100°C above steady state conditions during some sharp operating transients. Similarly, a detailed model for SMR reactors can help predict hot or cold spot formation inside catalyst particles which cannot be determined by experimental studies due to difficulty of measuring catalyst core temperatures.

Recent research has focused on increasing the energy efficiency of hydrogen production technology [16]. New and efficient configurations, such as thermo-coupled reactors, are being explored to increase operating efficiencies of existing conventional SMR units [17,18]. To design such new efficient reactor concepts, a detailed SMR model that can capture spatial and temporal variations at the particle level is required. Therefore, the prime focus of this work is to develop a rigorous, dynamic, heterogeneous model for SMR that could be used to study conventional SMR reactors for safe operation and as well as conduct feasibility studies for proposed novel configurations.

2.2 Model Development

The development of the multi-scale, dynamic, heterogeneous SMR model is described in this section. The key variables that vary as a function of time and space in the model are shown in Figure 2. The following primary assumptions have been made:

- (i) Radial variations in concentration and temperature in the gas phase have been neglected as the effect has been found to be negligible for typical industrial conditions [19]. This assumption may not hold well when the tube diameter is increased.
- (ii) Perfect radial mixing in reactor tubes [19]
- (iii) Ideal gas approximation [8, 10, 20]
- (iv) Tubes are assumed to be homogeneous within the reformer; the conditions of any one tube is sufficient to represent all other tubes in the unit [6,8]
- (v) Heavier hydrocarbons than methane have not been considered in this work. This is valid as higher hydrocarbons are typically converted to methane and carbon oxides in a pre-reformer [21].
- (vi) CH_4 , H_2O , CO , H_2 , CO_2 and N_2 are the components considered in this model. Additional components (like heavier hydrocarbons) may be added along with corresponding rate equations but with additional computational burden.
- (vii) Carbon deposition has not been considered in this work. The effect of carbon deposition in steam methane reforming is pronounced only when the steam to carbon ratio is lesser than 1 and for all industrial reformer data sets considered in this work the steam to carbon ratio is greater than 1 [22].

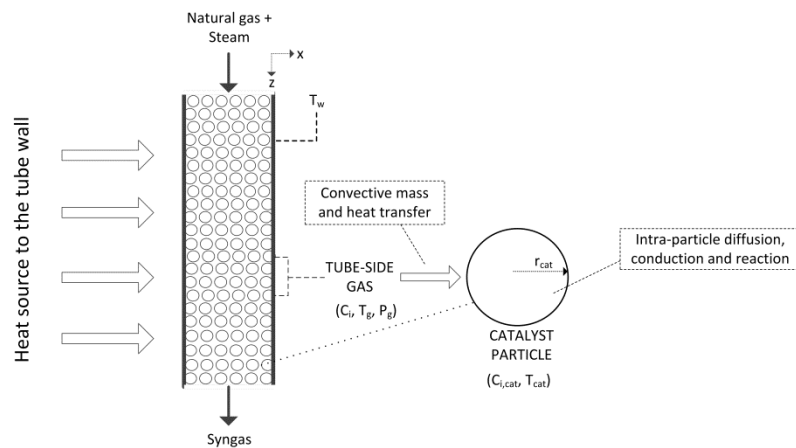


Figure 2: Key temporal and spatial variables considered in the proposed multi-scale SMR model

The proposed model considers three phases: the gas phase inside the tube (but outside the catalyst), the catalyst phase, and the tube wall. In the gas phase, differential mass, energy, and momentum balances are considered as a function of time (t) and axial position (z)

down the length of the reactor. In the catalyst phase, differential mass and energy balances are considered as a function of time, axial position, and radial position inside the catalyst (r). For the catalyst phase, it is assumed that one catalyst particle at axial position z is equivalent to all other catalyst particles at z . In the tube wall phase, the differential mass balances are considered with respect to time, axial position, and radial position x (that is, distance from the inside of the tube wall).

2.2.1 Gas Phase Mass Balance

The dynamic component mass balance in the gas phase is given by:

$$\frac{\partial C_i}{\partial t} = - \frac{\partial(C_i v_i)}{\partial z} - k_i \left(C_i - C_{c_i}|_{r=R_p} \right) \left(\frac{a_v}{\varepsilon} \right), \quad (5)$$

where C_i is the molar concentration of component i in the gas phase, v_i is the interstitial velocity of the gas, k_i is the mass transfer coefficient of component i computed as a function of the concentration difference existing between the gas phase and the catalyst surface $C_{c_i, surf}$, a_v is the ratio of catalyst external surface area per unit volume of the reactor and ε is the bed porosity. The interstitial velocity v_i under the ideal gas assumption, can be computed as [15]:

$$v_i = f(T_g(z, t), P_g(z)) = \left(\frac{F_{total}}{A_{tube} * \varepsilon} \right) \left(\frac{RT_g}{P_g} \right) \quad (6)$$

where F_{total} is the total inlet molar flow rate, A_{tube} is cross sectional area of the tube, R is the universal gas constant, T_g is the temperature and P_g the pressure of the process gas stream. Equation 6 can be substituted in equation 5 or can be treated as a separate equation in the resulting system of partial differential and algebraic equations. The molar flux term in equation 5 (the third term) is proportional to the concentration gradient existing between the bulk gas phase conditions and catalyst surface [23].

2.2.2 Gas Phase Momentum Balance

A pseudo-steady state model has been adopted to account for the pressure drop across the SMR reactor tubes, which is commonly used in similar circumstances [6,13]. This is due

to the numerical stiffness that results if a dynamic momentum balance is considered, even when neglecting gravitational effects, kinetic energy, and deviations in viscosity [15]. Furthermore, since the pressure drop due to friction typically dominates all other terms in a dynamic momentum balance for packed bed reactors [15] the Ergun equation is used to compute the friction factor [24]:

$$\frac{\partial P_g}{\partial Z} = -\frac{G}{\rho_g D_p} \left(\frac{1-\varepsilon}{\varepsilon^3} \right) \left(\frac{150(1-\varepsilon)\mu_g}{D_p} + 1.75G \right), \quad (7)$$

where the mass velocity $G = \rho_g v_s$, ρ_g is the mass density of the gas mixture, v_s is the superficial velocity ($v_s = v_i \varepsilon$), D_p is the particle diameter and μ_g is the viscosity of the gas mixture.

2.2.3 Gas Phase Energy Balance

The dynamic gas phase energy balance is given by:

$$\frac{\partial (T_g C_{p,mix} \rho_{g,molar})}{\partial t} = -\frac{\partial (v_i \rho_{g,molar} C_{p,mix} T_g)}{\partial z} + Q_{conv_{wall \rightarrow gas}} - Q_{conv_{gas \rightarrow cat}} + \sum_{i=1}^{N_c} Q_i \quad (8)$$

where $C_{p,mix}$ is the gas molar specific heat capacity which varies as a function of the local temperature at any axial position z , $\rho_{g,molar}$ is the gas molar density, $Q_{conv_{wall \rightarrow gas}}$ is the heat transferred by convection from the tube wall to the process gas stream, $Q_{conv_{gas \rightarrow cat}}$ is the heat transferred by convection from the process gas stream to the catalyst and Q_i is the net energy transferred by the movement of component i from the bulk gas to catalyst surface or vice-versa (i.e. the energy “carried” by species i in the form of enthalpy). The convective heat transfer is computed as follows:

$$Q_{conv_{wall \rightarrow gas}} = \frac{h_w (\pi D_{tube}) (T_w - T_g)}{A_{tube} \varepsilon} \quad (9)$$

$$Q_{conv_{gas \rightarrow cat}} = \frac{h_g a_v (T_g - T_{c|_{r=R_p}})}{\varepsilon}, \quad (10)$$

where h_w is the convective heat transfer coefficient between tube wall and gas phase, D_{tube} is the tube diameter, T_w is the tube wall temperature, h_g is the convective heat transfer coefficient between the gas phase and catalyst particles and $T_{c,surf}$ is the catalyst surface temperature. The heat flux is a function of the temperature gradient existing between the phases considered [23].

In equation 8, apart from the generally used heat transfer terms in an energy balance, the net energy transferred from or to the gas phase as components move from gas to catalyst or vice-versa, by account of the existing concentration gradient, has been included. This has been computed as follows:

when $C_i > C_{c_i,surf}$ then component moves from gas phase to catalyst phase removing energy from the bulk gas phase,

$$Q_i = - \frac{H_i k_i (C_i - C_{c_i,surf}) a_v}{\varepsilon} \quad (11)$$

where H_i is the enthalpy of component computed at the temperature of gas phase T_g .

when $C_i < C_{c_i,surf}$, then the component will move from catalyst surface to the bulk gas phase adding energy to the system,

$$Q_i = - \frac{H_{c_i,surf} k_i (C_i - C_{c_i,surf}) a_v}{\varepsilon} \quad (12)$$

where $H_{c_i,surf}$ is the enthalpy of component computed at the catalyst surface temperature. Note that the negative sign is still retained but Q_i would be positive as ΔC_i will be negative. Note that this effectively assumes that mass only diffuses in the direction of the gradient.

2.2.4 Gas Phase Boundary Conditions

The boundary conditions for equations 5, 7 and 8 at $z=0$ and $t>0$ are as follows:

$$C_i|_{z=0} = C_{i,inlet} \quad (13)$$

$$P_g|_{z=0} = P_{inlet} \quad (14)$$

$$T_g|_{z=0} = T_{inlet} \quad (15)$$

2.2.5 Gas Phase Correlations

The mass transfer coefficient k_i is computed using the relationship provided by Dwivedi et al. [25] for particle-fluid mass transfer in fixed beds:

$$k_i = \frac{v_s}{\varepsilon} N_{Sc}^{-2/3} \left[\frac{0.765}{N_{Re}^{0.82}} + \frac{0.365}{N_{Re}^{0.386}} \right] \quad (16)$$

Where the Reynolds number $N_{Re} = \frac{D_p \rho_g v_s}{\mu_g}$, Schmidt number $N_{Sc} = \frac{\mu_g}{\rho_g D_{i,m}}$, v_s is the superficial velocity and $D_{i,m}$ is the molecular diffusivity of component i in a mixture.

The convective heat transfer coefficient between the tube wall and bulk gas phase is given by [5,7]:

$$h_w = \frac{\lambda_g}{D_p} \left[2.58 N_{Re}^{1/3} N_{Pr}^{1/3} + 0.094 N_{Re}^{0.8} N_{Pr}^{0.4} \right] \quad (17)$$

where the Prandtl number $N_{Pr} = \frac{C_{p,mix} \mu_g}{\lambda_g}$ and λ_g is the thermal conductivity of the gas mixture. Singh and Saraf [10] mention that the actual heat transfer coefficient to ring-shaped catalysts in conventional reformers is approximately 40% of that calculated using equation 17. Hence, when calculating the convective heat transfer from wall to gas the value is multiplied by 0.4. The convective heat transfer coefficient from the gas phase h_g to the catalyst phase is given by [27]

$$h_g = 1.37 C_{p,mix} G \left(\frac{k_i}{v_s} \right) N_{Sc}^{2/3} N_{Pr}^{-2/3} \quad (18)$$

The porosity of the packed bed and catalyst surface area per unit volume is calculated as follows [15]:

$$\varepsilon = 0.38 + 0.073 \left[1 - \frac{\left(\frac{D_{tube} - 2}{D_p} \right)^2}{\left(\frac{D_{tube}}{D_p} \right)^2} \right] \quad (19)$$

$$a_v = \frac{6(1-\varepsilon)}{D_p} \quad (20)$$

2.2.6 Catalyst Phase Mass Balance

The catalyst particles, generally Raschig rings in the SMR process, are modeled as spherical with an effective diameter D_p [11] for simplicity. The steady-state model describing diffusion and reaction within a catalyst pellet is given by [24]:

$$0 = D_{e,i,mix} \left[\frac{\partial^2 C_{ci}}{\partial r^2} \right] + \frac{2}{r} D_{e,i,mix} \frac{\partial C_{ci}}{\partial r} + r_i \rho_c \quad (21)$$

The above equation has been modified to include the dynamics and rate kinetics at the local concentration and temperature inside the catalyst pellet. The dynamic mass balance for component i within the spherical catalyst particle is as follows:

$$\theta_c \frac{\partial C_{ci}}{\partial t} = \frac{2}{r} D_{e_{i,mix}} \frac{\partial C_{ci}}{\partial r} + \frac{\partial}{\partial r} \left[D_{e_{i,mix}} \frac{\partial C_{ci}}{\partial r} \right] + r_i \rho_c \quad (22)$$

where C_{ci} is the concentration of component i in the catalyst phase, r_i is the rate of reaction or formation of component i , r is the radial position inside the catalyst, $D_{e_{i,mix}}$ is the effective diffusivity of component i in a multi-component mixture, θ_c is the catalyst void fraction and ρ_c is the catalyst density.

2.2.7 Catalyst Phase Energy Balance

The catalyst energy balance used in the current work is analogous to that developed by Adams et al. [15] for a WGS reactor. The model incorporates the temperature dynamics of both the solid and gas phases assuming that the solid catalyst temperature and the gas temperature in the catalyst pores are equal. The energy balance is:

$$\left[(1 - \theta_c) \rho_c C_{p_c} + \theta_c \sum_{i=1}^{N_c} (C_{ci} C_{p_{c,i}}) \right] \frac{\partial T_c}{\partial t} = \lambda_c \left(\frac{1}{r^2} \right) \frac{\partial}{\partial r} \left(r^2 \frac{\partial T_c}{\partial r} \right) + \sum_{i=1}^{N_c} C_{p_{c,i}} \frac{\partial T_c}{\partial r} D_{e_{i,mix}} \frac{\partial C_{ci}}{\partial r} - \rho_c \sum_{i=1}^{N_c} H_{c,i} r_i \quad (23)$$

where T_c is the temperature of the catalyst (represents both solid and gas phase combined assuming that they are at same temperature at radial position r), C_{p_c} is the constant specific heat capacity of catalyst particle, $C_{p_{c,i}}$ is the specific heat capacity of component i in catalyst particle and λ_c is the constant thermal conductivity of the solid catalyst. The heat of reaction is accounted by computing the enthalpy of component i in the catalyst particle as follows:

$$H_{c,i} = \Delta H_{298}^f + \int_{298}^{T_c} C_{p_{c,i}}(T_c) dT \quad (24)$$

2.2.8 Catalyst Phase Boundary Conditions

At any axial position z along the tube length, the following boundary conditions apply for the catalyst centre ($r=0$, $t>0$, z):

$$\left[\frac{\partial C_{c_i}}{\partial r} \right]_{r=0} = 0 \quad (25)$$

$$\left[\frac{\partial T_c}{\partial r} \right]_{r=0} = 0 \quad (26)$$

For the catalyst surface ($r=R_p$, $t>0$, z):

$$\left[D_{e_{i,mix}} \frac{\partial C_{c_i}}{\partial r} \right]_{r=R_p} = k_i \left(C_i - C_{c_i} |_{r=R_p} \right) \quad (27)$$

$$\left[\lambda_c \frac{\partial T_c}{\partial r} + \sum_{i=1}^{N_c} D_{e_{i,mix}} \frac{\partial C_{c_i}}{\partial r} H_{c,i} \right]_{r=R_p} = h_g \left(T_g - T_c |_{r=R_p} \right) - \sum_{i=1}^{N_c} Q_i \left(\frac{\varepsilon}{a_v} \right) \quad (28)$$

Additional equations to compute the binary diffusivity, specific heat capacity, viscosity and thermal conductivity of the components are described in the appendix.

2.2.9 Tube Wall Model

Heat from the reforming furnace is transferred to the process gas through the tube wall. The tubes in SMR units contribute to 10% of the total SMR process installed costs and their service life is very sensitive to temperature changes [28]. It is therefore important to track the tube wall temperature changes. In the current work, two distinct approaches have been investigated: (I) using a steady state polynomial temperature profile for the inner wall hereafter referred to as case 1 and (II) a dynamic 2D model that accounts for conductive heat transfer across the wall hereafter referred to as case 2.

Alatiqi et al. [26] determined that in typical industrial SMR settings at steady-state, the inner tube wall temperature is well-approximated as a second order polynomial and used an empirical quadratic heat flux equation for calculating the heat transferred per unit area of the tube. A similar quadratic profile for the wall temperature was implemented by Pantoleonos et al [7] who limited the heat flux transferred to tubes to less than 80 KW/m². The corresponding quadratic wall profile that was used in their work is given by:

$$T_w(z) = A + Bz + Cz^2 \quad (29)$$

where T_w is the temperature of the wall at any axial position z , $A=1000.4$ K, $B=12.145$ K/m and $C=0.011$ K/m² are parameters that were optimized for maximum hydrogen production. The equation is valid when T_w is less than 1100 K. The authors then used the steady-state wall profile to perform dynamic simulations for an SMR reactor. Though this might be reasonable for small perturbations from steady-state, the approach cannot be applied to simulate larger transients such as cold start-up or shut-down nor can it be used for dynamic changes occurring on the heat-supply side of the SMR (outside the tubes) where the tube wall temperatures can change significantly. Also, Nielsen [3] has remarked that the most critical parameter affecting the tube life is the temperature difference existing across the tube wall. Hence, a detailed model for the tube wall will aid in tracking the temperatures during transient modes of operation.

A detailed dynamic 2D model was used for the tube wall that accounts for heat transfer by conduction within the wall. The model is as follows:

$$\rho_t C_{p_t} \frac{\partial T_w}{\partial t} = \lambda_t \left[\frac{\partial^2 T_w}{\partial x^2} + \frac{\partial^2 T_w}{\partial z^2} \right] \quad (30)$$

where T_w is the temperature of the tube wall at any time t , axial position z , lateral position x and ρ_t , C_{p_t} , λ_t is the density, specific heat capacity and thermal conductivity of the tube material respectively. The thermal conductivity of the tube material has been assumed to be constant in both the axial and lateral directions. For SMR tubes, internal diameter is in the range 0.07- 0.16 m and thickness ranges from 0.01-0.02 m [29]. Because the diameter is much smaller than the tube length, the tube walls are modeled as thin slabs instead of thin cylinders, which is common practice [30].

2.2.10 SMR Kinetics

The model presented can apply any kinetic model appropriate for the type of catalyst used. The SMR rate equations provided by Xu and Froment [32] for nickel-alumina catalysts, developed based on Langmuir-Hinselwood approach, have been widely used to simulate SMR kinetics and is used in the current work. The rate of reactions in equation 1, 2 and 3 are [9]:

$$r_1 = \frac{k_1}{p_{H_2}^{2.5} DEN^2} \left[p_{CH_4} p_{H_2O} - \frac{p_{H_2}^3 p_{CO}}{K_1} \right] \quad (34)$$

$$r_2 = \frac{k_2}{p_{H_2} DEN^2} \left[p_{CO} p_{H_2O} - \frac{p_{H_2} p_{CO_2}}{K_2} \right] \quad (35)$$

$$r_3 = \frac{k_3}{p_{H_2}^{3.5} DEN^2} \left[p_{CH_4} p_{H_2O}^2 - \frac{p_{H_2}^4 p_{CO_2}}{K_3} \right] \quad (36)$$

where p is the partial pressure of the respective component inside the catalyst and DEN is a dimensionless parameter defined as,

$$DEN = 1 + K_{CO} p_{CO} + K_{H_2} p_{H_2} + K_{CH_4} p_{CH_4} + \frac{K_{H_2O} p_{H_2O}}{p_{H_2}} \quad (37)$$

The rate coefficient k_1 , k_2 and k_3 are,

$$k_1 = 9.490 \times 10^{16} \frac{kmol \ kPa^{0.5}}{kg \ hr} \exp\left(-\frac{28879 \ K}{T_c}\right) \quad (38)$$

$$k_2 = 4.390 \times 10^4 \frac{kmol \ kPa^{-1}}{kg \ hr} \exp\left(-\frac{8074.3 \ K}{T_c}\right) \quad (39)$$

$$k_3 = 2.290 \times 10^{16} \frac{kmol \ kPa^{0.5}}{kg \ hr} \exp\left(-\frac{29336 \ K}{T_c}\right) \quad (40)$$

The equilibrium constants K_1 , K_2 and K_3 are,

$$K_1 = 10266.76 \ kPa^2 \exp\left(-\frac{26830 \ K}{T_c} + 30.11\right) \quad (41)$$

$$K_2 = \exp\left(\frac{4400 \ K}{T_c} - 4.063\right) \quad (42)$$

$$K_3 = K_1 K_2 \quad (43)$$

The adsorption constants for the components CH_4 , H_2O , H_2 , and CO are,

$$K_{CH_4} = 6.65 \times 10^{-6} \ kPa^{-1} \exp\left(\frac{4604.28 \ K}{T_c}\right) \quad (44)$$

$$K_{H_2O} = 1.77 \times 10^3 \exp\left(-\frac{10,666.35 \ K}{T_c}\right) \quad (45)$$

$$K_{H_2} = 6.12 \times 10^{-11} \ kPa^{-1} \exp\left(\frac{9971.13 \ K}{T_c}\right) \quad (46)$$

$$K_{CO} = 8.23 \times 10^{-7} \ kPa^{-1} \exp\left(\frac{8497.71 \ K}{T_c}\right) \quad (47)$$

The rates for components are calculated as follows:

$$r_{CH_4} = -(r_1 + r_3) \quad (48)$$

$$r_{H_2O} = -(r_1 + r_2 + 2r_3) \quad (49)$$

$$r_{CO} = r_1 - r_2 \quad (50)$$

$$r_{H_2} = 3r_1 + r_2 + 4r_3 \quad (51)$$

$$r_{CO_2} = r_2 + r_3 \quad (52)$$

The partial pressure of a component is related to the concentration in the catalyst as:

$$p_i = C_{c_i}RT_c \quad (53)$$

2.2.11 Simulation Strategy

The system of PDAE's was implemented and solved in the equation-based general process modelling and simulation software, gPROMS 3.3.1 [33]. The finite difference method was utilized to discretize the spatial domains. 1st order backward finite differences were applied to the axial domain while 2nd order centred finite differences were applied to the radial and lateral domain in case 2. The effect of mesh fineness on accuracy and computational time is discussed in the following sections.

2.3 Model Validation

The model proposed in this work has been validated with different steady-state data sets for industrial SMR reactors reported in literature. The operating conditions and model parameters are presented in Table 1. The equivalent catalyst diameter and catalyst properties are identical in all of the references and hence in this work the value 0.017 m has been used in all of the simulations for the four data sets. The catalyst properties used are tabulated in Table A.5.

Because of the numerical difficulties involved in determining consistent and meaningful initial conditions, the following strategy was employed. First, the initial values of all temperature and concentration variables in the gas and catalyst phases were set to pure N₂ and 750K. In addition, the inlet feed was specified as pure N₂ at 750K at 28.1 bar.

Although these conditions are close to steady-state, they are not quite steady-state. Therefore, the simulation was then run until steady-state was achieved, which we then define as time zero. The value of each variable is then saved and used as the initial conditions for the simulations in sections 2.4.1, and 2.4.2. For the tube wall model in case 2, the initial temperature is set to 750 K.

The model predictions for all of the four data sets are compared with the reported steady-state values for methane conversion and hydrogen mole fraction (dry basis) at the exit. Case 1 of the tube wall model was used. As shown in Figure 3, the model predictions are good with accurate prediction for De Deken et al. to a maximum relative percentage deviation of 5.36% from reported values for Elnashaie et al.-(b) which unlike other data sets was for a top-fired reformer. The results show that even with a pure first-principles approach the model predictions are good and will get better when more accurate data on external wall temperature is available for each of the reformers validated. It should be noted that the data were for reformers operating close to (but not at) thermodynamic equilibrium conditions.

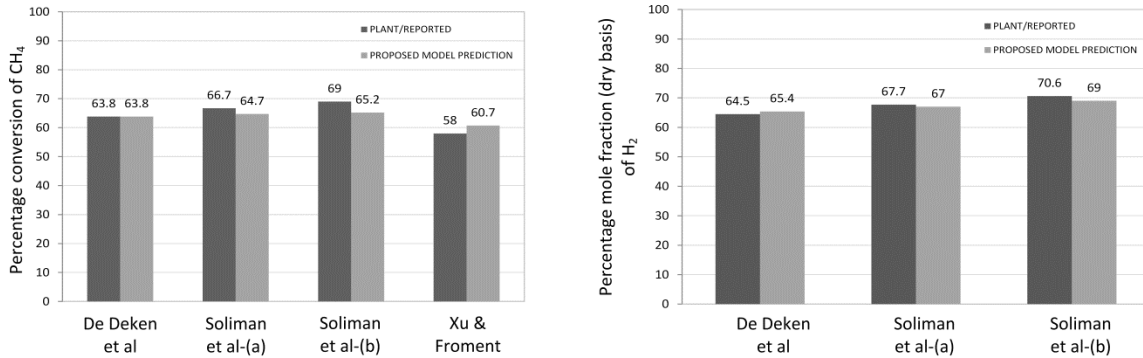


Figure 3: Comparison of percentage conversion of CH₄ and H₂ mole fraction at exit (dry basis) between reported values and the proposed model prediction (case 1)

For each of the above simulations, the number of nodes for the axial domain was 20 while for the radial domain it was 25. Increasing the number of axial grid points had no effect on the predicted methane conversion but increasing the number of radial grid points to 30 resulted in an insignificant percentage change of 0.96% with a substantial increase in the computation time. Therefore the final grid used was with 20 axial nodes and 25 radial nodes.

The model has also been validated using case 2 for the tube wall model with the same reference data sets tabulated in Table 2. Figure 4 shows the steady state methane conversions and hydrogen mole fraction at the exit (dry basis). In these simulations, the grid used included 20 axial nodes, 25 radial nodes and 20 lateral (tube wall) nodes.

Comparing these results to the results obtained using case 1 for the tube wall model, it is seen that model prediction for methane conversion and hydrogen mole fraction (dry basis) at the exit is greater when using Case 2. The increased rate of the endothermic reaction is due to the higher assumed heat transfer to the system by setting the outer wall at the maximum allowable creep limit temperature of 1200 K.

Table 2: Model validation reference for feed conditions and parameters

PARAMETERS	De Deken et al [19]	Soliman et al (a)-[12]	Soliman et al (b)-[12]	Xu and Froment [11]
<i>Feed conditions</i>				
$F_{Total} \left(\frac{Kmol}{hr} \right)$	24.084	21.663	23.271	24.335
$T_o (K)$	793	727.4	723	793.15
$P_o (bar)$	28.1	34.8	36.5	29
<i>Mole fraction</i>				
CH_4	0.2182	0.1763	0.1808	0.2128
H_2O	0.7274	0.7854	0.7981	0.7145
CO	-	-	0.0049	-
H_2	0.0118	0.0137	0.0098	0.0259
CO_2	0.0083	0.0246	0.0061	0.0119
N_2	0.0343	-	0.0003	0.0349
<i>Tube parameters</i>				
$D_t (m)$	0.102	0.0935	0.1	0.1016
$X_t (m)$	0.03	0.044	0.015	0.0306
$L (m)$	12	12	12	12

The validation test was repeated but now with an outer wall temperature of 1150 K. The results presented in Figure 4 show that the proposed model predictions now are more accurate for the first, third and fourth data sets in Table 2 which clearly shows that model

accuracy is case specific. It should hence be noted that improved model predictions can be obtained with accurate data for the outer tube wall temperature or the heat transferred to the tubes from an actual reformer furnace model.

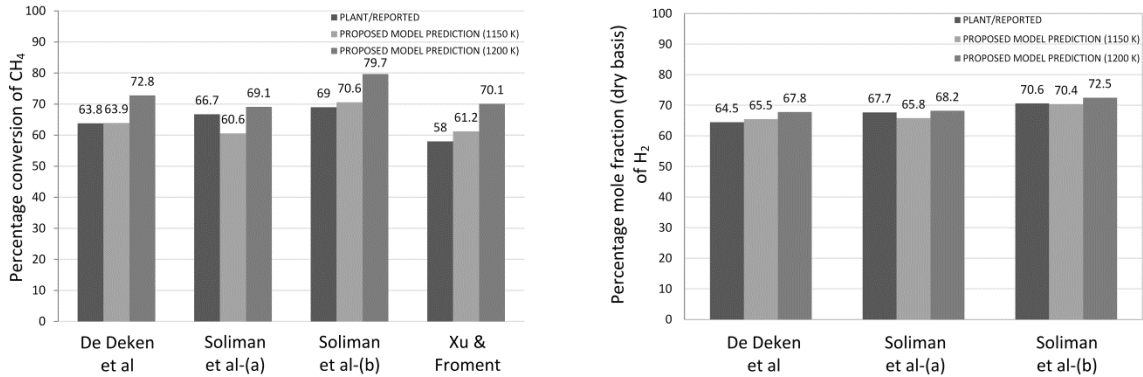


Figure 4: Comparison of percentage conversion of CH₄ and H₂ mole fraction at exit (dry basis) between reported values and model prediction (case 2 with $T_{w,o} = 1200$ K and $T_{w,o} = 1150$ K)

2.4 Results and Discussion

2.4.1 Dynamic Simulation Using Case 1 for Tube Wall Model

For these simulations, a “hot inert” initial state was used where a steady flow of N₂ at 750 K and 28.1 bar is fed under adiabatic conditions (no heat gain or loss through the tube wall). These conditions were selected based on typical feed inlet temperatures in SMR reactors that range from 723 K to 923 K [34].

Then, at time $t=0$, the tubes were introduced to feed conditions corresponding to De Deken et al. data in Table 2 and the quadratic wall profile was set. Figure 5 shows the dynamic mole fraction profile of CH₄ along the reactor tube length and the dynamic mole fraction trajectory of the products CO, H₂, and CO₂ at the exit. The mole fraction trajectory demonstrates the fast dynamics of the SMR reaction reaching a steady state at close to 150 s with significant methane conversion. The mole fraction of CO₂ increases rapidly initially as the water gas shift reaction is promoted at lower temperatures but reduces as the catalyst temperature increases with time which favours the reverse WGS endothermic reaction before steady-state is attained.

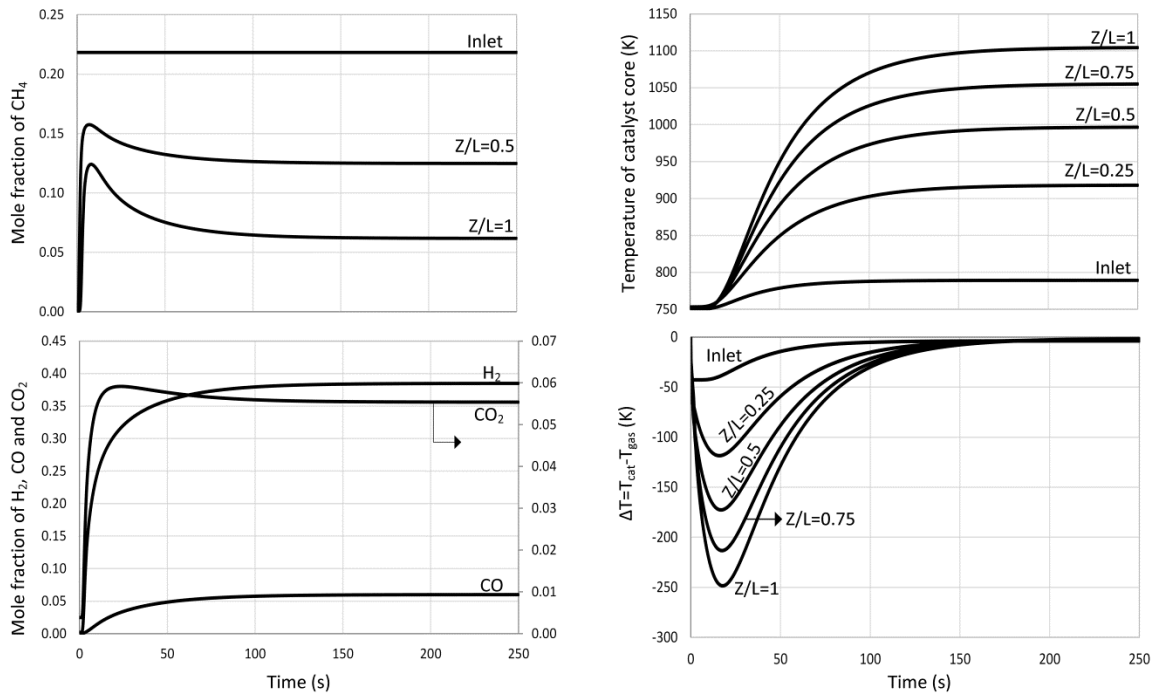


Figure 5: Dynamic profiles for gas phase mole fractions at the exit(left), and core catalyst temperature and temperature difference between catalyst core and gas phase ($\Delta T = T_{cat} - T_{gas}$) at selected points down the length of the reactor (expressed as the axial distance Z divided by the reactor length L) for case 1

Figure 5 also shows the temperature of the catalyst core and the difference between catalyst core and bulk gas phase along the tube length respectively. The catalyst core temperature profiles show no hot or cold spots being formed inside the catalyst, but the temperature difference between the catalyst core and the gas phase can be as large as 250 K at the exit as the gas gets heated rapidly. Even though at steady state the difference is small, a significant temperature difference between the gas and the catalyst phase is seen prior to attaining steady state.

2.4.2 Dynamic Simulation Using Case 2 for Tube Wall Model

The previous simulation was repeated using case 2 for the tube wall model. The results show a significant increase in the time required to reach steady state (more than 200%) compared to case 1 as shown in Figure 6 because the thermal inertia of the wall is now considered.

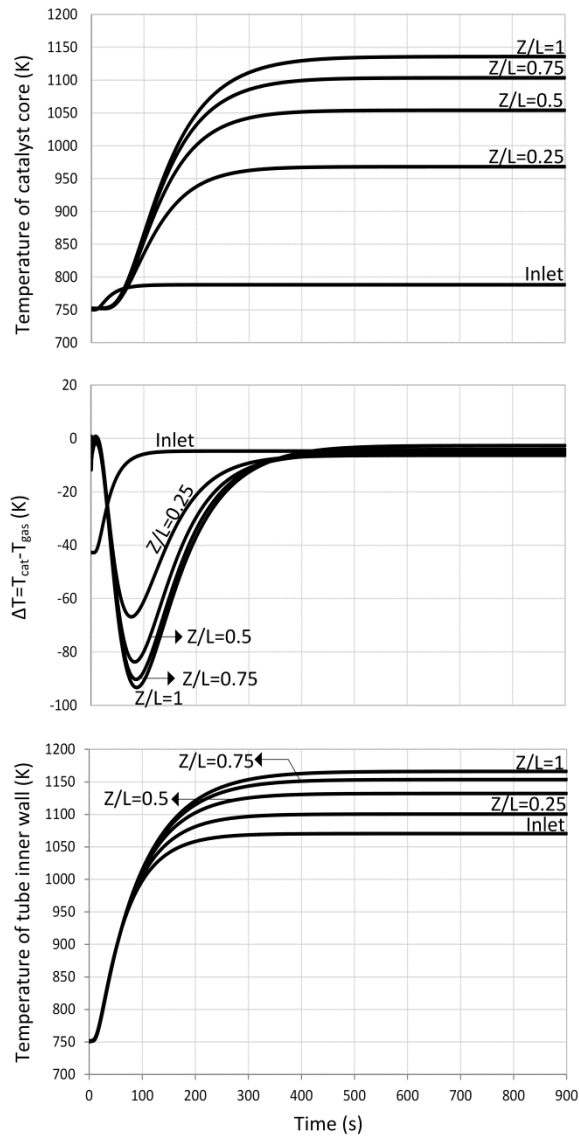


Figure 6: Dynamic profiles for catalyst core temperature, temperature difference between the catalyst core and the gas phase ($\Delta T = T_{\text{cat}} - T_{\text{gas}}$) and temperature of tube inner wall at selected points down the length of the reactor (expressed as the axial distance Z divided by the reactor length L) for case 2

The steady-state temperature for catalyst core at different axial points is greater by an average of 37 K because of the higher inner wall temperature for case 2 than case 1 as shown in Figure 6. Also, the temperature difference between catalyst core and the bulk gas phase show an interesting profile at the initial 6 m of the reactor not seen in the previous simulations (case 1). The catalyst core temperature is greater because the gas is no longer subjected to the instantaneous high heat flux from the tube wall initially as in case 1 at $t > 0$. Also, once the feed is introduced at 793 K, which is greater than the initial

catalyst temperature of 750 K, heat is transferred to the catalyst while heat consumption for the endothermic reaction begins only after the reactants start diffusing into the catalyst. Figure 7 shows significant temperature difference that exists along the axial length between the outer wall (constant in this work =1200 K) and the inner wall at steady-state. Moreover, the inner wall temperature at steady-state can be fit to a polynomial equation of second order $T_{w,i} = (-0.4189 \text{ Km}^{-2}) z^2 + (13.721 \text{ Km}^{-1})z + 1063.8 \text{ K}$ with $R^2=0.9967$. This justifies the quadratic profile used for the inner wall at steady-state by previous researchers [5,6]. However, the results obtained with case 2 show that this only applies to steady-state conditions, thus demonstrating the importance of modeling the dynamic spatial variations in temperature in the wall when simulating start-up conditions or other transient events.

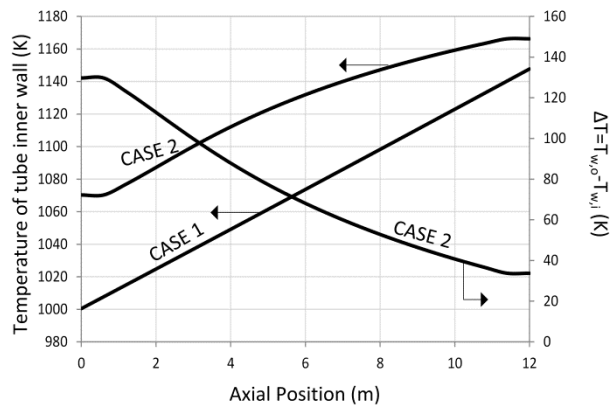


Figure 7: Steady state profiles for the temperature of the tube inner wall and the temperature difference between the outer wall and inner wall of the tube for case 2 ($\Delta T=T_{w,o}-T_{w,i}$)

The spatial and temporal variations at different positions within the catalyst pellet are shown in Figure 8. Both concentration and temperature profiles show that a gradient exists within the solid catalyst until steady state-state is attained at $t=400s$. The temperature difference between the surface and centre of the catalyst can be as high as 75 K in the initial 100s, which is quite significant and not captured in heterogeneous models which assume an isothermal catalyst particle. Furthermore, the concentration profiles show very interesting phenomena in which the concentration of methane inside the catalyst for the first 100s of transition reaches a peak value more than double the steady-state concentration. Furthermore, this peak occurs at different times for different points within the catalyst (i.e., the centre vs. the surface). Because of this, the direction of flow of methane inside the catalyst due to diffusion changes twice during this transition, which

is quite interesting. Thus, the profiles in Figure 8 clearly show the importance of modeling diffusion inside a solid catalyst and signify the need to model temporal and spatial variations in concentration and temperature at the particle level.

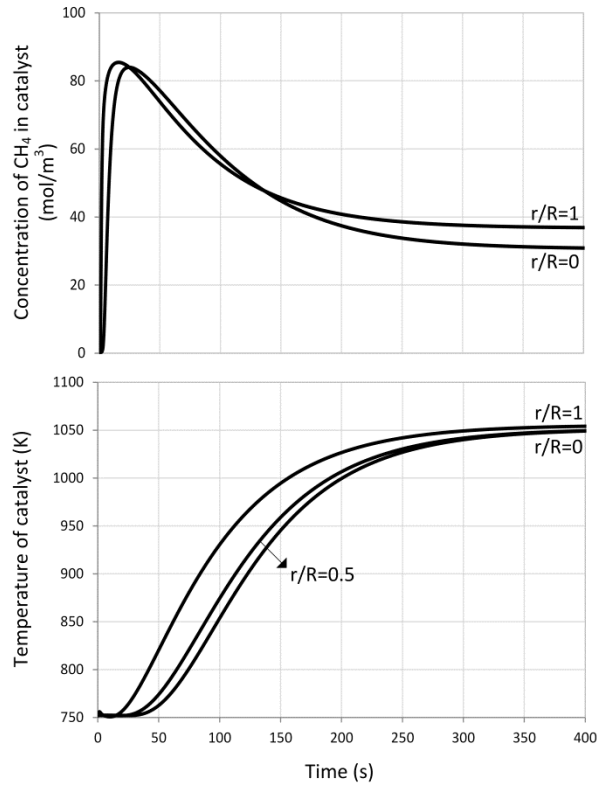


Figure 8: Dynamic profiles for concentration of CH_4 and temperature in the catalyst pellet at an axial distance of 6 m for case 2

2.4.3 Effect of Feed Disturbance

The model was also used to study the effects of disturbances in the inlet process gas stream to the tubes. For these simulations, the initial conditions were the final steady-state profiles obtained from the earlier simulation presented in section 2.4.2. As mentioned previously, the case 1 model cannot predict the effects of the disturbances on the tube wall temperature. Hence, the case 2 model has been used in the following simulations.

- (a) **Feed temperature disturbance:** The effect of a step increase in feed temperature by 100 K was investigated. As the reaction is endothermic, an increase in feed temperature increases the methane conversion from the previous steady-state value as

shown in Figure 9. However, there was only a small effect on the gas phase temperature at the exit at steady-state. Figure 10 shows that the step increase in feed temperature has a very negligible effect on the catalyst core and the tube inner wall temperature beyond 3 m from the inlet. The catalyst core temperature profile compliments the increase in methane conversion by nearly 6 % points from the previous steady-state value in the initial 3 m zone of the tube and by 2.2 % points at the exit. The temperature of the inner tube wall increases from the previous steady-state value by a maximum of 23 K below 3 m length to a minimum of 4 K at the exit as shown in Figure 10.

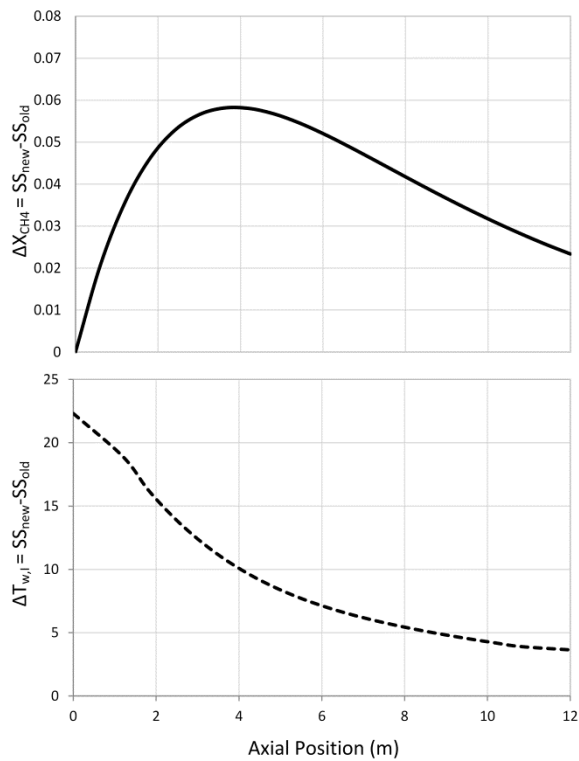


Figure 9: The difference in methane conversion (ΔX_{CH_4}) and inner tube wall temperature ($\Delta T_{w,i}$) between new and previous steady state values for a step increase in feed temperature by 100 K

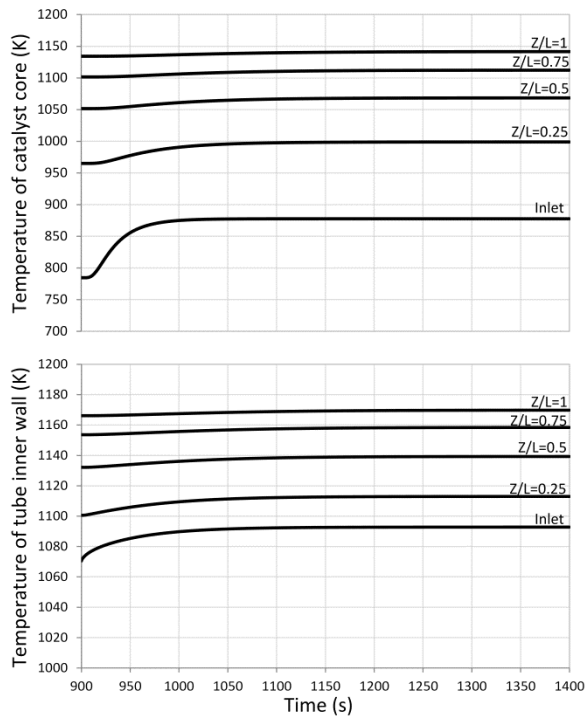


Figure 10: Dynamic profiles for catalyst core and tube inner wall temperature at various axial positions for a step increase in inlet feed temperature by 100 K at $t=900$ s

(b) **Feed molar flow rate disturbance:** The second feed disturbance studied was a 50% step decrease in the inlet feed total molar flow rate (the composition remains the same). Though the feed molar flow rate decreases, the system is still subjected to the same heat flux from the tube wall which increases the core catalyst temperature as shown in Figure 11. The increase in temperature displaces the effect of decrease in concentration and drives the forward endothermic reaction resulting in higher methane conversion from previous steady state as shown in Figure 12. A similar observation of the effect of temperature towards higher methane conversion being dominant over reduced concentration was observed by Nandasana et al. [14]. It can be seen that methane conversion increases at the exit by nearly twelve percentage-points. The step decrease in feed molar flow rate also has an adverse effect on the inner tube wall temperature. Figure 12 shows that the inner tube wall temperature increases by an average of 31 K from the previous steady state values along the axial length.

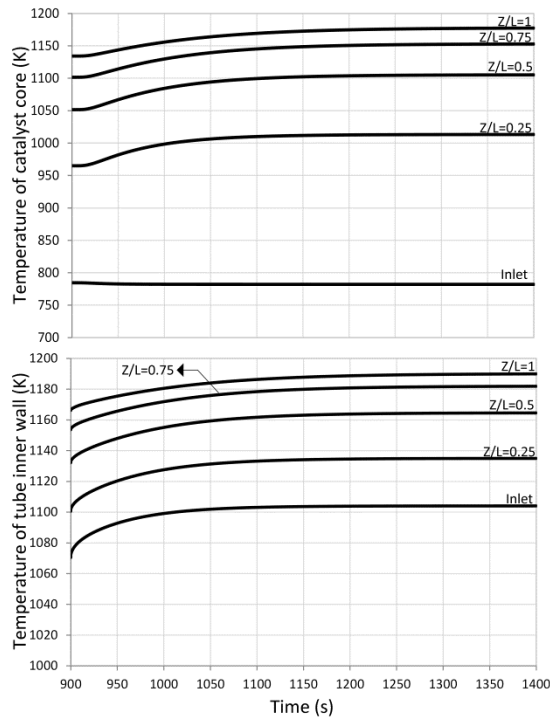


Figure 11: The difference in methane conversion (ΔX_{CH_4}) and inner tube wall temperature ($\Delta T_{w,i}$) between new and previous steady state values for a step decrease in feed molar flow rate by 50%

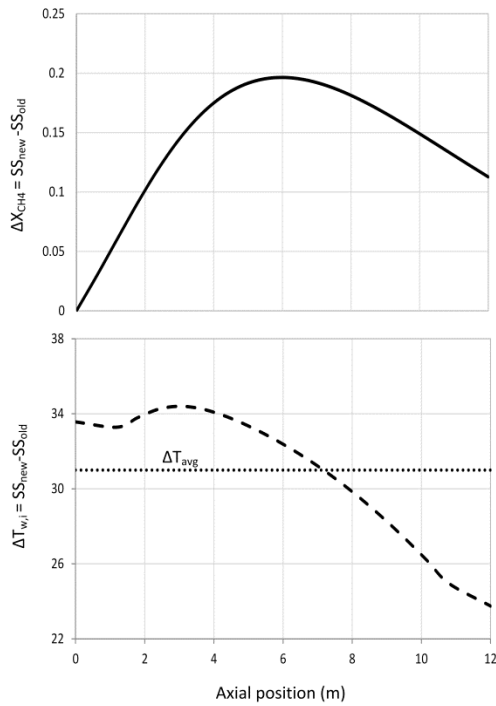


Figure 12: Dynamic profiles for catalyst core and tube inner wall temperature at various axial positions for a step decrease in inlet feed molar flow rate by 50% at $t=900s$

(c) **Inlet steam trip disturbance:** The third disturbance simulated was a trip in the inlet steam flow for 60 s (from 900 s to 960 s) followed by restoring normal supply. The total flow rate inside the tubes decreases and Figure 13 shows the dynamic mole fraction trajectories of CH_4 , CO , and CO_2 at the exit. The mole fraction of CO_2 drops to zero as the WGS reaction ceases without steam and instead reverse WGS is favoured. The CO mole fraction profile shows an interesting trend immediately after the disturbance, where higher conversion of CH_4 is favoured initially due to increasing temperature but later drops as the SMR reaction rate decreases with decreasing steam concentration in the system. However, the mole fraction of CO drops by fifteen percentage-points only as reverse WGS is favoured. The effect of the steam trip also increases the temperature of the catalyst core and the inner tube wall as shown in Figure 13 as the rate of endothermic reaction slows with decreasing reactant (steam) concentration in the system. It can be seen that catalyst core temperature and the inner tube wall temperature can peak by as high as 50 K in the initial 6 m of the reactor tube. After 60s, normal supply is restored and even though previous steady-state points are gradually reached, the temperature transients may cause severe damage to the tube wall.

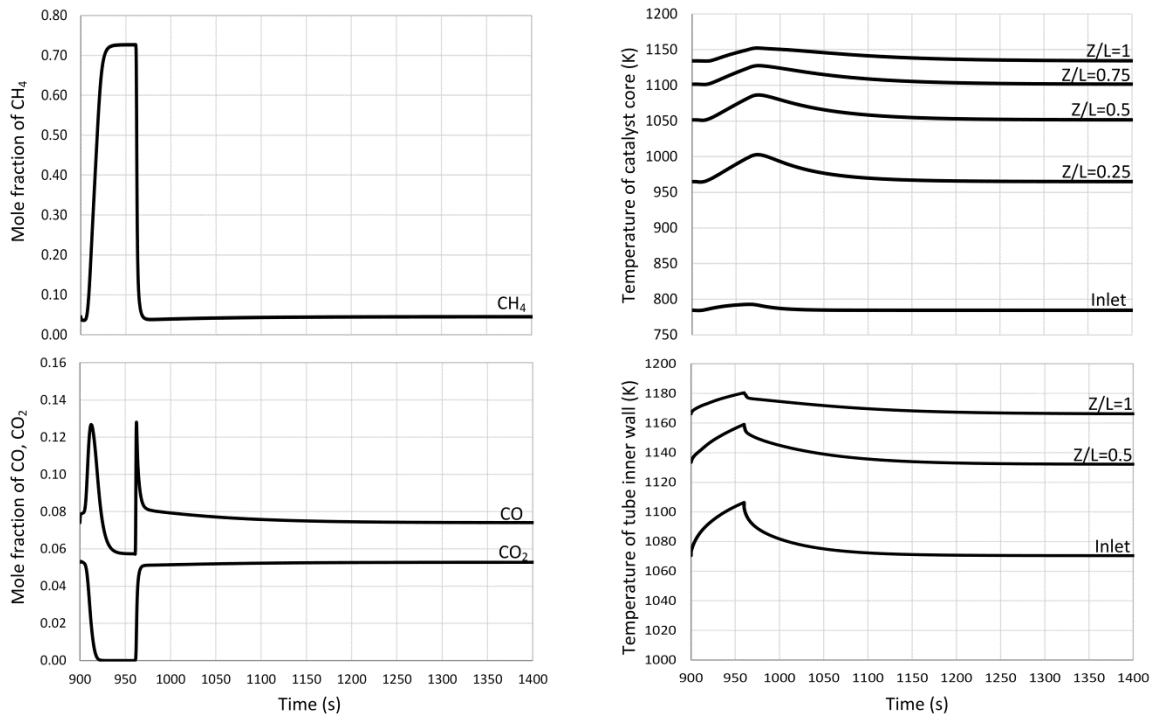


Figure 13: Dynamic profiles for mole fraction (CH_4 , CO , CO_2) at the exit, catalyst core temperature and the inner tube wall temperature for a trip in inlet steam supply for 60s from $t=900\text{s}$ to $t=960\text{s}$

2.5 Conclusions

The multi-scale, dynamic, heterogeneous, two-dimensional model for SMR reactor presented in this work has been developed on a pure first-principles basis and validated with different industrial data sets available from literature. One of the key inferences from this work is that diffusional limitations in gas-solid heterogeneous systems can be accurately accounted without the use of an effectiveness factor for a particular catalyst. This feature eliminates the need for experimentally determined context-specific data but only requires catalyst properties such as porosity, density, tortuosity, diameter and void fraction to predict spatial and temporal variations in concentration and temperature at the particle level. Furthermore, model validation simulations showed great accuracy with no requirement of fitting model parameters to the available industrial data, which is significant considering the model is based purely on first-principles.

The dynamic results presented also demonstrate the importance of a heterogeneous model for the catalyst and tube wall to track spatial variations in temperature during transient modes of SMR operation. For instance, a simulated feed step decrease in molar flow rate showed catalyst core temperature to increase by an average of 44 K and the tube inner wall temperature by an average of 31 K along the reactor tube. The current dynamic model can hence be used to simulate dynamics of a conventional SMR for safe operation to avoid violations in critical operating parameters such as the catalyst core temperature or the tube wall temperature. Though the effects of feed inlet conditions like temperature, steam to methane ratio and flow rate have been studied extensively by Adams and Barton [35] at steady-state, we intend to study the effects of these parameters on operating constraints while transitioning to a new steady-state in our future work. The current model can also be modified to simulate thermo-coupled configurations by substituting appropriate boundary conditions for the wall. Results obtained from such a detailed model can then be used for integrated design and control purposes to handle transient operations.

2.6 Acknowledgements

Financial support from an Imperial Oil University Research Award and NSERC-CRD are gratefully acknowledged. We also thank Philip Tominac for his contributions to the project.

2.7 Nomenclature

Abbreviations

<i>conv</i>	heat transfer by convection
PDAE	Partial Differential Algebraic Equation
SMR	Steam Methane Reforming
WGS	Water Gas Shift
1D	One Dimensional
2D	Two Dimensional

Subscripts

<i>c</i>	catalyst
<i>e</i>	effective
<i>g</i>	gas phase
<i>i, j</i>	component indices

mix mixture

surf catalyst surface

t tube

w tube wall

Variables

a_v ratio of catalyst external surface area per unit volume

C concentration

C_p specific heat capacity

D diffusion coefficient

D_t tube diameter

D_p particle diameter

F_{total} total molar flow rate

G	mass velocity
h	heat transfer coefficient
H	enthalpy
k_1, k_2, k_3	rate coefficients
K_1, K_2, K_3	equilibrium constants
k_i	mass transfer coefficient
L	tube length
M	molecular weight
N_c	number of components
N_{Re}	Reynolds number
N_{Pr}	Prandtl number

N_{Sc}	Schmidt number
P	total pressure
p	partial pressure
R	gas constant
Q	heat transfer
T	temperature
v_i	interstitial velocity
v_s	superficial velocity
r	radial coordinate
r_i	rate of reaction of component i
x	lateral coordinate
y	vapour mole fraction

z axial coordinate

Greek letters

ε bed porosity

λ thermal conductivity

θ_c void fraction of solid catalyst

μ viscosity

ρ_g mass density of gas

$\rho_{g,molar}$ molar density of gas

ρ_c catalyst density

τ tortuosity of catalyst

Ω diffusion collision integral

2.8 References

- [1] J. R. Rostrup-Nielsen, "Syngas in perspective," *Catal. Today*, vol. 71, no. 3–4, pp. 243–247, Jan. 2002.
- [2] J. R. Rostrup-Nielsen, "New aspects of syngas production and use," *Catal. Today*, vol. 63, no. 2–4, pp. 159–164, Dec. 2000.
- [3] T. Rostrup-Nielsen, "Manufacture of hydrogen," *Catal. Today*, vol. 106, no. 1–4, pp. 293–296, Oct. 2005.
- [4] J. K. Rajesh, S. K. Gupta, G. P. Rangaiah, and A. K. Ray, "Multiobjective Optimization of Steam Reformer Performance Using Genetic Algorithm," *Ind. Eng. Chem. Res.*, vol. 39, no. 3, pp. 706–717, 2000.
- [5] P. L. Spath and M. K. Mann, "Life Cycle Assessment of Hydrogen Production via Natural Gas Steam Reforming Life Cycle Assessment of Hydrogen Production via Natural Gas Steam Reforming," Colorado, 2001.
- [6] B. Balasubramanian, A. Lopez Ortiz, S. Kaytakoglu, and D. P. Harrison, "Hydrogen from methane in a single-step process," *Chem. Eng. Sci.*, vol. 54, no. 15–16, pp. 3543–3552, Jul. 1999.
- [7] G. Pantoleontos, E. S. Kikkinides, and M. C. Georgiadis, "A heterogeneous dynamic model for the simulation and optimisation of the steam methane reforming reactor," *Int. J. Hydrogen Energy*, pp. 1–13, Mar. 2012.
- [8] J. R. Fernandez, J. C. Abanades, and R. Murillo, "Modeling of Sorption Enhanced Steam Methane Reforming in an adiabatic fixed bed reactor," *Chem. Eng. Sci.*, vol. 84, pp. 1–11, 2012.
- [9] S. S. E. H. . Elnashaie and S. S. Elshishini, *Modelling, simulation and optimization of industrial fixed bed catalytic reactors*. Gordon and Breach Science Publishers, 1993.
- [10] C. P. P. Singh and D. N. Saraf, "Simulation of Side Fired Steam-Hydrocarbon Reformers," *Ind. Eng. Chem. Process Des. Dev.*, vol. 18, no. 1, pp. 1–7, Jan. 1979.
- [11] J. Xu and G. F. Froment, "Methane steam reforming: II. Diffusional limitations and reactor simulation," *AIChE J.*, vol. 35, no. 1, pp. 97–103, Jan. 1989.
- [12] M. A. Soliman, S. S. E. H. El-Nashaie, A. S. Al-Ubaid, and A. Adris, "Simulation of steam reformers for methane," *Chem. Eng. Sci.*, vol. 43, no. 8, pp. 1801–1806, 1988.
- [13] H. M. Kvamsdal, H. F. Svendsen, O. Olsvik, and T. Hertzberg, "Dynamic simulation and optimization of a catalytic steam reformer," *Chem. Eng. Sci.*, vol. 54, no. 13–14, pp. 2697–2706, Jul. 1999.
- [14] A. D. Nandasana, A. K. Ray, and S. K. Gupta, "Dynamic Model of an Industrial Steam Reformer and Its Use for Multiobjective Optimization," *Ind. Eng. Chem.*

Res., vol. 42, no. 17, pp. 4028–4042, Aug. 2003.

- [15] T. A. Adams II and P. I. Barton, “A dynamic two-dimensional heterogeneous model for water gas shift reactors,” *Int. J. Hydrogen Energy*, vol. 34, no. 21, pp. 8877–8891, Nov. 2009.
- [16] Z. A. Aboosadi, M. R. Rahimpour, and a. Jahanmiri, “A novel integrated thermally coupled configuration for methane-steam reforming and hydrogenation of nitrobenzene to aniline,” *Int. J. Hydrogen Energy*, vol. 36, no. 4, pp. 2960–2968, Feb. 2011.
- [17] G. Kolios, J. Frauhammer, and G. Eigenberger, “Efficient reactor concepts for coupling of endothermic and exothermic reactions,” *Chem. Eng. Sci.*, vol. 57, pp. 1505–1510, 2002.
- [18] V. A. Kirillov, N. A. Kuzin, A. V Kulikov, S. I. Fadeev, A. B. Shigarov, and V. A. Sobyenin, “Thermally Coupled Catalytic Reactor for Steam Reforming of Methane and Liquid Hydrocarbons : Experiment and Mathematical Modeling,” *Theor. Found. Chem. Eng.*, vol. 37, no. 3, pp. 300–308, 2003.
- [19] J. C. De Deken, E. F. Devos, and G. F. Froment, “Steam Reforming of Natural Gas: Intrinsic Kinetics, Diffusional Influences, and Reactor Design,” *Chem. React. Eng. - ACS Symp. Ser. ACS Publ.*, vol. 196, pp. 181–197, 1982.
- [20] K. R. Rout, J. Solsvik, a. K. Nayak, and H. a. Jakobsen, “A numerical study of multicomponent mass diffusion and convection in porous pellets for the sorption-enhanced steam methane reforming and desorption processes,” *Chem. Eng. Sci.*, vol. 66, no. 18, pp. 4111–4126, Sep. 2011.
- [21] I. Dybkjx, “Tubular reforming and autothermal reforming of natural gas - an overview of available processes,” *Fuel Process. Technol.*, vol. 42, pp. 85–107, 1995.
- [22] J. Xu, C. M. Y. Yeung, J. Ni, F. Meunier, N. Acerbi, M. Fowles, and S. C. Tsang, “Methane steam reforming for hydrogen production using low water-ratios without carbon formation over ceria coated Ni catalysts,” *Appl. Catal. A Gen.*, vol. 345, no. 2, pp. 119–127, Aug. 2008.
- [23] K. Hangos and I. Cameron, *Process Modelling and Model Analysis*. San Diego: Academic Press, 2001.
- [24] H. S. Fogler, *Elements Of Chemical Reaction Engineering*, 4th ed. Upper Saddle River. NJ: Prentice Hall, 2006.
- [25] P. N. Dwivedi and S. N. Upadhyay, “Particle-Fluid Mass Transfer in Fixed and Fluidized Beds,” *Ind. Eng. Chem. Process Des. Dev.*, vol. 16, no. 2, pp. 157–165, 1977.
- [26] I. M. Alatiqi, A. M. Meziou, and G. A. Gasmelseed, “Modelling, simulation and sensitivity analysis of steam reformers,” vol. 14, no. 4, pp. 241–256, 1989.
- [27] C. N. Satterfield, *Mass transfer in heterogeneous catalysis*, 1st ed. Cambridge:

Massachusetts Institute of Technology Press, 1970.

- [28] D. A. Latham, K. B. McAuley, B. A. Peppley, and T. M. Raybold, "Mathematical modeling of an industrial steam-methane reformer for on-line deployment," *Fuel Process. Technol.*, vol. 92, no. 8, pp. 1574–1586, Aug. 2011.
- [29] S. Sanaye and E. Baheri, "Thermal modeling of radiation and convection sections of primary reformer of ammonia plant," *Appl. Therm. Eng.*, vol. 27, no. 2–3, pp. 627–636, Feb. 2007.
- [30] F. P. Incropera and D. P. DeWitt, *Fundamentals of Heat and Mass Transfer*, 5th ed. New York, N.Y.: John Wiley & Sons, 2002.
- [31] S. Aslshirin, M. Bahmani, a. Fazlali, and O. Fadavi, "The Static and Dynamic Modeling of a Steam Methane Reforming Hydrogen Plant," *Pet. Sci. Technol.*, vol. 30, no. 18, pp. 1882–1892, Jul. 2012.
- [32] J. Xu and G. F. Froment, "Methane steam reforming, methanation and water-gas shift: I. Intrinsic kinetics," *AIChE J.*, vol. 35, no. 1, pp. 88–96, Jan. 1989.
- [33] *Model Developer Guide*, v3.3.0 ed., no. April. Process systems enterprise, 2010.
- [34] J. R. Rostrup-nielsen and T. Rostrup-nielsen, "Large-scale hydrogen production," vol. 6, no. 4, 2002.
- [35] T. A. Adams II and P. I. Barton, "Combining coal gasification and natural gas reforming for efficient polygeneration," *Fuel Process. Technol.*, vol. 92, no. 3, pp. 639–655, Mar. 2011.
- [36] R. Perry and D. Green, *Perry's chemical engineers' handbook*, 8th ed. New York: McGraw-Hill, 2008.
- [37] R. C. Reid, J. M. Prausnitz, and B. E. Poling, *The properties of gases and liquids*, 4th ed. McGraw-Hill Book Company, NY, 1987.
- [38] E. L. G. Oliveira, C. a. Grande, and A. E. Rodrigues, "Methane steam reforming in large pore catalyst," *Chem. Eng. Sci.*, vol. 65, no. 5, pp. 1539–1550, Mar. 2010.
- [39] M. Defalco, L. Dipaola, and L. Marrelli, "Heat transfer and hydrogen permeability in modelling industrial membrane reactors for methane steam reforming," *Int. J. Hydrogen Energy*, vol. 32, no. 14, pp. 2902–2913, Sep. 2007.
- [40] J. Łabanowski, "Evaluation of reformer tubes degradation after long term operation," *J. Achiev. Mater. Manuf. Eng.*, vol. 43, no. 1, pp. 244–251, 2010.
- [41] "IN-519 cast chromium-nickel-niobium heat-resisting steel," *INCO Databook*, 1976.

CHAPTER 3

Modelling, Simulation and Design of an Integrated Radiant Syngas Cooler and Steam Methane Reformer for Use with Coal Gasification

The contents of this chapter have been published in the following peer reviewed journal:

J.H. Ghouse, D. Seepersad, T.A. Adams II, Modelling, simulation and design of an integrated radiant syngas cooler and steam methane reformer for use with coal gasification, Fuel Process. Technol., vol. 138, pp. 378-389, 2015.

The models described in this chapter and the corresponding gPROMS code has been used in separate control studies that have been published in the following peer reviewed journal:

D. Seepersad, J.H. Ghouse, T.A. Adams II, Dynamic Simulation and Control of an Integrated Gasifier/Reformer System. Part I: Agile Case Design and Control, Chem Eng Res Des., vol. 100, pp. 481-496, 2015.

D. Seepersad, J.H. Ghouse, T.A. Adams II, Dynamic Simulation and Control of an Integrated Gasifier/Reformer System. Part II: Discrete and Model Predictive Control, Chem Eng Res Des., vol. 100, pp. 497-508, 2015.

3.1 Introduction

Synthesis gas (commonly referred to as “syngas”) is a gaseous mixture where the major constituents are hydrogen and carbon monoxide. It is a key feedstock in the production of hydrogen, electricity, methanol, ammonia, synthetic fuels by the Fischer-Tropsch (FT) process, and commodity chemicals such as di-methyl ether (DME). Gasification and reforming are the two primary industrial routes available to produce syngas. The gasification path employs high temperature partial oxidation of solid fossil fuels like coal, biomass or carbon intensive waste products like petcoke and municipal solid waste. For reforming, a variety of hydrocarbons can be used as feedstock, but methane is the preferred feedstock in many of the hydrogen production facilities in the world [1]. Steam reforming of methane is an endothermic catalytic process where the heat required is supplied by combustion of fuel (usually natural gas) to the reactant gases (steam and methane) within multiple tubes that are placed inside a furnace. Though the product from both gasification and reforming is syngas, the quality of syngas varies widely between them. Moreover, each of these processes has unique advantages and disadvantages which are exploited depending upon the industry they are applied in.

One of the main advantages of gasification technology is that it allows for the consumption of vast available resources of solid fossil fuel reserves to produce fuels, chemicals and electricity, thereby reducing the reliance on oil, especially for nations that import crude oil but have large reserves of coal. The major disadvantage in using gasification for fuels and chemicals synthesis is the low H_2/CO molar ratio in the product synthesis gas. The H_2/CO molar ratio usually ranges from 0.75-1.1 depending upon the type of feed (coal/biomass) [2], which generally needs to be upgraded to a higher H_2/CO ratio depending on the application (for example, Fischer-Tropsch (FT) synthesis requires a feed ratio of 2 [2] but some DME synthesis routes require a feed ratio of 1.2-1.5 [3]). The gas is usually upgraded by employing Water Gas Shift (WGS) reactor that converts carbon monoxide and steam to hydrogen and carbon dioxide. This process, however, leads to a loss in the plant-wide carbon efficiency (ratio of total carbon atoms in products to total carbon atoms in the input to the plant), increased carbon dioxide emissions and higher capital and processing costs. Alternatively, reforming is an established technology especially in petroleum refineries, and the resulting syngas is hydrogen rich with a molar H_2/CO ratio of greater than 3. However, the disadvantage is that the Steam Methane Reforming (SMR) process is highly endothermic necessitating combustion of natural gas to supply the heat required resulting in CO_2 emissions. Clearly, there is an opportunity to improve performance of syngas production processes using synergistic options with reduced emissions. Bhat and Sadhukhan [4] present an excellent review on the

possibilities for improving SMR technology using different process intensification strategies, one of which involves using heat integration with exothermic or high temperature systems to supply heat to the endothermic reactions. Considering the need to find more efficient plants that incorporate sustainable designs, the advantages of each of these independent technologies can be harnessed by integrating them together in one unit that will result in efficiency improvements, flexible capability to meet different H₂/CO molar ratios for downstream processes and reduced emissions.

One such application was studied by Adams and Barton [2] who explored integrating natural gas steam reforming with coal based entrained-bed gasifiers as shown in Figure 14. The integrated design resulted in an increase in the total system efficiency (compared to non-integrated equivalent processes) by up to 2 percentage points and an increase in net present value of up to \$100 million for a polygeneration plant of 1711 MW (equivalent to 227 TPH of coal feed). The concept was centred on the need to cool the high temperature coal-derived synthesis gas exiting the gasifier at 1600 K to 1020 K (conventionally done using steam generation in a radiant cooler with tubes) and the steam methane reforming process requiring heat to drive the endothermic reactions. The heat integration strategy involves placing tubes in the radiant cooler filled with SMR catalyst. The proposed integrated configuration resolves the issue of meeting the desired H₂/CO ratio without WGS reactors or external reformers. The proposed configuration also envisioned dynamic operational capability. It is attractive because there are significant potential economic advantages if the products of downstream processes can be changed periodically to respond to market demands and prices [5]. Currently, this is difficult to do in part because the gasifier which forms the upstream part of the plant exhibits poor dynamic operability. However, by integrating gasification and steam methane reforming into one unit, it is possible to change syngas production quality and rate dynamically while keeping the gasifier itself at steady state.

Though Adams and Barton [2] showed that this integrated system was attractive from a systems-level techno-economic perspective, the feasibility of such a device itself was never studied in any level of detail. The authors acknowledged the need to develop and study the integrated device in order to determine key design parameters, product yields and qualities, conversion efficiencies, costs, controllability, dynamic operating envelopes, and other performance criteria. Therefore, the primary focus in this work is to develop first-principle based multi-scale, dynamic, heterogeneous model to address these issues and propose an initial base-case design. To the best of our knowledge, this is the first work to propose a specific design for the integrated concept, develop a corresponding model, and study its performance in detail.

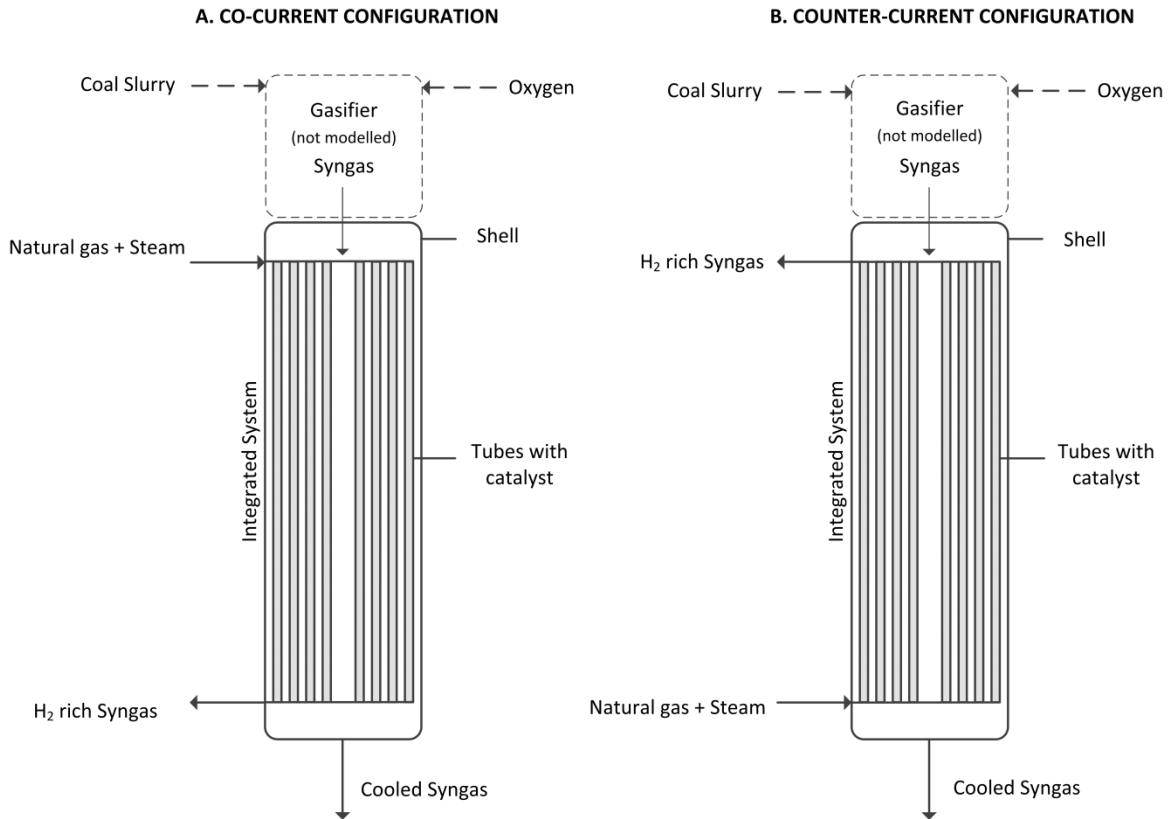


Figure 14: Proposed concept of integrating RSC of an entrained-bed gasifier with SMR

3.2 Materials and Methods

The development of the multi-scale, dynamic, heterogeneous model for the integrated system is explained in this section. The model consists of five sub-models that are coupled to simulate the hybrid system. The five sub-models include the (1) refractory lining of the RSC, (2) coal-derived syngas inside the RSC, (3) tube wall of the SMR tubes, (4) gas phase inside the tubes and (5) catalyst particles that are packed within the tubes. Both co-current and counter-current configurations for the tube gas flow have been analyzed and presented. It should be noted that the gasifier, that precedes the RSC, has not been modelled in this work as the key idea behind the proposed configuration is to operate the gasifier at steady-state and not to subject it to the dynamic transients of a polygeneration plant.

3.2.1 RSC Shell Model Description

The RSC Shell model includes mass balances, energy balances, and a pseudo momentum balance for the shell syngas phase. The model accounts for the spatial and temporal variations in concentration and temperature of the shell gas phase. The following principal assumptions have been made:

- (a) The pressure drop in the radiant cooler is small (on the order of 1 bar [6]) and therefore does not need to be modeled using rigorous first principle equations. Instead, the pressure drop has been fixed and assumed to be linear with respect to vessel length.
- (b) The shell side coal-derived syngas is assumed to contain particles of very small diameter of less than 10 μm (ash and other impurities from gasification) that get entrained with the gas, as suggested by Brooker [5]. The effect of the particles on the total gas emissivity has been considered (see appendix).
- (c) The coal-derived syngas inside the RSC is well mixed and no radial variations in concentration and temperature are considered. As such, each SMR tube is assumed to be identical, a common assumption applied to a similar arrangement of tubes in SMR furnaces [8], [9].
- (d) Molten slag has not been considered in this work. In entrained bed gasifiers, the liquid slag from gasification flows along the gasifier walls and at the RSC inlet, it drops to the bottom as droplets into the quench pool [7][10]. The residence time for the molten slag droplets in the RSC is small enough compared to the gas such that the heat transfer from the slag to the walls is considered negligible.
- (e) Slag deposition on tube surfaces was considered and found to have a relatively small impact on the final design. Since neglecting slag deposition increases the speed of simulation, it was not considered for most of the results in this work.

3.2.2 Shell Gas Phase Mass Balance¹

The dynamic component mass balance in the shell is given by:

$$\frac{\partial c_{i_s}}{\partial t} = -\frac{\partial(C_{i_s}v_s)}{\partial z} + r_i, \quad (1)$$

¹ Contribution of the second author – Dominik Seepersad

where C_{is} is the concentration of species i in the shell gas stream, v_s is the downward velocity of the gas and r_i is the rate of WGS reaction of component i . The boundary condition at $z=0$ is $C_{s,inlet}$.

On the shell side, the coal-derived synthesis gas consists of H_2 , CO , CO_2 , and H_2O and hence exothermic WGS reactions occur and need to be accounted for in the RSC model. Though Monaghan and Ghoniem [11] mention that the WGS reactions in the radiant cooler do not have a major effect on the exit coal-derived syngas composition, there is a need to include WGS kinetics to predict the RSC exit temperature with better accuracy. There are numerous WGS kinetic models available for catalyst based systems that operate below $450^\circ C$ [12] but few are available for homogenous reaction systems such as for gasification chambers. However, the homogenous kinetics for WGS in a combustion environment is used in this work and is given as follows [13], [14]:

$$r_i = 2.75 \times 10^9 \exp\left(-\frac{10100}{T_{g,s}}\right) \left(C_{CO}C_{H_2O} - \frac{1}{K_{eq}}C_{CO_2}C_{H_2}\right) \quad (2)$$

where $T_{g,s}$ is the shell gas temperature, C_{CO} is the concentration of carbon monoxide, C_{H_2O} is the concentration of water vapour, C_{CO_2} is the concentration of carbon dioxide, C_{H_2} is the concentration of hydrogen and K_{eq} is the equilibrium constant. Note that in the above equation, the concentration and pre-exponential factor are in the units of $kmol/m^3$ and $m^3/kmol.s$ respectively that will have to be changed to the required units of $mol/m^3.s$ for the r_i term. The equilibrium constant is given by the following equation [14]:

$$K_{eq} = \exp\left[470.8524 - 175.8711(\ln T_{g,s}) + 21.95011(\ln T_{g,s})^2 - 0.9192934(\ln T_{g,s})^3\right] \quad (3)$$

3.2.3 Shell Gas Phase Energy Balance

The model considers radiative and convective heat transfer between coal-derived synthesis gas on the shell side and tube walls and also between the coal-derived synthesis gas and the refractory lining. It should be noted that the reflection from the refractory lining to the tube wall was considered negligible. However, the effect of this assumption on model prediction is studied in section 3.6.3. The dynamic gas phase energy balance is given by the following equation:

$$\frac{\partial(\rho_{molar,s} H_s)}{\partial t} = -\frac{\partial(v_s \rho_{molar,s} H_s)}{\partial z} - \frac{N_t}{A_s} (Q_{t,rad} + Q_{t,conv}) - \frac{1}{A_s} (Q_{r,rad} + Q_{r,conv}), \quad (4)$$

where H_s is the enthalpy of the gas phase in the shell, N_t is the number of tubes inside the RSC, $\rho_{molar,s}$ is the gas molar density, A_s is the cross-sectional area of the shell, $Q_{t,rad}$ and $Q_{r,rad}$ is the heat transferred by radiation from the gas stream to a single tube wall and the refractory lining respectively, $Q_{t,conv}$ and $Q_{r,conv}$ is the heat transferred by convection from the gas stream to a single tube wall and the refractory lining respectively.

The enthalpy of the gas phase is defined as follows:

$$H_s = \sum_{i=1}^{N_c} H_i y_i, \quad (5)$$

where H_i is the enthalpy and y_i is the mole fraction of component i in the gas phase. The enthalpy of the component i is given by the following equation:

$$H_i = \Delta H_{form,i} + \int_{298}^{T_{g,s}} C_{p,i} dT, \quad (6)$$

where $\Delta H_{form,i}$ is the heat of formation and $C_{p,i}$ is the temperature dependent specific heat capacity of component i in the gas phase.

The heat transfer terms by radiation and convection between the shell gas and tube wall are computed as:

$$Q_{t,rad} = \sigma \epsilon_g \epsilon_t (\pi D_{t,o}) (T_{g,s}^4 - T_w|_{r=R_{t,o}}^4) \quad (7)$$

$$Q_{t,conv} = h_{g,s} (\pi D_{t,o}) (T_{g,s} - T_w|_{r=R_{t,o}}) \quad (8)$$

where σ is the Stefan-Boltzmann constant, ϵ_g and ϵ_t is the emissivity of the gas and tube respectively, $D_{t,o}$ is the outer tube diameter, $T_w|_{r=R_{t,o}}$ is the outer tube wall temperature and $h_{g,s}$ is the convective heat transfer coefficient between the gas phase and the tube wall.

The heat transfer terms between the shell gas and the refractory lining are computed as follows:

$$Q_{r,rad} = \sigma \epsilon_g \epsilon_r (\pi D_{s,i}) (T_{g,s}^4 - T_r|_{r=R_{s,i}}^4) \quad (9)$$

$$Q_{r,conv} = h_r (\pi D_{s,i}) (T_{g,s} - T_r|_{r=R_{s,i}}) \quad (10)$$

where ϵ_r is the emissivity of the refractory, $D_{s,i}$ is the inner RSC shell diameter, $T_{r(r=R_{si})}$ is the inner refractory temperature and h_r is the convective heat transfer coefficient between the gas phase and the refractory lining. The boundary condition at the inlet $z=0$ is $T_{s,inlet}$.

3.2.4 SMR Model

The heterogeneous model used in this work for catalytic steam methane reforming is from our previous work [15]. The SMR model accounts for the spatial and temporal variations in the gas and catalyst particle. For model and auxiliary equations, reaction kinetics and more details the reader is advised to refer to the prior work described in chapter 2.

3.2.5 Tube Wall Model

The model for the SMR tube wall accounts for the transient heat conduction along the axial and radial direction. In our previous work [15], a similar two-dimensional model was presented assuming a planar tube wall. The model has been changed where the thin slab wall approximation has been removed to account for the radial curvature of the wall for improved accuracy and is as follows:

$$\rho_t C_{p_t} \frac{\partial T_w}{\partial t} = \lambda_t \left[\frac{\partial^2 T_w}{\partial r^2} + \frac{\partial^2 T_w}{\partial z^2} \right], \quad (11)$$

where T_w is the tube wall temperature, ρ_t is the density (7880 kg/m^3), C_{p_t} is the specific heat capacity (741 J/Kg-K) and λ_t is specific thermal conductivity (28.5 w/mK) of the tube material[16].

3.2.6 Tube Wall Boundary Conditions

The outer wall of the SMR tube is subjected to radiative and convective heat flux from the shell side gas as described in section 3.2.3. The boundary condition at $r = R_{t,o}$, $\forall z$ and $t > 0$ is given as:

$$\lambda_t \left[\frac{\partial T_w}{\partial r} \right]_{r=R_{t,o}} = \sigma \epsilon_g \epsilon_t (T_{g,s}^4 - T_w|_{r=R_{t,o}}^4) + h_{g,s} (T_{g,s} - T_w|_{r=R_{t,o}}). \quad (12)$$

The tube emissivity ϵ_t is 0.85 [17].

At the inner wall, the heat transfer to the process gas or the tube side gas is by convection. The boundary condition at $r = R_{t,i}$, $\forall z$ and $t > 0$ is given as [15]:

$$\lambda_t \left[\frac{\partial T_w}{\partial r} \right]_{r=R_{t,i}} = h_w (T_w|_{r=R_{t,i}} - T_{g,t}) \quad (13)$$

At the top and bottom of the tube wall, flux is assumed to be zero because of the small cross sectional area [15]. The boundary condition at $z = 0$ and $z = L$, $\forall r$ and $t > 0$ is given as:

$$\left[\frac{\partial T_w}{\partial z} \right]_{z=0} = \left[\frac{\partial T_w}{\partial z} \right]_{z=L} = 0 \quad (14)$$

3.2.7 Refractory Model

The proposed integrated system design does not arrange the tubes into a tightly-packed “waterwall” configuration along the inside of the refractory as is often done in a conventional RSC for a GE gasifier, where high pressure steam is generated. Instead, the SMR tubes are arranged in a circle inside the shell near the edge, but with some spacing between the shell and the tubes, as well as between the tubes themselves (see section 3.4). However, the RSC shell needs to be protected from the high temperature environment and hence the proposed design envisages the use of a refractory lining. Also, refractory lining provides insulation as in conventional coal-fired furnaces and reduces the heat dissipation to the surroundings. In an entrained-bed gasifier, the refractory is typically composed of different layers typically consisting of fireclay brick, insulating brick and a castable layer [6] [11]. However, because detailed refractory layout is outside the scope of this work, only a single layer of firebrick refractory is modelled with “average” properties. The model is similar to the tube wall model and is given as:

$$\rho_r C_{p_r} \frac{\partial T_r}{\partial t} = \lambda_r \left[\frac{\partial^2 T_r}{\partial r^2} + \frac{\partial^2 T_r}{\partial z^2} \right], \quad (15)$$

where T_r is the refractory temperature, ρ_r is the density (2645 Kg/m^3), C_{p_r} is the specific heat capacity (960 J/Kg-K) and λ_r is specific thermal conductivity (1.8 w/m-K) of the refractory material [18]. It should be noted that, if desired, additional layers can be added to the model without great difficulty.

3.2.8 Refractory Boundary Conditions

At $r = R_{RSC,i}$, $\forall z$ and $t > 0$, the inner wall of the refractory is subjected to convective and radiative heat flux from the shell gas.

$$-\lambda_r \left[\frac{\partial T_r}{\partial r} \right]_{r=R_{s,i}} = \sigma \epsilon_g \epsilon_r (T_{g,s}^4 - T_r|_{r=R_{s,i}}^4) + h_{g,r} (T_{g,s} - T_r|_{r=R_{s,i}}), \quad (16)$$

where ϵ_r is the refractory emissivity and $h_{g,r}$ is the convective heat transfer coefficient from the shell gas to the refractory inner wall. The ϵ_r is commonly assigned a constant value of 0.83 [10], but it should be noted that the emissivity changes significantly with temperature. The emissivity values provided in the supplementary material for the refractory were fit to a second order polynomial model as a function of temperature and then used in the simulations given as follows:

$$\epsilon_r = -1 \times 10^{-7} T_r^2 + 8 \times 10^{-5} T_r + 0.8935 \quad (17)$$

At the outer wall of the refractory, heat is exchanged with ambient air via radiation and convection. The boundary condition at $r = R_{RSC,o}$, $\forall z$ and $t > 0$ is given as:

$$-\lambda_r \left[\frac{\partial T_r}{\partial r} \right]_{r=R_{RSC,o}} = \sigma \epsilon_r (T_r^4|_{r=R_{RSC,o}} - T_{amb}^4) + h_r (T_r|_{r=R_{RSC,o}} - T_{amb}) \quad (18)$$

At the top and bottom of the refractory lining, the flux is assumed to be zero because of the small cross sectional area [15]. The boundary condition at $z = 0$ and $z = L$, $\forall r$ and $t > 0$ is given as:

$$\left[\frac{\partial T_r}{\partial z} \right]_{z=0} = \left[\frac{\partial T_r}{\partial z} \right]_{z=L} = 0 \quad (19)$$

3.3 Model Validation for Independent Systems

The model presented in this work is for a proposed integrated configuration and no experimental data exists to validate the model predictions for the integrated device. The key motivation towards the development of a model has been to evaluate the feasibility of the proposed integrated configuration and develop a base case design that can help cut costs when building the pilot-scale system. Though a certain percentage of design margins will be included to account for the model mismatch with the real system, it is essential to show that the model predictions are within a certain confidence interval where the results can be considered reliable to analyze the performance of the integrated system. To this end, the approach that was adopted in this work for model validation was to validate the models for the SMR and RSC independently. Considering the limitations, this is the best methodology possible to validate the integrated model.

The SMR model was validated in the prior work with four industrial data sets available in the open literature. The model showed great accuracy with a maximum deviation of 5.38 % points between the model prediction and data for methane conversion [15]. The RSC shell model validation, in comparison, is more challenging because in the conventional GE gasifiers, the radiant cooler cools the hot coal-derived syngas by generating high pressure steam in a waterwall configuration. Robinson and Luyben [6] simulated the radiant cooler in Aspen using CSTRs in series with a constant coolant temperature of 608 K assuming the RSC consisting 2828 tubes with a diameter of 2 in. They also mention that very few references are available about the design. Kasule et al. [19] followed a similar approach to simulate the RSC, where a PFR was used with a constant coolant temperature of 609 K. Monaghan and Ghoniem [11] also employ a PFR configuration to simulate the radiant cooling, where they note that saturated vapour at the exit of the waterwall is at a temperature and pressure of 608.9 K and 137.8 bar respectively [20]. Furthermore, design and material details for the radiant coolers are sparse and contradictory. For example, references [6], [21], state that the RSC diameter is 16 feet (4.877 m) and length is 100 feet (30.48 m). In another available reference [20], the authors mentioned that the assumed RSC diameter (inner) is 2.74 m with a length of 40 m. Also, details about material properties like the thermal conductivity, density or specific heat capacity are not available. The data sets that were used for model validation, with certain material properties assumed, are tabulated in Table 3.

The method employed in this work to validate the RSC Shell model assumes a ring of tubes along the circumference of the RSC to mimic the waterwall, where steam is

generated within the tubes. The temperature of the tube inner wall is assumed to be at the steam temperature of 609 K instead of the boundary condition described in Eq. 13.

Table 3: Available RSC shell dimensions

Design Parameter (m)	Length	Inner Diameter	Outer Diameter	Tube outer diameter	Tube thickness
Data set 1 [6], [21]	30.48	4.572	4.877	0.0508	0.003
Data set 2 [20]	40	2.74	-	0.07	0.01

The number of tubes in the waterwall that can fit along the circumference of the gasifier is calculated by dividing the circumference of the gasifier by the outer diameter of the tube. For data set 1, using this approach, the number of tubes is 282 while it is 122 for data set 2. The model prediction for exit mole fractions of the gaseous components using data set 1 is shown in Figure 15. It can be seen from the predicted mole fraction of the gaseous components that the rate of WGS reaction is higher when compared to the reported simulated data. This increased rate is because the WGS rate equations were developed for hydrocarbon combustion where the reactions proceed at a much faster rate. This fact is also acknowledged by Monaghan and Ghoniem [11] when using the same reaction kinetics model and instead they used the rate equations by Bustamante et al. [22], [23] for simulating the WGS reactions in the RSC. However, Monaghan and Ghoniem still had to tune the predicted rates to around “0-8%” of that predicted by Bustamante’s expression to match the available data sets. The same strategy could well have been adopted in the current work but were not done for two reasons; (i) the range of 0-8% varies depending on the data set employed and (ii) the rate equations developed by Bustamante et al. [22], [23] were for temperatures in the range of 1070 K-1134 K (for forward WGS reaction) and 1148 K to 1198 K (for reverse WGS reaction), well below the operating temperature of the RSC where the inlet temperature is greater than 1600 K and the exit temperature is in the range 866 K to 1089 K. The model prediction for the RSC exit temperature is 914 K compared to the reported simulated exit temperature of 866 K [6]. However, for the same data set, the design temperature reported for the Tampa power plant, where the RSC is employed, is 1033 K while the operating temperature is below 1005 K [24]. This shows that with the limited available data and with no parameter estimation, the model prediction for RSC exit temperature falls within an acceptable range of around 5% between the two reported temperatures. For data set 2, the model prediction for the exit mole fraction is shown in Figure 15 and compared against the reported model prediction and equilibrium composition reported by Monaghan and Ghoniem [20]. It can be seen that the mole fraction prediction differs marginally from the

reported simulated data but matches with the equilibrium composition reported. However, it was noted that increasing the length changed the molar composition which implies that equilibrium has not been attained. The temperature at the RSC exit is predicted to be 975 K compared to the reported temperature 1089 K [20]. Though the relative percentage error is around 10.5%, it should be accounted that the model has not been modified accurately to represent an actual membrane wall configuration. Also, other effects like slag deposition (considered by the authors) on the wall have been ignored that offer resistance to heat transfer across the walls. This is the principal reason for the predicted drop in temperature compared to the model used by Monaghan and Ghoniem [20] where slag phase temperature was tracked.

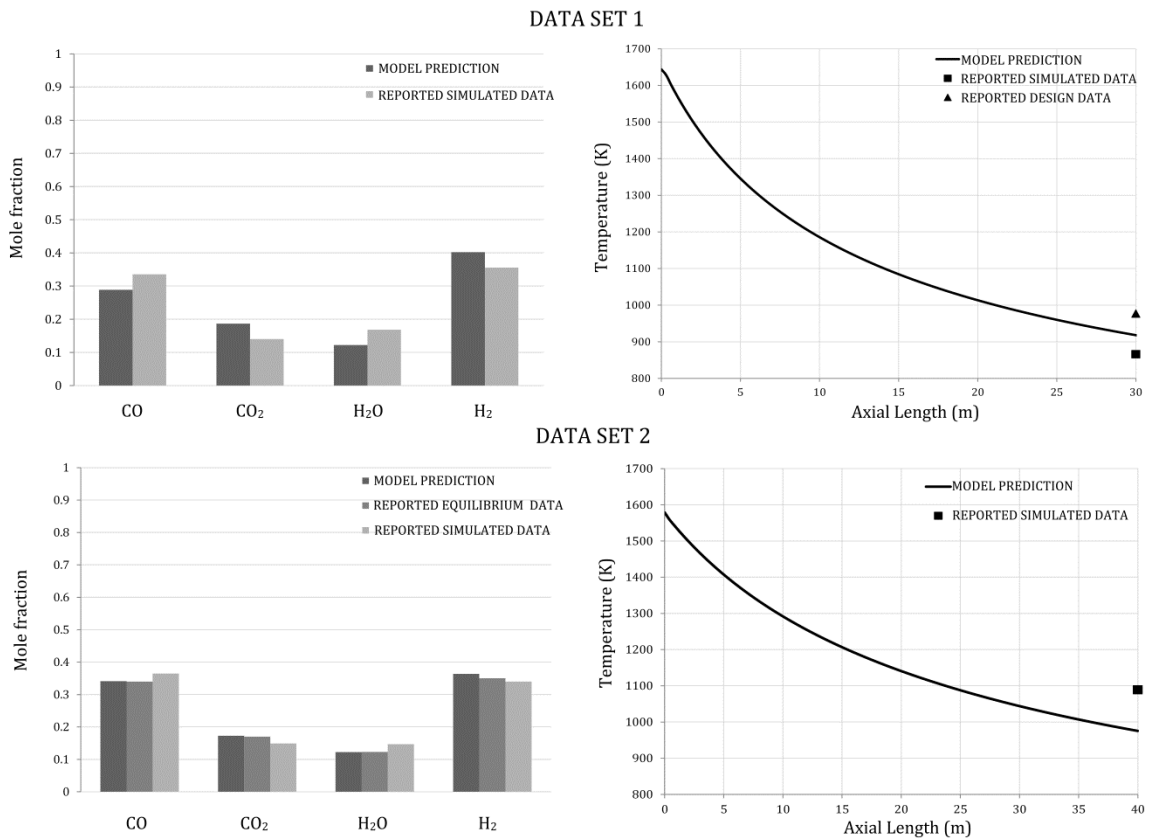


Figure 15: RSC model validation using data sets 1 and 2

Therefore, it is reasonable to conclude, with all the afore-mentioned limitations and considering the fact that the objective is to analyze the design and operability of a new hybrid system for which experimental data is non-existent, the model prediction for the individual systems i.e. the SMR and RSC is sufficient to explore the proposed hybrid configuration.

3.4 Determination of Design Parameters for the Hybrid System

To simulate the integrated system, several design parameters are required as inputs to the model. The key design parameters are the RSC shell diameter, RSC shell length, refractory thickness, tube length, tube diameter and number of tubes within the RSC shell. It is evident that there are several design parameters and a good starting point to determine the values is using a retro-fit approach. Using this technique, the proposed integrated system is first designed for existing entrained-bed gasifiers in the industry. For the tube side design parameters, conventional SMR tube diameters include tubes with outer and inner diameter of 0.1-0.084, 0.102-0.0795, 0.114-0.102, 0.115-0.1 and 0.1322-0.1016 m respectively [25]–[30]. However, the number of tubes inside the RSC is influenced by two contrasting characteristics; (i) the physical space limitation within the RSC shell and (ii) required surface area based on the cooling duty to be provided.

To determine the number of tubes that can fit inside a given RSC shell diameter, the placement of the tubes inside the RSC was treated as a typical fired-heater where the tubes are placed in an annular arrangement in 2 rows along the refractory lined wall. In Figure 16, “C” represents the centre to centre distance between the tubes and “D” represents the outer diameter of the tube. The number of tubes that can be placed depends on the C/D ratio. The C/D ratio can either be 1.5 or 2, but the ratio adopted in this work is 2, as this ensures uniform flux around the circumference of the tubes [31]. The distance between the refractory lined wall and the tube centre is 1.5 times ‘D’. Based on the adopted design properties, the total number of tubes for a single row within the RSC shell is given as:

$$N_t = \frac{\pi(D_{RSC} - 2D_{t,o})}{\left(\frac{C}{D}\right)D_{t,o}} \quad (20)$$

Equation 20 gives the upper limit to the number of tubes that can be fit in a single row as a function of the RSC shell diameter, tube diameter and C/D ratio. However, the question remains if the available surface area is sufficient to provide the required cooling duty for a commercially operating gasifier with a coal-feed rate of 102 tonne per hour that requires 2.54 GJ/tonne coal [2] which equals to 72 MW. Conventional SMR tubes are known to operate with an average heat flux of 45 kW/m² to 90 kW/m² while modern high flux reformers operate at 116 kW/m² [32]. The average flux through the tube walls for the integrated system has been used as a gauge to determine the operation severity [33]. Therefore, the base-case design should be able to provide the minimum cooling duty of 72 MW and the average heat flux should fall between the above-mentioned ranges. Of

the tube diameters considered, a smaller tube diameter with a small wall thickness was chosen (0.1 m-0.084 m) to fit more tubes and also to reduce the weight as the total weight is directly proportional to the diameter [34]. Using equation 20, the number of tubes were 137 assuming two rows of tubes along the refractory wall. However, results are also presented to demonstrate the availability of multiple designs with different tube lengths and diameters.

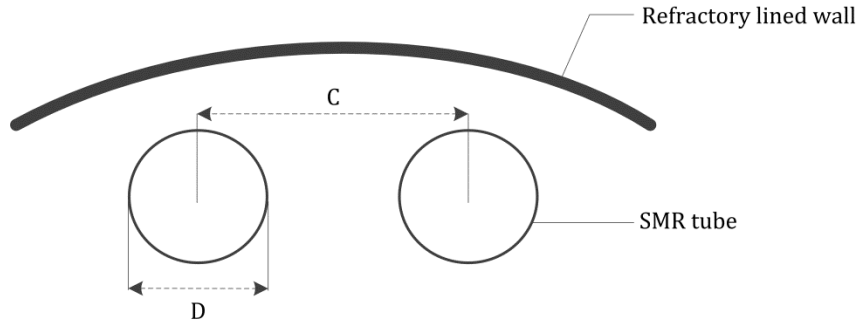


Figure 16: Placement of tubes within the RSC shell

3.5 Numerical Analysis and Grid Independence Test

The model consisting of partial differential and algebraic equations was implemented in gRPOMS v3.7.1, an equation-oriented process modeling environment [35]. The method of finite differences was utilised to discretize the spatial domain that includes the axial direction along the length of the RSC, the radial direction within the catalyst particles and the lateral direction for the tube wall and refractory lining. A centred finite difference scheme was used for both the radial domain of the catalyst particles and for the lateral domain of the tube wall and refractory (2^{nd} order). For the axial domain, backward/forward finite difference scheme was used depending upon the flow configuration.

The grid size determines the accuracy of the model solution but the trade-off of using a fine grid is the computation time associated with a large model as described in this work. Considering the fact that the future applications of the proposed model were to analyze dynamic performance and control design, the effect of grid fineness on computation time was important, and ensuring the accuracy of the model prediction simultaneously. In

numerical methods, accuracy is generally determined by comparing computed value against a true value or the relative percentage change from the previous iteration meets a set tolerance. One way to determine if a grid size is appropriate is to track the percentage change in one of the variables until it meets a specified tolerance. More often than not, one of the key properties that are neglected in the simulation of first-principle models is the global conservation of mass and energy. With huge models, especially those that incorporate several coupled sub-models, a simple but effective way to analyze the accuracy of a particular grid and model validity is to check if the fundamental mass and energy balances are conserved.

In this work, the model was simulated using different grid sizes for the axial and radial domains, keeping the lateral domain for the walls constant at 10 nodes. It was observed that mass within the tubes and the shell was always conserved for different mesh fineness (axial domain) where the relative difference between the inlet and outlet was of the order 10^{-7} . However, the mesh fineness affected the energy conservation significantly because unlike mass which was not flowing between the tube side axial domain and the shell side axial domain, energy was flowing across these domains. Therefore, the conservation of energy between the shell and tube side was evaluated using the following equation:

$$\Delta E = E_{shell} - (E_{tube} + E_{ref}) \quad (21)$$

where E_{shell} is the energy change between the inlet and outlet shell side streams, E_{tube} is the energy change between the inlet and outlet tube side streams and E_{ref} is the energy transferred to the refractory wall from the shell side gas. The cumulative function is then calculated on a normalised basis for both ΔE and CPU time, which is given as follows:

$$CF = \left(\frac{\Delta E}{\Delta E_{max}} \right) + \left(\frac{CPU\ time}{CPU\ time_{max}} \right) \quad (22)$$

As the grid gets finer, the energy balance difference will tend towards zero but at the expense of a huge CPU time. The cumulative function, described in equation 22, combines the effect of conservation and CPU time which is plotted as a function of axial and radial nodes as shown in Figure 17. It is evident that the optimal grid size lies at 75 axial nodes, 35 radial nodes with a cumulative function value of 0.6157. However, it is interesting to note that increasing the radial nodes to 50 has a minimal impact on the cumulative function, while the axial nodes have maximum impact. Therefore, a fine grid with 75 axial nodes and 50 radial nodes was adopted in this work for greater accuracy.

With this grid size, energy balance is closed to around 1% and the CPU time required is 11 minutes.

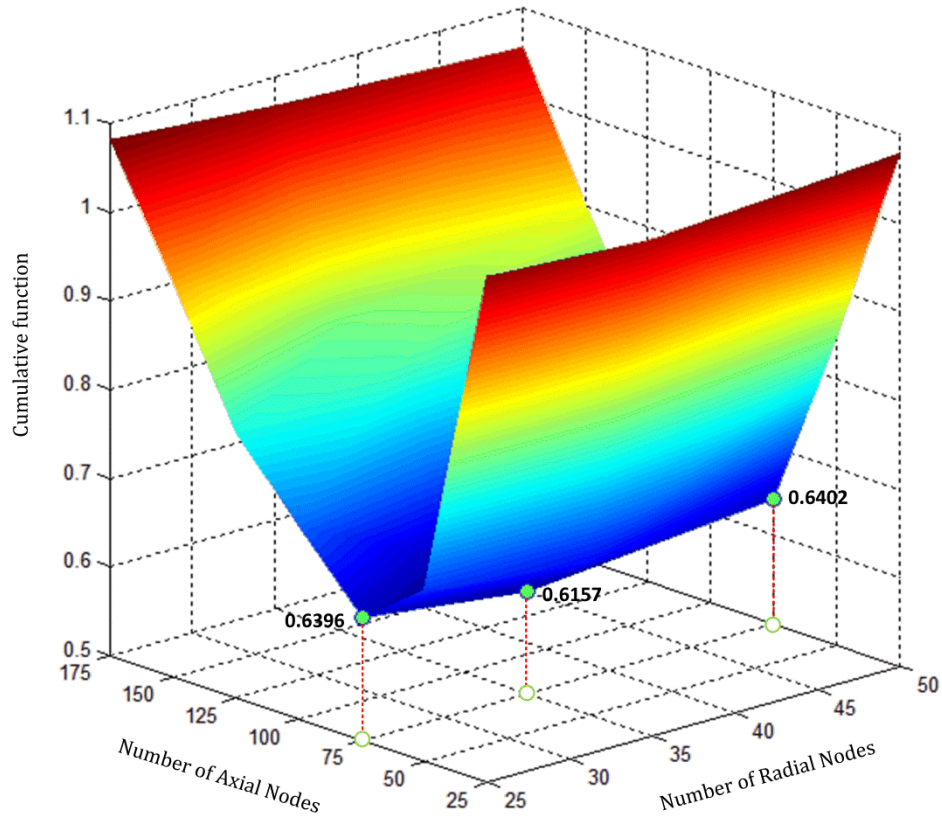


Figure 17: Determination of the optimal numerical grid size

3.6 Results and Discussion

3.6.1 Performance of Co-current and Counter-current Configurations

The dynamic model developed was initialised using a warm start-up case. The warm start-up state was obtained by introducing a nitrogen feed at a temperature of 727.4 K in the tube side and by using an equimolar feed of carbon dioxide and water (products of combustion from gasifier burners used during gasifier start-up) at a temperature of 727.4 K. Once steady-state was attained, feed with conditions given in Table 4 was introduced

on the tube and shell side. The simulation continued until steady-state and the results were then used to analyze the performance.

Table 4: Operating conditions for integrated RSC-SMR system

Parameter	$F_{in,total}$ (kmol/hr)	T_{inlet} (K)	P_{inlet} (bar)	Mole fraction					
				CH ₄	H ₂ O	CO	H ₂	CO ₂	N ₂
Shell Side	12297	1623	55.1	0	0.2376	0.4043	0.2868	0.0714	0
Tube Side	4864	727.4	45	0.2182	0.7274	0	0.0118	0.0083	0.034

Figure 18 shows the steady-state temperature and conversion profiles along the axial length in both co-current and counter-current configurations. The coal-derived syngas on the shell side is cooled to a temperature of 1123 K and 977 K in the co-current and counter-current configuration respectively. This results in a cooling duty provided of 73.5 MW for the co-current configuration and 91 MW for the counter-current configuration. On the tube side, for co-current flow, the process gas exits at a temperature of 1063 K while for the counter-current flow configuration the exit temperature is 1179 K. The coal-derived syngas exit temperature in commercially operating RSC's that employ steam generation to provide the required cooling ranges from 866 K to 1089 K as described in section 3.3. Comparing the RSC shell exit temperatures of the proposed integrated design, the co-current configuration falls slightly outside this range while the counter-current flow falls well within the specified operating range in commercial plants. However, the improvement with the proposed design is the high value product on the tube side. It can be seen from Figure 18 that methane conversion on the tube side is sufficiently high at 80% for co-current configuration and a very high 88% for counter-current configuration. In literature, the reported methane conversion for industrial SMR reactors ranges between 65% to 90%. On the shell side, as the temperature of the coal-derived syngas decreases along the axial length, the exothermic WGS reaction is favoured as shown in Figure 18. In both configurations, CO conversion is around 20%. These results demonstrate two key performance objectives that the proposed design had to meet: (i) provide the required cooling duty and cool the hot coal-derived syngas and, (ii) show that the available exergy is sufficient to integrate a highly endothermic SMR operation with high methane conversion.

With the key performance objectives demonstrated, it is imperative to know if the proposed system is violating any operating constraints. The key operating constraints pertaining to this design include the following: (i) temperature at which refractory failure occurs, (ii) average flux through the SMR tube walls and (iii) maximum tube wall

temperature. The refractory brick failure temperature is set at 2073 K [20] for the inner wall and 573 K for the outer wall.

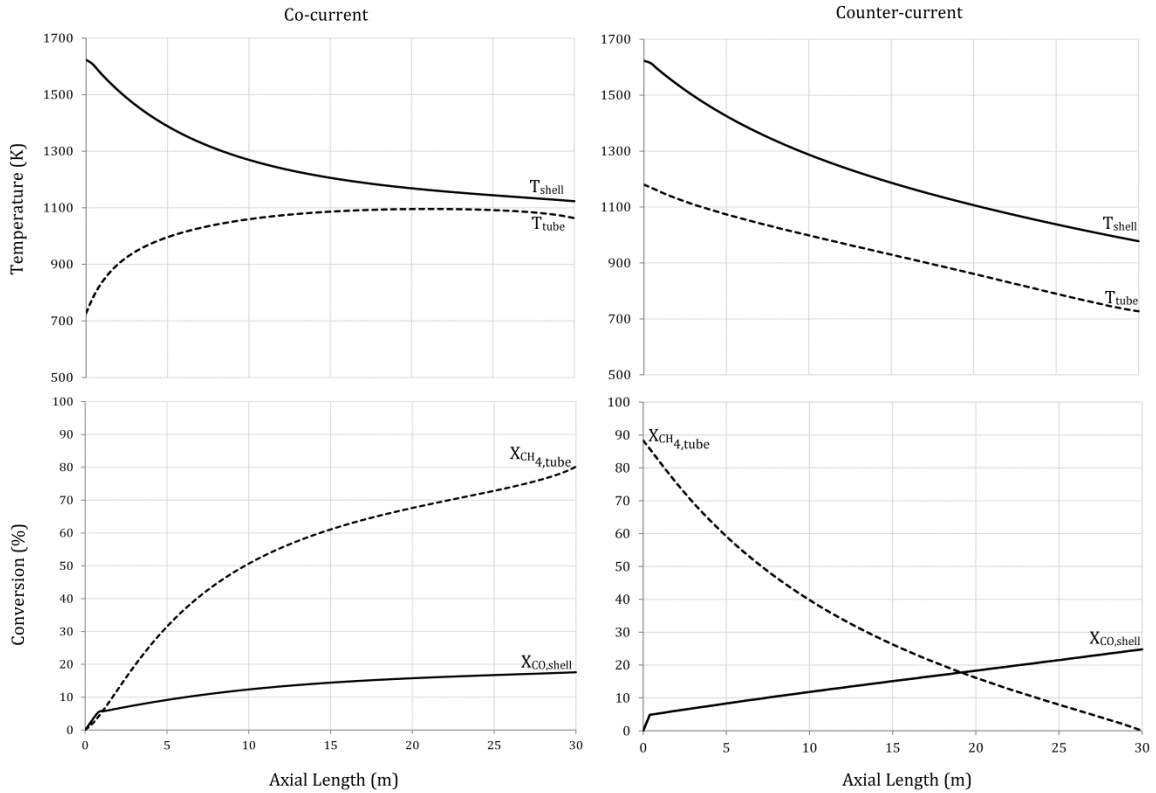


Figure 18: Axial profiles of gas temperature and conversion in co-current and counter-current configuration

Figure 19 shows the axial temperature profiles for the refractory layer (both inner and outer wall) for both co-current and counter-current configuration. It can be observed that the temperature of the outer layer of refractory exceeds the safety limit for the initial 5 m and hence the refractory thickness will need to be increased. It was observed that a 25% increase in refractory thickness from the base case 0.2 m was sufficient to reduce the temperature to acceptable safety limits. Another option to circumvent this problem in the real system is to use either a thicker layer of refractory and/or a different refractory material along the axial length where temperatures exceed the specified limit; in this case for the initial 5 m. Figure 19 also shows the incident flux on the tube walls at every axial node along with the average flux for both the configurations. For co-current flow, the average flux through the tube walls is 45 kW/m^2 and for counter-current flow, the average flux is 56 kW/m^2 . Even though the average flux through the tube walls lies within the range of commercially operating SMR plants, one of the key constraint violations to look for is the maximum tube wall temperature. The tube wall temperatures are a critical

operating parameter that determine tube failures and by extension, the life of the tubes [34]. Available references from literature mention existing tube materials where reformers are designed for a maximum operating tube wall temperature of 1323 K [32], [36]. Also, commercial vendors have different tube materials available for petrochemical steam reformers which have a maximum temperature limit in the range 1273 K to 1448 K [37]. In this work, the maximum design limit temperature is set to 1350 K. Figure 19 shows the axial outer tube wall temperature profiles for both the co-current and counter-current configurations.

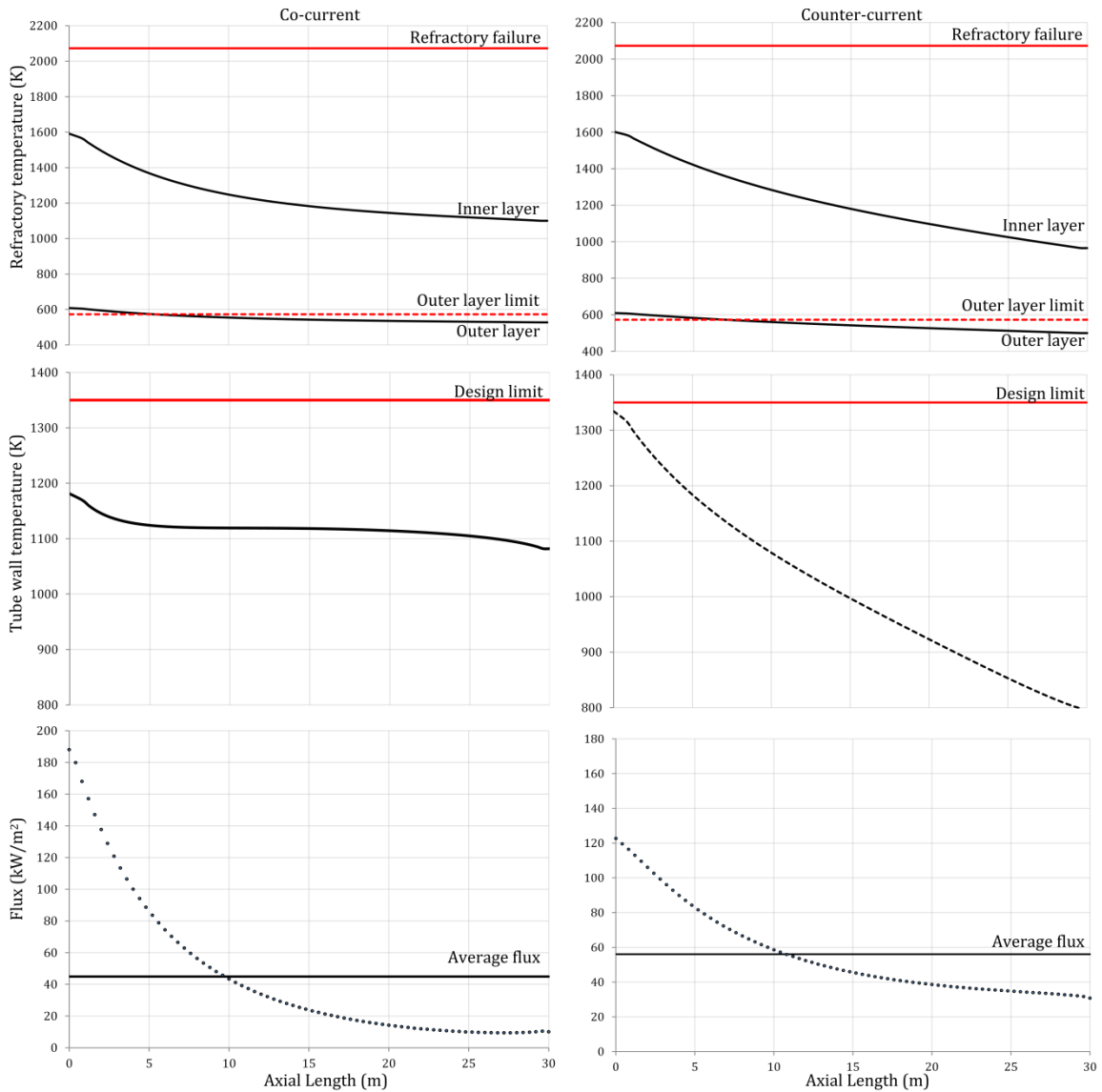


Figure 19: Axial profiles of refractory temperature, outer tube wall temperature and heat flux through tube wall for co-current and counter-current configuration

For the co-current flow configuration, the maximum tube wall temperature is 1181 K and for the counter-current configuration, the maximum tube wall temperature is close to the design limit at 1334 K. It should be noted here that the total flow rate through the tubes for the counter-current configuration was increased by 10% from 1061 kmol/hr (used for the co-current configuration) as the maximum tube wall temperature was 1375 K indicating the opportunity to process higher feed rates.

Another potential problem during nominal operation of the integrated system may be the incidence of a phenomenon termed as “metal dusting” that affects conventional steam reformer tubes. Metal dusting refers to the disintegration of the tube material into dust that includes fine metal particles and oxides. The typical temperature range at which metal dusting occurs in reformers has been established between 723 K and 1073 K. A study by Chun et al [38] on different Nickel based alloys showed that the maximum for localized metal dusting occurred at around 923 K. In our case studies, the tube wall temperatures (both inner and outer) lie outside this range at steady-state. However, the tube wall temperatures may lie in that range during start-up scenarios and while transitioning between different steady-states. It may well be possible that the more recent high performance tube materials (such as alloys resistant to metal dusting) can withstand the afore-mentioned constraints but the promising feature of this study has been to ensure operability with prevailing industry standards.

Both these base-case configurations are able to provide the minimum required cooling duty of 72 MW and high methane conversion. As mentioned previously, the co-current configuration processes 1061 kmol/hr of natural gas feed achieving a methane conversion of 80%. If the same conversion were to be attained using an external reformer assuming the same operating conditions, 264.6 GJ/hr of heat would be required that would be provided by combustion of natural gas. This would result in approximately 13.3 tonnes of CO₂ per hour if we consider 53.1 Kg of CO₂ is emitted per million Btu of energy supplied by natural gas combustion [39]. This shows that the proposed integrated system reduces the carbon emissions when compared to using an external reformer. It should be noted that the numbers do not include the CO₂ avoided if the coal-derived syngas were to be upgraded using WGS reactors which would further increase the total avoided CO₂ when using the integrated system.

3.6.2 Other Design Options

Furthermore, the effect of different tube lengths and tube diameters from the base case designs was analyzed for the co-current configuration considering it was the more feasible design when compared to the counter-current configuration. For all of the cases considered, the feed conditions were set to the same as used for the base case design analysis. Table 5 shows a summary of the performance for each of the different cases considered.

Table 5: Co-current performance with different SMR tube thickness and length

	Base-case Tube diameter (0.1-0.084 m)		Case 1 Tube diameter = 0.132-0.102 m		Case 2 Tube diameter = 0.114- 0.102 m	
	L=30 m	L=20 m	L = 30 m	L = 20 m	L = 30 m	L=20 m
Gasifier Capacity (TPH)	102	102	102	102	102	102
NG Feed Processed (kmol/hr)	1061	1061	1061	1061	1061	1061
Number of tubes	137	137	102	102	120	120
Shell Gas Exit Temperature (K)	1123	1167	1138	1183	1137	1182
Tube Gas Exit Temperature (K)	1063	1095	1094	1127	1112	1146
Methane Conversion (%)	80	68	73.5	62	71	60
Maximum Tube Wall Temperature (K)	1181	1185	1243	1248	1190	1194
Tube side pressure drop (bar)	35	17.3	24	11.6	15.6	7.5
Cooling Duty Provided (MW)	73.5	67	71	65	71	65

It was observed for the base case tube diameter that when the length was reduced to 20 m (approximately 33% reduction), the system was still able to provide a significant cooling

duty of 67 MW to coal-derived syngas but the methane conversion dropped by 15 percentage points to 68%. However, the advantage with using shorter tubes is the significant reduction in pressure drop by around 50%. The low methane conversion can be improved by optimizing the operating parameters like the steam to carbon ratio in the feed, inlet temperature to the tubes or the inlet pressure. This allows space to explore for more agile designs that can improve upon the base case design performance. The analysis also shows the effect of different tube diameters and tube thickness on the performance; case 2 which has the thickest tubes has a significantly high maximum outer tube wall temperature. Additionally, larger outer tube diameters reduce the number of tubes that can be placed inside the shell which in turn increases the inlet feed rate per tube if the same amount of natural gas has to be processed. This in turn affects the inlet velocity and has a pronounced effect on the methane conversion. For example, case 2 with a length of 30 m provides almost the same cooling duty as the base case tube diameter with the same length but the methane conversion drops by 8 percentage points. This demonstrates the various degrees of freedom available such that the performance can be improved significantly using optimization techniques.

3.6.3 Sensitivity Analysis on Performance

It has been demonstrated in section 3.6.2 that several designs are available for the proposed integrated configuration that meets all the key requirements of the process. However, it is important to acknowledge the fact that the designs are based on model predictions and identify how some parameters and assumptions will affect the performance of the proposed integrated configuration. The effect of (i) gas phase emissivity, (ii) radiation from refractory walls and (iii) slag deposition on tubes is considered in this section. For the sake of brevity, the following sections describe the results for co-current configuration while the results for the counter-current configuration can be obtained from the appendix.

The gas phase emissivity used by previous researchers, an important parameter for calculating the radiation heat transfer, range from 0.3 [40] to 0.9, while the maximum gas-particle total emissivity employed in similar modelling works is 0.9 [19], [41]. To assess the effect, the gas phase emissivity was then subjected to a +/- 10% change. Five key parameters that demonstrate performance and operating constraints were chosen to evaluate the effect and percentage change from the base case value. In Figure 20 green bars indicate a favorable change and a red bar indicates a change that is not favorable for that parameter. For example, a decrease in the maximum tube wall temperature will be a

favourable change which improves tube life while a decrease in the exit tube gas temperature is not a favourable change as this will lead to reduced methane conversion. For -10% change in the gas phase emissivity, Figure 20 shows that the effect on the performance is negligible with the methane conversion and cooling duty provided dropping by a mere 0.89% and 0.63 % respectively. The maximum tube wall temperature drops by 1.7% which is favorable. For a +10% change, the opposite trend is observed as the heat transfer increases. The percentage change in methane conversion and cooling duty provided increase by 0.76% and 0.5% respectively while the maximum tube wall temperature increases by 1.5%. Though this change seems to be unfavourable, a 1.5% change translates to a temperature of 1198 K, which is still within the design limit temperature and improves the performance.

Refractory materials are usually coated with a reflective coating that increases the capacity to re-radiate heat back to the furnace chamber minimizing heat loss to the environment. The assumption in this work of no heat transfer between refractory and tube wall might not be bad for evaluating the overall performance because if the heat loss to the environment is minimised it would only result in an increase in conversion of methane. However, the effect of that assumption might be critical for tube wall temperatures and was analysed by treating the shell as an adiabatic chamber. Figure 20 shows the effect on the designated parameters. As expected, methane conversion increases by 3% and 2% in co-current and counter-current configurations respectively. However, it is interesting to note that the cooling duty decreases. This is because in the base case simulations, the shell side gas exchanges heat with the refractory layer which in turn is cooled by the ambient air on the outside. This provides additional cooling to the coal-derived syngas. Also, the effect on the maximum tube wall temperatures was minimal as shown in Figure 20. This shows that the effect of excluding complex radiation modeling has only a minimal effect on the model prediction.

The assumption of no slag deposition may hold true during initial stages of operation but an end of run analysis to determine performance depreciation due to slag buildup is beneficial. A slag layer of thickness 2 mm was considered on the tube surface, typically found in syngas radiant coolers in gasifiers [7]. The model was modified to include an additional two dimensional slag model on the tube surface. Figure 20 shows that the methane conversion and cooling duty provided decrease by 2.8% and 2.5% for co-current configuration. However, the slag buildup protects the tube walls from high temperature and the maximum tube wall temperature drops by 6.5%. This trend is especially significant for counter-current design where the base case maximum tube wall temperature was close to the design limit.

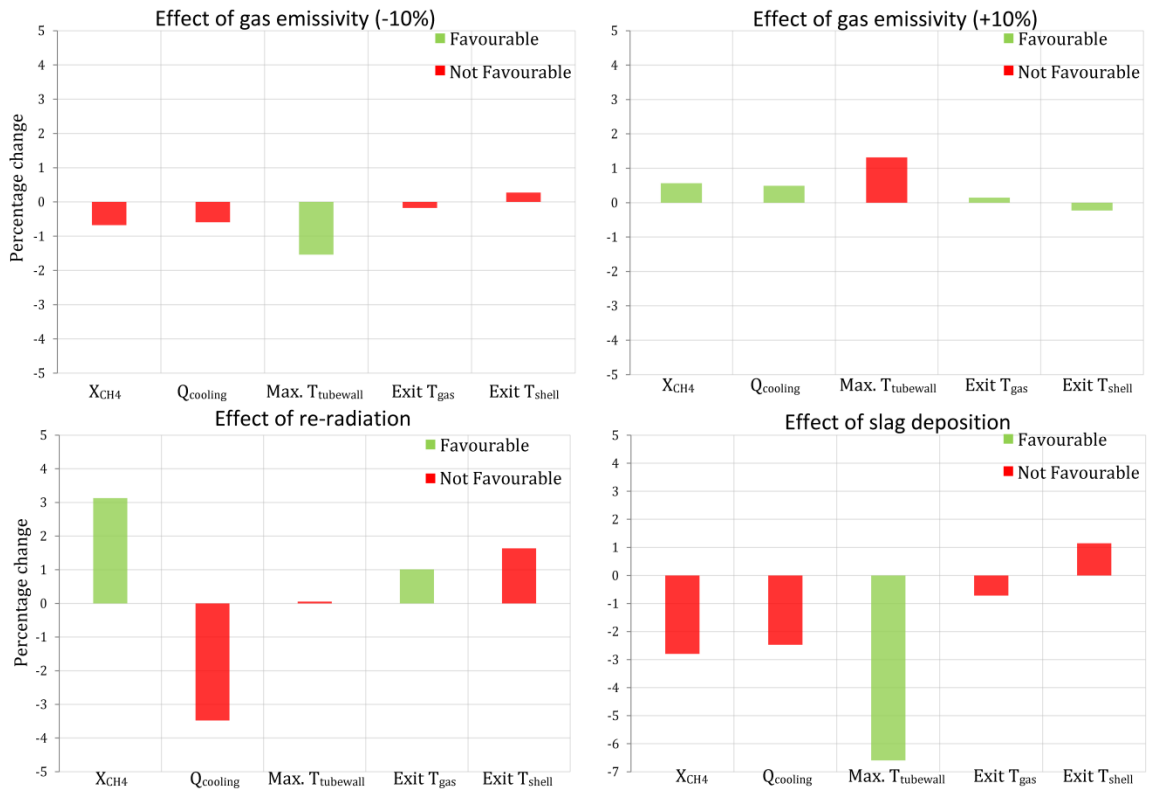


Figure 20: Sensitivity analysis for co-current configuration

3.7 Conclusions

This work presented the design for a process intensification strategy for syngas production using gasification and methane reforming. A dynamic, multi-dimensional model was developed for the integrated system to study feasibility and performance. The results presented showed that the integrated configuration conceived by Adams and Barton [2] is a promising design option requiring further analysis before industrial implementation. The model predictions showed that the integrated design is capable to meet the required performance objectives that were set for a polygeneration plant. The co-current configuration was able to process a total natural gas feed rate of 1061 kmol/hr achieving a methane conversion of 80% without violating any of the set design constraints. In the process, the co-current design provided a cooling duty of 73.5 MW to the hot coal-derived syngas. However, for counter-current configuration, it was observed that the maximum tube wall temperature exceeded the design limit of 1350 K by 25 K for

the same flow rate. A counter-current configuration with increased NG processing capacity of 1165 kmol/hr was demonstrated that met all the design constraints. The simulations showed that both the flow configurations had different advantages and disadvantages. For example, the co-current configuration while providing a lower cooling duty when compared to counter-current design, the maximum tube wall temperature was far lower than that in counter-current flow. On the other hand, the counter-current flow configuration was able to achieve very high methane conversion but with higher tube wall temperatures.

The results from the sensitivity analysis highlighted the aspects to be considered when pilot-scale implementations of the proposed system are done. The results also showed the advantages of shorter tubes with a significant reduction in the pressure drop but with a loss in performance because of a decrease in available heat transfer area. However, the results lay the foundation for exploring smaller and agile design configurations with lower NG capacity for new gasifiers that are not limited by retro-fit constraints. The authors acknowledge that the analysis of a new design based on models, even when rigorous, will be subjected to a certain degree of error due to the several assumptions and parameter uncertainties. However, such modelling efforts lay the groundwork for proof of concept that help support further research exploration into new and innovative reactor designs.

3.8 Acknowledgements

Financial support from an Imperial Oil University Research Award and NSERC-Collaborative Research and Development grant are gratefully acknowledged.

3.9 Nomenclature

Subscripts

c catalyst

conv convection

e effective

g	gas phase
i	component indices
mix	mixture
s	shell
t	tube
r	refractory
rad	radiation
w	tube wall

Variables

a_v	m^2/m^3	catalyst external surface area per unit volume
C	mol/m^3	concentration
C_p	$J/mol/K$	specific heat capacity
D	m	diameter
F_{total}	mol/s	total molar flow rate
G		mass velocity

h $w/m^2/K$ heat transfer coefficient

H J/mol enthalpy

K_{eq} - equilibrium constant

L m tube length

N_c - number of components

p bar partial pressure

P bar total pressure

Q w heat transfer

T K temperature

r m radial coordinate

r_i $mol/m^3/s$ rate of reaction of component i

y - vapour mole fraction

z m axial coordinate

Greek letters

ρ_{molar} mol/m^3 density

σ $w/m^2/K^4$ Stefan-Boltzmann constant

ϵ - emissivity

λ $w/m/K$ thermal conductivity

3.10 References

- [1] J. K. Rajesh, S. K. Gupta, G. P. Rangaiah, and A. K. Ray, "Multiobjective Optimization of Steam Reformer Performance Using Genetic Algorithm," *Ind. Eng. Chem. Res.*, vol. 39, no. 3, pp. 706–717, 2000.
- [2] T. A. Adams II and P. I. Barton, "Combining coal gasification and natural gas reforming for efficient polygeneration," *Fuel Process. Technol.*, vol. 92, no. 3, pp. 639–655, Mar. 2011.
- [3] W. Cho, T. Song, A. Mitsos, J. T. Mckinnon, G. H. Ko, J. E. Tolsma, D. Denholm, and T. Park, "Optimal design and operation of a natural gas tri-reforming reactor for DME synthesis," *Catal. Today*, vol. 139, pp. 261–267, 2009.
- [4] S. A. Bhat and J. Sadhukhan, "Process Intensification Aspects for Steam Methane Reforming : An Overview," *AIChE J.*, vol. 55, no. 2, 2009.
- [5] Y. Chen, T. A. Adams II, and P. I. Barton, "Optimal Design and Operation of Flexible Energy Polygeneration Systems," *Ind. Eng. Chem. Res.*, vol. 50, pp. 4553–4566, 2011.

- [6] P. J. Robinson and W. L. Luyben, "Simple Dynamic Gasifier Model That Runs in Aspen Dynamics," *Ind. Eng. Chem. Res.*, vol. 47, no. 20, pp. 7784–7792, Oct. 2008.
- [7] D. Brooker, "Chemistry of deposit formation in a coal gasification syngas cooler," *Fuel*, vol. 72, no. 5, pp. 665–670, 1993.
- [8] B. Balasubramanian, A. Lopez Ortiz, S. Kaytakoglu, and D. P. Harrison, "Hydrogen from methane in a single-step process," *Chem. Eng. Sci.*, vol. 54, no. 15–16, pp. 3543–3552, Jul. 1999.
- [9] J. R. Fernandez, J. C. Abanades, and R. Murillo, "Modeling of Sorption Enhanced Steam Methane Reforming in an adiabatic fixed bed reactor," *Chem. Eng. Sci.*, vol. 84, pp. 1–11, 2012.
- [10] R. F. D. Monaghan and A. F. Ghoniem, "A dynamic reduced order model for simulating entrained flow gasifiers. Part II: Model validation and sensitivity analysis," *Fuel*, vol. 94, pp. 280–297, Apr. 2012.
- [11] R. F. D. Monaghan and A. F. Ghoniem, "A dynamic reduced order model for simulating entrained flow gasifiers," *Fuel*, vol. 91, no. 1, pp. 61–80, Jan. 2012.
- [12] T. A. Adams II and P. I. Barton, "A dynamic two-dimensional heterogeneous model for water gas shift reactors," *Int. J. Hydrogen Energy*, vol. 34, no. 21, pp. 8877–8891, Nov. 2009.
- [13] W. P. Jones and R. P. Lindstedt, "Global Reaction Schemes for Hydrocarbon Combustion," *Combust. Flame*, vol. 73, no. 3, pp. 233–249, 1988.
- [14] M. Bockelie, D. Swensen, and M. Denison, "A Computational Workbench Environment for Virtual Power Plant Simulation," 2002.
- [15] J. H. Ghouse and T. A. Adams II, "A multi-scale dynamic two-dimensional heterogeneous model for catalytic steam methane reforming reactors," *Int. J. Hydrogen Energy*, vol. 38, no. 24, pp. 9984–9999, Aug. 2013.
- [16] "IN-519 cast chromium-nickel-niobium heat-resisting steel," *INCO Databook*, 1976.
- [17] F. Banisharifdehkordi and M. Baghalha, "Catalyst deactivation in industrial combined steam and dry reforming of natural gas," *Fuel Process. Technol.*, vol. 120, pp. 96–105, Apr. 2014.

- [18] F. P. Incropera and D. P. DeWitt, *Fundamentals of Heat and Mass Transfer*, 5th ed. New York, N.Y.: John Wiley & Sons, 2002.
- [19] J. Kasule, R. Turton, D. Bhattacharyya, and S. E. Zitney, "Mathematical Modeling of a Single-Stage, Downward-Firing, Entrained-Flow Gasifier," *Ind. Eng. Chem. Res.*, p. 120411171146002, Apr. 2012.
- [20] R. F. D. Monaghan and A. F. Ghoniem, "Simulation of a Commercial-Scale Entrained Flow Gasifier Using a Dynamic Reduced Order Model," *Energy & Fuels*, vol. 26, no. 2, pp. 1089–1106, Feb. 2012.
- [21] "The Tampa Electric Integrated Gasification Combined-Cycle Project - An Update," U.S. DOE and Tampa Electric Company, 2000.
- [22] F. Bustamante, R. M. Enick, R. P. Killmeyer, B. H. Howard, K. S. Rothenberger, A. V. Cugini, B. D. Morreale, and M. V. Ciocco, "Uncatalyzed and wall-catalyzed forward water-gas shift reaction kinetics," *AIChE J.*, vol. 51, no. 5, pp. 1440–1454, May 2005.
- [23] F. Bustamante, R. M. Enick, A. V. Cugini, R. P. Killmeyer, B. H. Howard, K. S. Rothenberger, M. V. Ciocco, B. D. Morreale, S. Chattopadhyay, and S. Shi, "High-temperature kinetics of the homogeneous reverse water-gas shift reaction," *AIChE J.*, vol. 50, no. 5, pp. 1028–1041, May 2004.
- [24] "Tampa Electric Polk Power Station Integrated Gasification Combined Cycle Project - Final Technical Report," U.S. DOE and Tampa Electric Company, 2002.
- [25] M. Pedernera, "Use of a heterogeneous two-dimensional model to improve the primary steam reformer performance," *Chem. Eng. J.*, vol. 94, no. 1, pp. 29–40, Jul. 2003.
- [26] A. D. Nandasana, A. K. Ray, and S. K. Gupta, "Dynamic Model of an Industrial Steam Reformer and Its Use for Multiobjective Optimization," *Ind. Eng. Chem. Res.*, vol. 42, no. 17, pp. 4028–4042, Aug. 2003.
- [27] Y. H. Yu and M. H. Sosna, "Modeling for industrial heat exchanger type steam reformer," *Korean J. Chem. Eng.*, vol. 18, no. 1, pp. 127–132, Jan. 2001.
- [28] M. A. Soliman, S. S. E. H. El-Nashaie, A. S. Al-Ubaid, and A. Adris, "Simulation of steam reformers for methane," *Chem. Eng. Sci.*, vol. 43, no. 8, pp. 1801–1806, 1988.
- [29] J. Xu and G. F. Froment, "Methane steam reforming: II. Diffusional limitations and reactor simulation," *AIChE J.*, vol. 35, no. 1, pp. 97–103, Jan. 1989.

- [30] G. Pantoleontos, E. S. Kikkinides, and M. C. Georgiadis, "A heterogeneous dynamic model for the simulation and optimisation of the steam methane reforming reactor," *Int. J. Hydrogen Energy*, pp. 1–13, Mar. 2012.
- [31] K. S. N. Raju, *Fluid Mechanics, Heat Transfer, and Mass Transfer*. Hoboken, NJ, USA: John Wiley & Sons, Inc., 2011.
- [32] T. Rostrup-Nielsen, "Manufacture of hydrogen," *Catal. Today*, vol. 106, no. 1–4, pp. 293–296, Oct. 2005.
- [33] K. Aasberg-Petersen, J.-H. Bak Hansen, T. S. Christensen, I. Dybkjaer, P. S. Christensen, C. Stub Nielsen, S. E. L. Winter Madsen, and J. R. Rostrup-Nielsen, "Technologies for large-scale gas conversion," *Appl. Catal. A Gen.*, vol. 221, no. 1–2, pp. 379–387, Nov. 2001.
- [34] I. Dybkjx, "Tubular reforming and autothermal reforming of natural gas - an overview of available processes," *Fuel Process. Technol.*, vol. 42, pp. 85–107, 1995.
- [35] "gPROMS." Process Systems Enterprise.
- [36] J. R. Rostrup-Nielsen, "Production of synthesis gas," *Catal. Today*, vol. 18, no. 4, pp. 305–324, Dec. 1993.
- [37] "Construction material | S+C Spun Casting - Petrochemical Industry." [Online]. Available: <http://www.schmidt-clemens.com/industries/petrochemical-industry/alloysmaterials.html>. [Accessed: 20-Jun-2014].
- [38] C. M. Chun, F. Hershkowitz, and T. a. Ramanarayanan, "Materials challenges in syngas production from hydrocarbons," *ECS Trans.*, vol. 19, no. 10, pp. 9–20, 2009.
- [39] "Carbon Dioxide Emissions Coefficients." [Online]. Available: http://www.eia.gov/environment/emissions/co2_vol_mass.cfm.
- [40] H. Watanabe and M. Otaka, "Numerical simulation of coal gasification in entrained flow coal gasifier," *Fuel*, vol. 85, pp. 1935–1943, 2006.
- [41] R. Govind and J. Shah, "Modeling and simulation of an entrained flow coal gasifier," *AIChE J.*, vol. 30, no. 1, pp. 79–92, Jan. 1984.
- [42] S. Grevskott, T. Rusten, M. Hillestad, E. Edwin, and O. Olsvik, "Modelling and simulation of a steam reforming tube with furnace," *Chem. Eng. Sci.*, vol. 56, no. 2, pp. 597–603, Jan. 2001.

CHAPTER 4

Dynamic Operability Analysis and Start-up of an Integrated Radiant Syngas Cooler and Steam Methane Reformer

The contents of this chapter have been submitted for peer review in the following journal:

J.H. Ghouse, D. Seepersad, T.A. Adams II, Dynamic Operability and Start-up of an Integrated Radiant Syngas Cooler and Steam Methane Reformer, AIChE Journal, 2016 (Submitted)

4.1 Introduction

In an entrained-bed gasifier, product synthesis gas (commonly called “syngas”, a mixture of hydrogen and carbon monoxide) exits the gasifier section at high temperatures of upto 1350°C and has to be cooled for downstream unit operations [1]. The hot coal-derived syngas is cooled by employing a radiant cooler or quench cooling section or both in series. In the RSC section of conventional entrained-bed gasifiers, the cooling is provided by generating high pressure steam within tubes placed inside the radiant cooler. However, Adams and Barton [2] proposed a different cooling strategy by replacing high pressure steam generation with the highly endothermic steam methane reforming process. The proposed configuration while providing the required cooling to the hot coal-derived syngas also has other significant advantages:

- (i) Increased system level efficiency as a result of process integration,
- (ii) A valuable syngas stream with a high molar H_2/CO ratio (greater than 4) is produced via the steam methane reforming reactions.
- (iii) In a number of industrial processes, coal-derived syngas, which has a low molar H_2/CO ratio, is upgraded using external reformers or water gas shift reactors to meet the feed requirements for downstream methanol synthesis and liquid fuels production. With the integrated configuration, the hydrogen rich syngas from methane reforming can be blended with the coal-derived syngas to meet the desired H_2/CO molar ratio.

Adams and Barton [2] showed that a polygeneration system which employed the integrated concept was technically feasible and economically desirable from a systems-level perspective. However, in their analysis, only a simple zero-order model was used for the integrated device which did not capture the complexities of high temperature heat transfer, heterogeneous reaction kinetics, and safety constraints on the temperature of the various materials used in its construction. As such, there were many unanswered questions about the range of operating conditions at which the device could safely operate, how well it would perform, and what the actual design parameters should be (such as tube lengths, number of tubes, diameters, and arrangement).

To answer these questions, detailed dynamic heterogeneous models for the proposed integrated system were developed and analyzed [3]. The model accounted for spatial and temporal variations in key variables like temperature, concentration and pressure in the gas phase on the RSC shell and SMR tube side, where methane reforming reactions occur. The model was then utilized to develop a base-case design for two different configurations; co-current flow and counter-current flow. The results showed that a

feasible design existed for both configurations subject to the process requirements and operating constraints but with different advantages and disadvantages for each configuration. For example, not only was the natural gas processing capacity higher for the counter-current configuration but a higher methane conversion of close to 90% was observed in the counter-current configuration. However, the disadvantage of the counter-current configuration was the proximity of the maximum tube wall temperature to the design limit of 1350 K. Furthermore, a sensitivity analysis was performed to assess the effect of certain model parameters on the overall performance. Finally, using the model for steady-state simulations, a base-case design for the proposed integrated configuration (co-current and counter-current) was established. The reader is referred to Ghouse et al. [3] for a complete description of the design heuristics, steady-state performance studies and the sensitivity results.

A flexible or “agile” polygeneration plant in which the feeds and/or products are changed seasonally, weekly, or even daily in response to market conditions could yield significant financial benefits. For example, Chen et al. [4] demonstrated that if each subsection of a polygeneration process had enough flexibility to transition between 50% and 100% of its maximum capacity on a daily basis, the plant could respond to market conditions over the course of its life time enough to increase its net present value by 17% compared to a plant that always operates at the same steady-state. At maximum flexibility (between 0% and 100% of capacity), the net present value increases up to 62%. Similarly, one of the main advantages of the proposed device is that it can be used in a similar fashion, changing the feed amounts or product amounts in response to market conditions. However, with the proposed design, the gasifier itself remains at steady state, which is a desirable property since gasifiers are rarely used dynamically in an industrial setting.

Therefore the main objective of this work is to study the flexibility of the integrated device in the context of a polygeneration plant. The quality of the syngas produced from the integrated system can be altered by manipulating the operating variables. However, it is critical to ensure that such transitions to new operating points are safe and feasible. This study helps in determining the safe operating envelope and the extent to which it can be used for agile polygeneration. Furthermore, the effect of gasifier disturbances on the system performance and a start-up procedure is established and simulated.

4.2 Flexibility in Syngas Yield and H₂/CO ratio at Steady-state

As mentioned in the introduction, one of the key advantages anticipated for the proposed integrated system is the ability to vary the molar H₂/CO ratio of the blended syngas (hydrogen and carbon monoxide) depending upon the downstream process requirements, thereby eliminating the need for upgrading the coal-derived syngas using water gas shift reactors. For the designs that were established previously, the production rates and mole fraction of the syngas produced at steady-state is listed in

Table 6 [3]. The coal-derived syngas and reformed syngas can be blended in different ratios to get the desired H₂/CO molar ratio in the blended syngas. However, the amount of blended syngas available at a particular H₂/CO ratio limits the final yield of the desired products. To this end, two different blending modes are used for this study for a polygeneration plant; Mode 1 and 2. Mode 1 uses all of the available coal-derived syngas and different fractions of the natural gas-derived syngas for blending while Mode 2 uses all of the gas-derived syngas and different fractions of the coal-derived syngas are added to the blend. Figure 21 and Figure 22 shows the production capacity of the blended syngas for different molar H₂/CO ratios for co-current and counter-current configurations respectively.

Table 6: Feed and production capacity at steady-state for co-current and counter-current designs

Parameter	Co-current Design		Counter-current Design	
	Reformer	Gasifier	Reformer	Gasifier
Natural Gas/Coal Feed (TPH)	17	102	19	102
Syngas Produced (TPH)	20	123	27	123
Product Composition:				
Methane	0.032	-	0.018	-
Water	0.355	0.166	0.343	0.137
Carbon Monoxide	0.075	0.332	0.096	0.304
Hydrogen	0.452	0.359	0.469	0.387
Carbon Dioxide	0.061	0.143	0.049	0.172

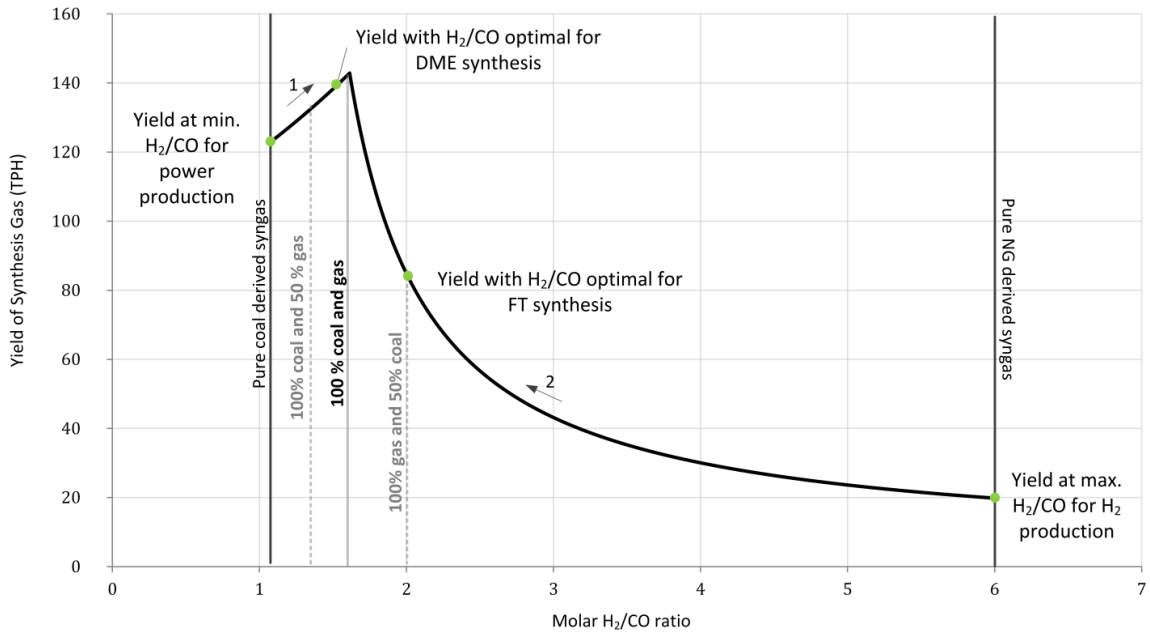


Figure 21: Syngas yields with different H₂/CO ratios for co-current configuration

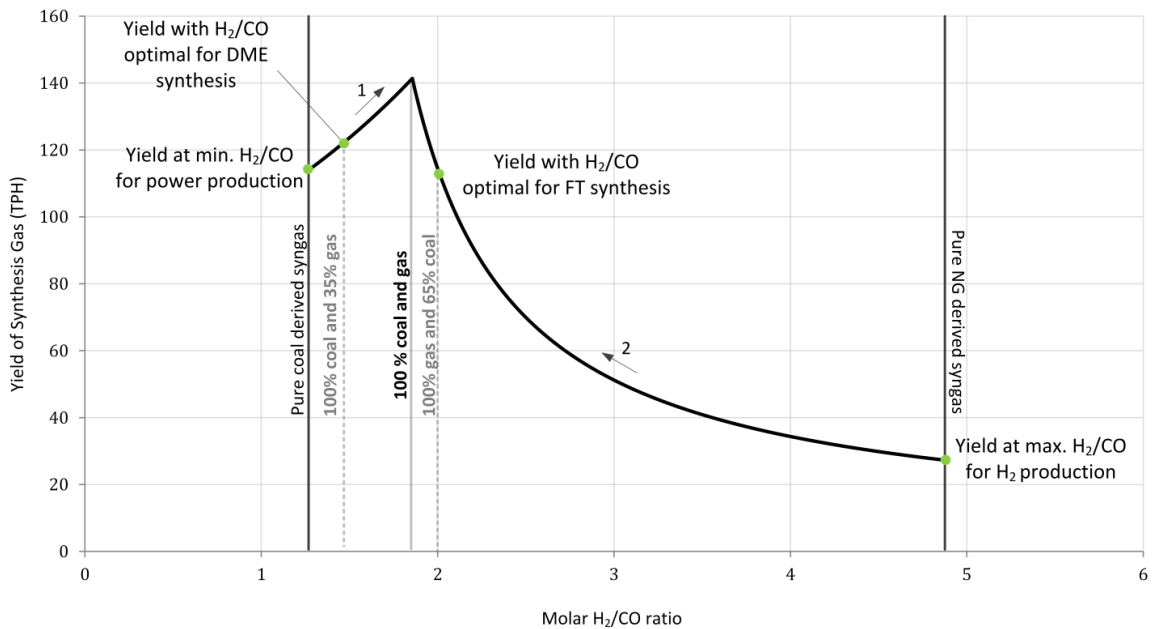


Figure 22: Syngas yields with different H₂/CO ratios for counter-current configuration

Figure 21 shows that for the co-current configuration, the molar H₂/CO ratio ranges from 1.1 (pure coal-derived syngas) to 6 (pure gas-derived syngas). Using mode 1, the H₂/CO

ratio can be varied from 1.1 to 1.6 with a corresponding minimum capacity of 123 TPH to a maximum capacity of 143 TPH when 100% of the reformed syngas is used for blending with the coal-derived syngas. The resulting H_2/CO ratio from mode 1 is compatible for Dimethyl Ether (DME) synthesis for which the feed molar H_2/CO ratio requirement typically ranges from 1.2-1.5 [5]. On the contrary, mode 2 yields a molar H_2/CO ratio between 1.6 and 6. In mode 2, the molar H_2/CO ratio of 2 that is desirable for Fischer-Tropsch (FT) liquids [6] or methanol production [7] is achieved by blending 50% of the coal-derived syngas with the reforming derived syngas. Furthermore, higher molar H_2/CO ratios are available for hydrogen production although at lower syngas flow rate of 20 TPH. For the counter-current configuration, shown in Figure 22, the operating line for syngas flow rates versus the molar H_2/CO ratio is similar to that of the co-current configuration. However, the quality of the blended syngas is different for counter-current configuration. For example, the H_2/CO ratio of pure coal-derived syngas is higher at 1.3 owing to the increased water gas shift reaction in the radiant cooler for the counter-current design. The yield of syngas suitable for DME synthesis is lower than that available for the co-current design but the requirement is achieved by blending just 35% of the reformed syngas with the coal-derived syngas. Also, at maximum yield of 141 TPH, the syngas H_2/CO ratio is higher at 1.85. For FT synthesis, the amount of syngas is available is 101 TPH which is 25% higher than the amount available for the co-current design. The disadvantage with the design may be the maximum H_2/CO ratio that can be achieved with the counter-current configuration is 4.8 which is less favourable for the production of high purity hydrogen. This shows that there are different advantages to be gained with the co-current and counter-current configurations. It is also important to note that the aforementioned flexibility analysis in syngas H_2/CO ratios and capacity for polygeneration is done at steady-state. In the following sections, the ability to safely transition from one operating condition to another will be analysed.

4.3 From Steady-state to Dynamic Simulations

The model for the integrated system was implemented and solved in gPROMS v3.7.1 [8]. The system of partial differential and algebraic equations were discretized in space using the method of finite differences. The reader is advised to refer to Ghouse et al. [3] for a detailed account of the solution techniques and grid size employed to simulate the integrated system. The steady-state operating point that was established for the co-current and counter-current configuration (outlined in Table 6) was used as the initial state for all the dynamic simulations presented in this work to mimic a scenario where the system is subjected to changes from a steady-state operating point. To achieve this in gPROMS, the following commands are used: (i) "SAVE", (ii) "RESTORE" and (iii) "REASSIGN". The

“SAVE” function saves the state of all variables at any point (the steady-state operating point in this instance) while the “RESTORE” function is used to restore a saved variable set to initialize the simulation from that particular operating point, and the “REASSIGN” function is used to change input variables to the model (i.e. inducing step changes or disturbances to the system).

In this work, dynamic case studies are performed in open loop to assess the system dynamics and determine constraints that might impede the desired dynamic operability characteristics of the integrated system. Furthermore the integrated system is subjected to disturbances on the shell side to determine unsafe operating conditions, if any. It should be noted that unlike traditional steam methane reformers where the heat supply to the tubes can be altered effectively by controlled the firing of the burners in the furnace [9], the heat supply to the reformer tubes cannot be controlled in the case of the proposed integrated system as the heat is from the coal-derived syngas on the shell side. This leads to a difficult but interesting scenario in which the integrated system can only be controlled with the SMR tube side variables while treating any change on the shell side as a disturbance and simultaneously ensuring that the required cooling duty is provided to the coal-derived syngas and the operating constraints are not violated.

4.4 Changes to Tube Side Variables

4.4.1 Effect of Feed Inlet Temperature

The feed temperature on the tube side was subjected to a step change of ± 50 K at time 500s. Figure 23 shows the effect of the step change on exit tube and shell gas temperatures, catalyst core temperature at different axial positions along the length of the reactor, change in steady-state outer tube wall temperatures and methane conversion for the co-current configuration. Figure 23A shows that the exit tube gas temperature shows inverse response and changes by 4 K for a ± 50 K change in feed temperature while the shell gas temperature changes by 6 K. Though there is a 75s lag before changes are noticeable at the shell exit, the dynamics of the system fast approaches a new steady-state after 450s. Also, from Figure 23C it is observed that the change in catalyst core temperatures at different axial positions is negligible except at the inlet where the temperature change reflects the change in the inlet gas temperature. The new steady-state temperature for the outer tube wall does not violate the design limit and the change from the previous steady-state is uniform throughout the length except between 0.5 m and 3 m

as shown in Figure 23B. The reason for this change in trend is that a +50 K step change in temperature at the inlet speeds the endothermic reaction thus reducing the temperature while a -50 K step change slows the endothermic reaction thus increasing the temperature. However the same effect is not reflected along the remaining length of the tube. For the most part, the step changes in feed inlet temperature do not affect the methane conversion significantly with the resulting change being only around 2.5 percentage points as shown in Figure 23D. The inlet gas temperature has an inverse response on the syngas H_2/CO ratio. For +/- 50 K change in the feed temperature, the molar H_2/CO ratio of the syngas changes from 6 to 5.8 and 6.2 respectively. The magnitude of change in the H_2/CO ratio can be greater if the change in the inlet gas temperature is larger.

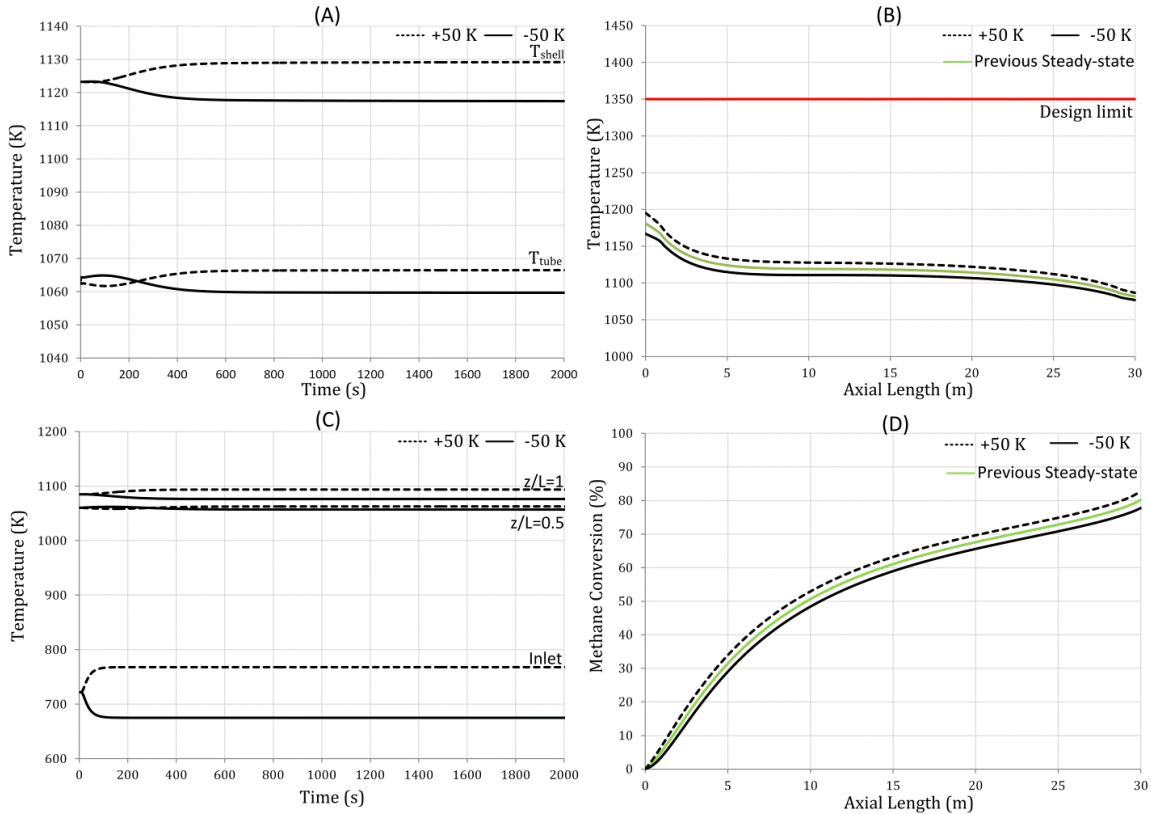


Figure 23: Effect of step change of both +50 K and -50 K in inlet temperature for co-current configuration on (a) exit gas temperature leaving the tube and shell, (b) axial tube wall temperature, (c) catalyst core temperature at the inlet, exit, and halfway point and (d) axial methane conversion

For the counter-current configuration the effect of a similar step change in the inlet feed temperature is shown in Figure 24. Figure 24A shows that the exit shell gas temperature changes by around 5 K while the exit tube gas phase temperature changes by around 10

K. Though the change in exit gas phase temperature appears to be similar to the co-current configuration, an interesting difference is the time required for the impact of the

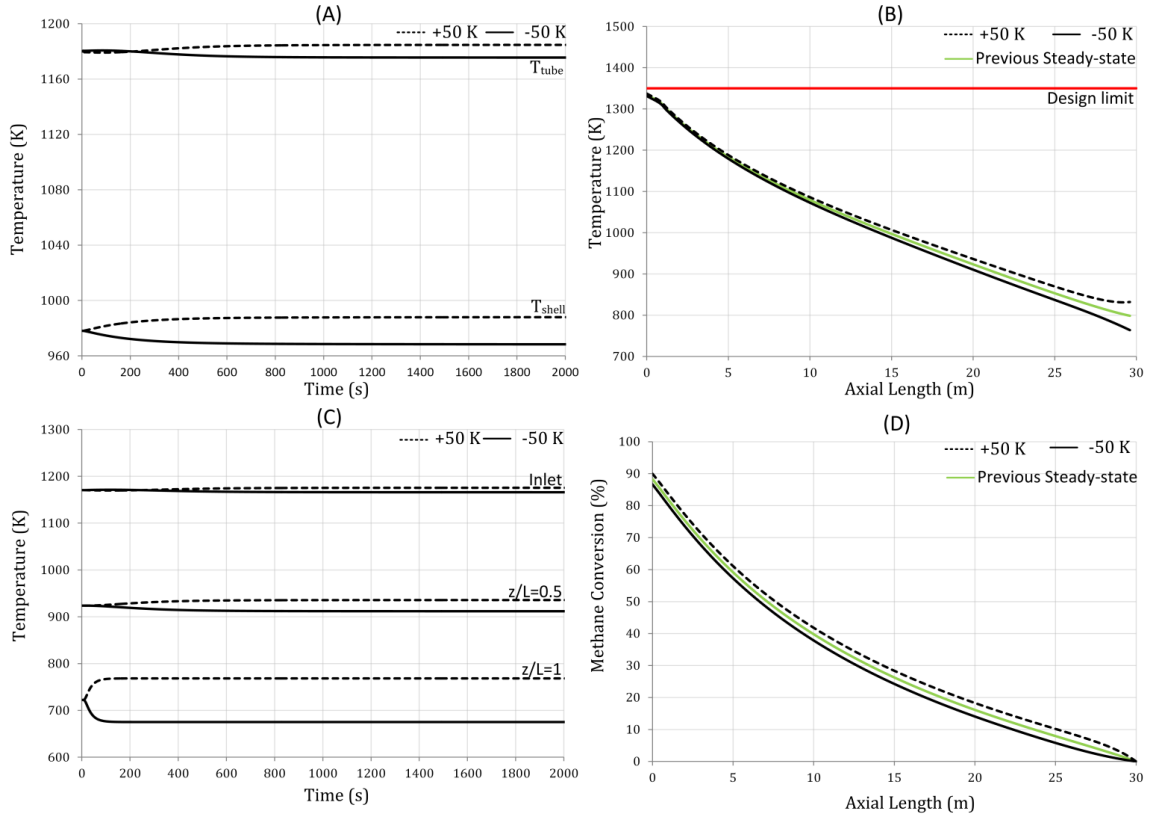


Figure 24: Effect of step change of both +50 K and -50 K in inlet temperature for counter-current configuration on (a) exit gas temperature leaving the tube and shell, (b) axial tube wall temperature, (c) catalyst core temperature at the inlet, exit, and half-way point and (d) axial methane conversion

step change to be reflected at the shell and tube exit for each configuration. The change is reflected immediately in the gas temperature on the shell side because of its proximity to the source of the inlet step change owing to the counter-current configuration, while for the tube exit the time required to reflect the change is around 200s; slower than that for the co-current configuration. With the exit gas temperature usually being the measured variable in conventional SMR systems, the change in the dead time between co-current and counter-current configurations will affect the control design and its efficacy. For the catalyst core temperatures, the change is minor, around 10 K, except at the inlet where the step change occurs. However, the magnitude of the change in the steady-state outer tube wall temperature along the axial length varies and is not a constant as seen in the co-current configuration. This change ranges from 33 K at $z=30$ m (inlet for the tube side) to around 4 K at $z=0$ m (exit for the tube side). Therefore a +50 K change in feed temperature results in the maximum tube wall temperature approaching the design limit

temperature. Also, a similar drop in tube wall temperature close to the inlet is observed owing to the speed of the endothermic reaction. However, the change in methane conversion is 1.7 percentage points which is lower when compared to the co-current configuration. For the counter-current design, the molar H_2/CO ratio changes to 5 when the inlet temperature is reduced by 50 K and to 4.8 when the inlet temperature is increased by 50 K.

4.4.2 Operating at a Lower Steam to Carbon Ratio

Steam is one of the reactants for both the SMR reaction and the water gas shift reaction that occurs in parallel within the tubes. Furthermore, the change in feed steam supply affects the H_2O/C ratio which affects the rate of total methane conversion. In conventional SMR reactors, the typical H_2O/C ratio is greater than 3. One of the other reasons to maintain a high ratio, apart from promoting higher conversion, is to avoid carbon deposition that occurs at H_2O/C ratios of less than 1 [10]. Steam supply is also crucial for driving the forward endothermic reactions thereby consuming the high heat supplied to the SMR tubes; failure will lead to overheating of the catalyst and tube walls. Furthermore, the inlet H_2O/C ratio has a significant impact on the molar H_2/CO ratio in the reformed syngas. Therefore, in the following section a 50% reduction in steam supply is simulated which results in an inlet H_2O/C ratio of 1.6.

For the co-current configuration, the steam supply was reduced by 50% and introduced as a step change. The effect of the change in the inlet H_2O/C ratio on the exit tube and shell gas temperature, tube wall temperature, catalyst core temperature and methane conversion is shown in Figure 25. Figure 25A shows that the exit gas temperature on both the shell and tube side increase owing to the net reduction in flow rate on the tube side. The tube gas exit temperature increases by 118 K while the change in shell gas exit temperature is lower at 72 K. Though the temperature of the gas phase increases, the rate of the endothermic reaction decreases as a result of decreased reactant concentration and this is reflected in the decrease in methane conversion by 18 percentage points from the base-case 80% as shown in Figure 25D. Figure 25C shows that the catalyst core temperature increases slowly but the change in temperature is around 76 K at 15 m and 120 K at the exit. The outer tube wall temperatures also show a significant change. The temperature increases near the inlet by 43 K but at the centre and exit the temperature increases by around 71 K and 104 K respectively. However, the maximum tube wall temperature is well within the specified design limit temperature of 1350 K. Though the system is able to handle the step change without violating any of the constraints considered in this

analysis, other practical limits to the rate of temperature increase of the commercial catalyst and tube walls should also be considered in practice. However, it should be noted that here the change was introduced as a step change and such sharp increase in temperatures can be avoided by subjecting the system to a ramp change or a series of small step changes. Furthermore, the effect of a low H_2O/C ratio has a significant effect on the product molar H_2/CO ratio. The molar H_2/CO ratio decreases from 6 to 4 when the inlet H_2O/C ratio is reduced from 3.3 to 1.6. Therefore, the inlet steam can be used to manipulate the reforming syngas molar H_2/CO ratio as desired for downstream process requirements. These results also show that the H_2O/C ratio can be potentially used as a manipulated variable to control the rate of reaction without violating any of the operating constraints.

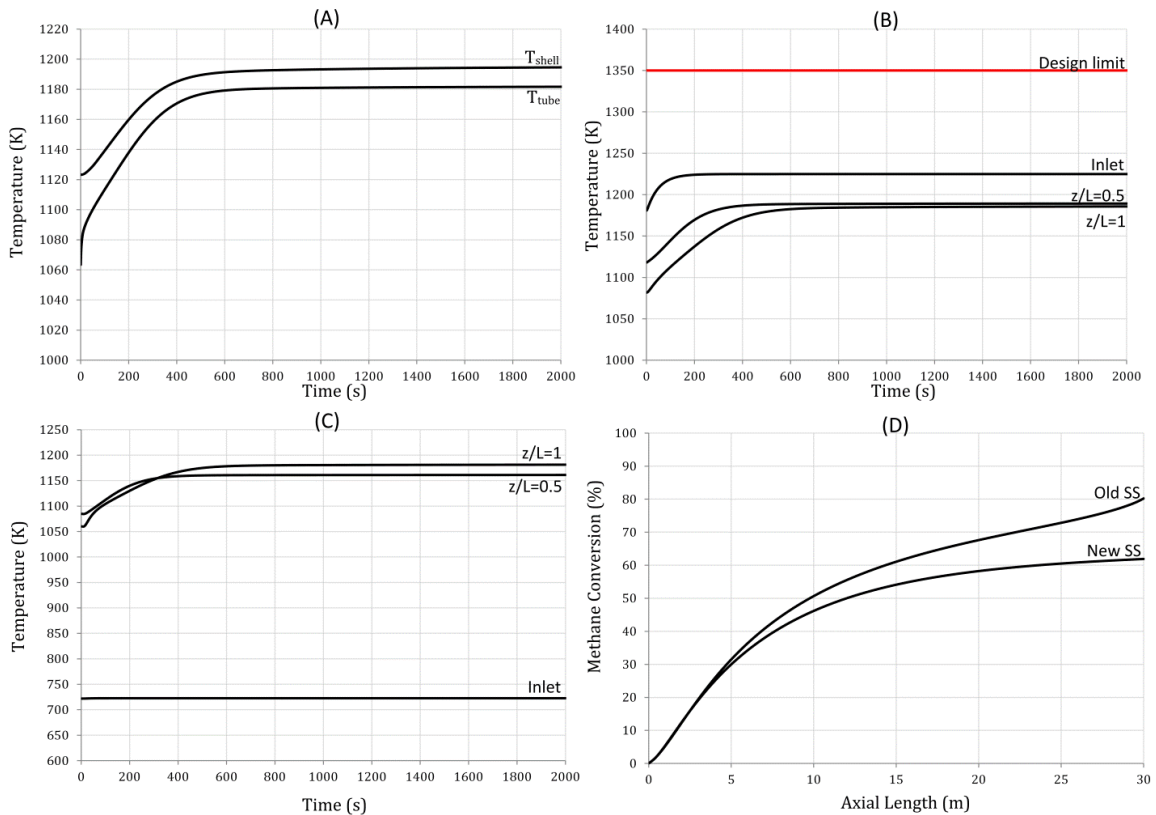


Figure 25: Effect of 50% reduction in inlet steam supply for co-current configuration on (a) exit gas temperature leaving the tube and shell, (b) tube wall temperature at the inlet, exit, and halfway point, (c) catalyst core temperature at the inlet, exit, and halfway point and (d) axial methane conversion

A similar change was simulated for the counter-current configuration and its effect on shell and tube exit gas temperature, outer tube wall temperature, catalyst core temperature and methane conversion is shown in Figure 26. In Figure 26A, it can be seen that the tube exit gas temperature changes by as much as 126 K while the shell gas exit temperature changes by 45 K. As observed in the co-current configuration, the catalyst core temperature changes significantly; 129 K at the tube gas exit and 88 K at 15 m. Though the methane conversion drops by only 10 percentage points shown in Figure 26D, the major drawback is that the outer tube wall temperature near the tube gas exit breaches the design limit in 15s as shown in Figure 26B. It is important to note that the base case steady-state maximum tube wall temperature was very close to 1350 K which limits its flexibility for transient modes of operation. For the counter-current configuration, the product molar H_2/CO ratio decreases from 5 to 3.5, but more importantly, the design cannot safely transition to a new operating steady-state.

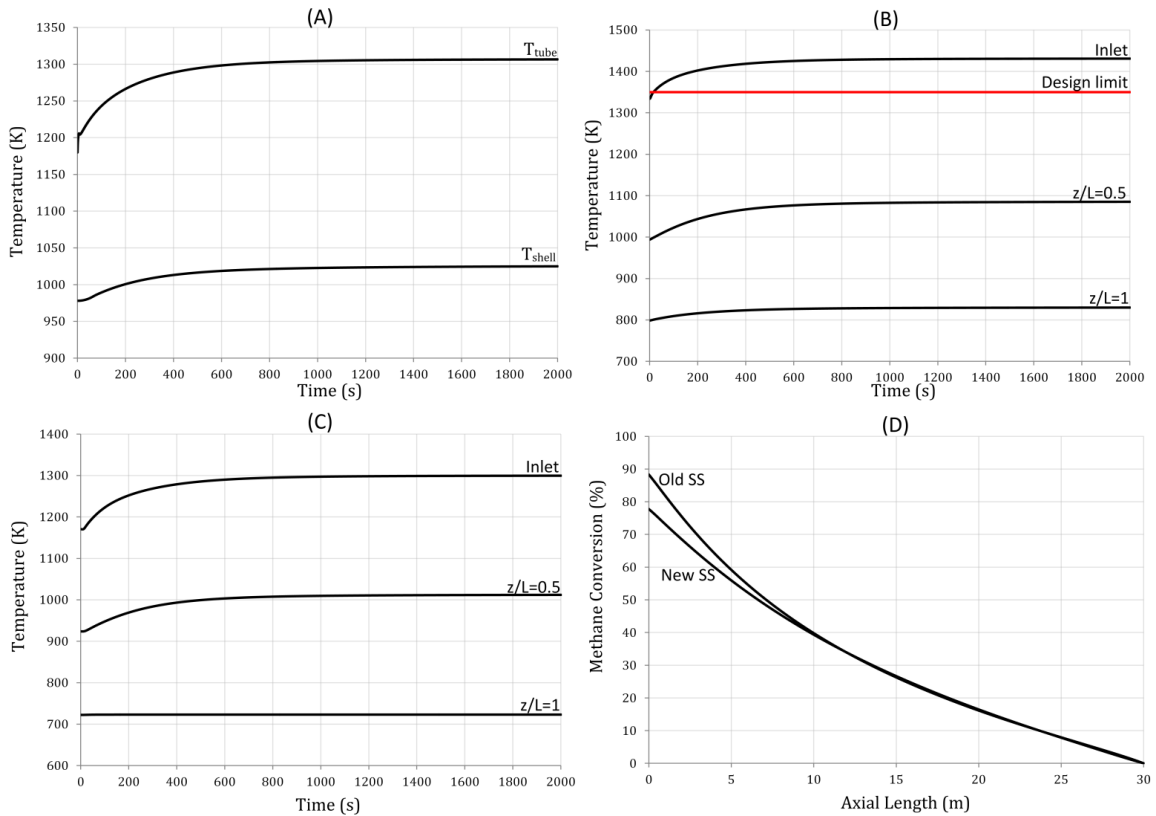


Figure 26: Effect of 50% reduction in inlet steam supply for counter-current configuration on (a) exit gas temperature leaving the tube and shell, (b) tube wall temperature at the inlet, exit, and halfway point, (c) catalyst core temperature at the inlet, exit, and halfway point and (d) axial methane conversion

4.4.3 Operating the Reformer at Reduced Capacity

One of the advantages that were envisaged for the proposed integrated system was the flexibility to operate it dynamically. The feed flow to the SMR tubes (containing the mixture of steam and natural gas) is subjected to a step decrease of 25% to simulate a scenario where the demand for products is low and to determine if the integrated system can handle a lower throughput. The effect on gas exit temperatures, outer tube wall temperatures, catalyst core temperatures and methane conversion for the co-current configuration is shown in Figure 27. Figure 27A shows that the exit gas phase temperatures on both the shell and tube sides increase owing to lower throughput through the tubes and reach a new steady-state in 600 s. The magnitude of change of the shell gas temperature is 65 K while for the tube gas temperature it is 110 K. Though the shell gas exit temperature increases to 1188 K, the increase in temperature can be easily handled by the downstream quench cooler [11]. Also, from Figure 27B it can be observed that though the outer tube wall temperature increases, it is still well within the design limit. The rate of temperature increase is faster at the inlet than at other positions along the axial length. Figure 27C shows that the catalyst core temperature at the centre and at the exit changes by 67 K and 113 K respectively. Owing to the increase in temperature of the gas and catalyst phase, the endothermic reactions move forward resulting in a higher methane conversion of 83% from the previous 80% as shown in Figure 27D. Figure 28 shows the effect of the reduced reformer feed on the yield of blended syngas and molar H_2/CO ratio. The operating envelope shifts to the left of the steady-state operating point where the maximum yield of syngas remains nearly constant but with different H_2/CO ratios. The turn down in reformer feed may be beneficial for downstream processes. For example, the available syngas feed drops by almost 40% for FT synthesis and 20% for DME synthesis which may be beneficial when the production of liquid fuels has to be decreased, such as in a flexible polygeneration plant which produces more power production during the day time and more fuels at night. The results further demonstrate the effect of the system temperature on the H_2/CO ratio of the syngas – an increase in temperature affects the rate of the WGS reaction that decreases the moles of hydrogen and increases the moles of carbon monoxide in the syngas.

For the counter-current configuration, the effect of a step decrease in feed flow to the SMR tubes is shown in Figure 29. Figure 29A shows that the change in shell gas exit temperature is only 20 K while the tube gas exit temperature increases rapidly to 1350 K. As observed with other case studies for counter-current configuration, Figure 29B shows that the outer tube wall temperature exceeds the design limit immediately at the tube exit.

The catalyst core temperature near the exit increases by 180 K which can damage the catalyst; although such hot spots are not observed at any other axial position as shown in Figure 29C. Owing to the very high temperature, the methane conversion reaches as high as 96%, though this is irrelevant since the step change leads to tube material failure. This result clearly demonstrates that the counter-current configuration is not as flexible as the co-current configuration to handle lower feed rates. This means that the co-current configuration may be more desirable from a systems perspective, since the increased flexibility would enable more flexibility of the polygeneration system in which it is used.

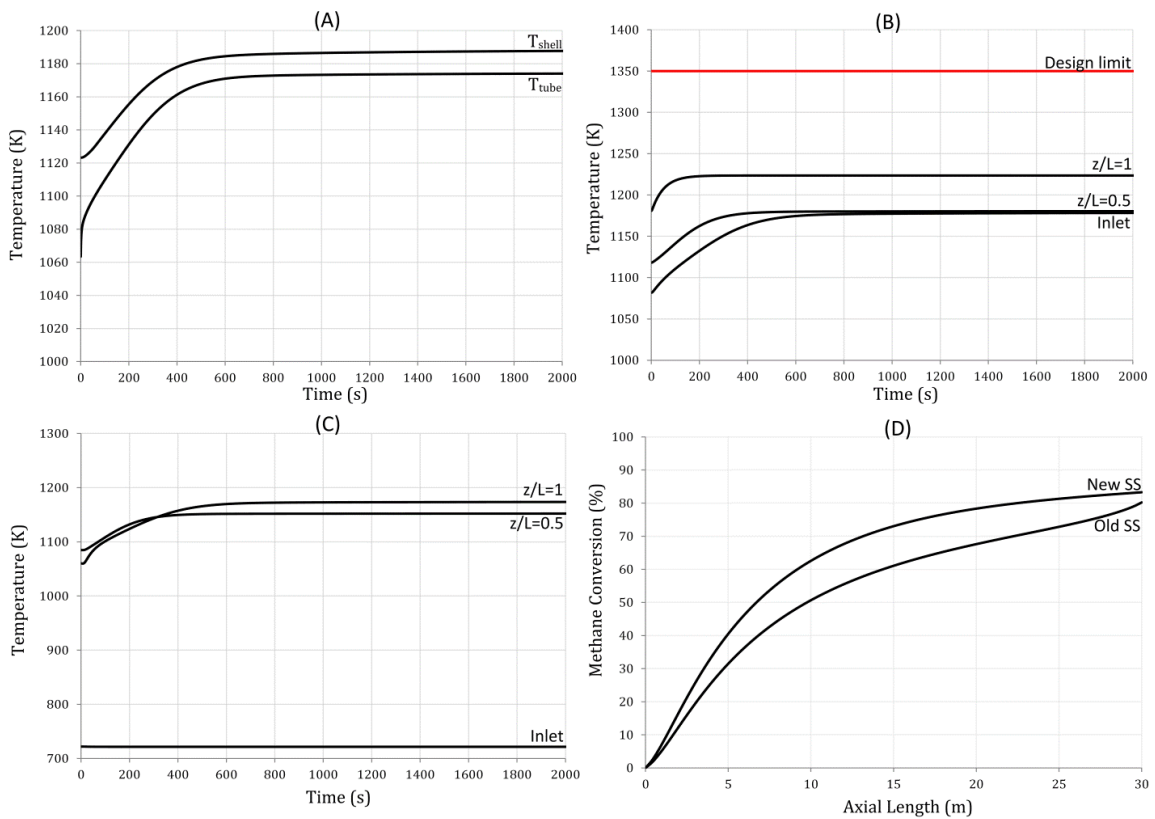


Figure 27: Effect of step decrease in total SMR feed by 25% for co-current configuration on (a) exit gas temperature leaving the tube and shell, (b) tube wall temperature at the inlet, exit, and halfway point, (c) catalyst core temperature at the inlet, exit, and halfway point and (d) axial methane conversion

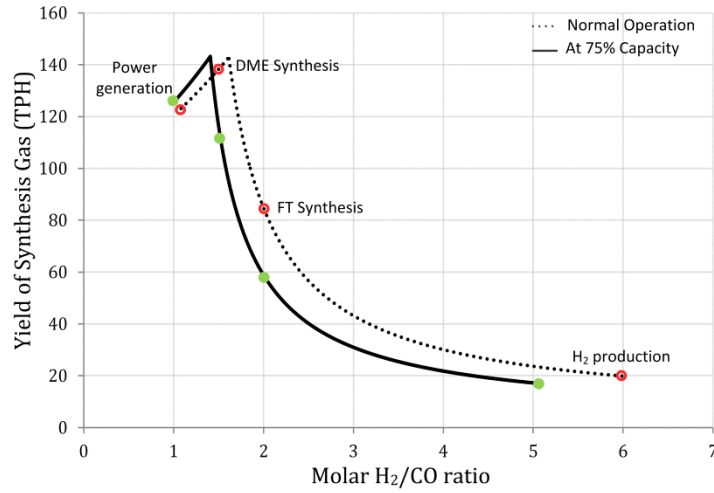


Figure 28: Effect of reduced SMR feed on syngas yield and H_2/CO ratio for co-current configuration

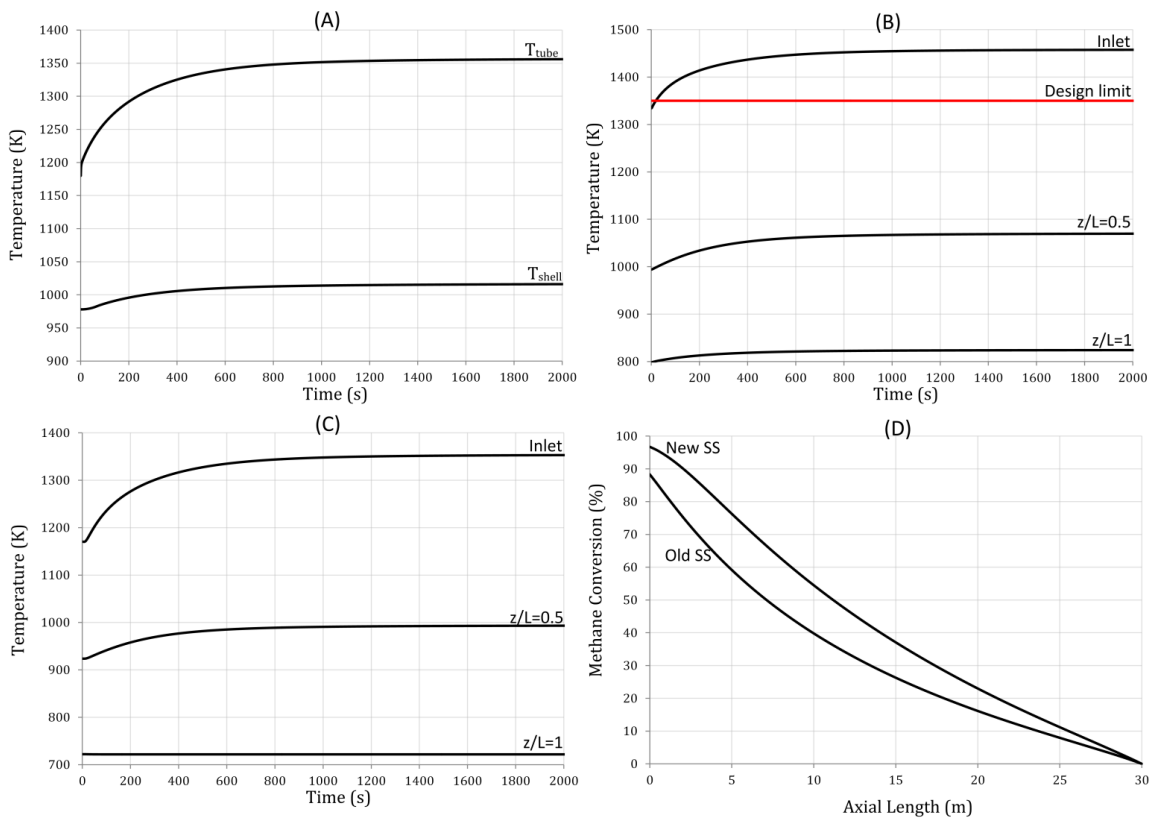


Figure 29: Effect of step decrease in total SMR feed by 25% for counter-current configuration on (a) exit gas temperature leaving the tube and shell, (b) tube wall temperature at the inlet, exit, and halfway point, (c) catalyst core temperature at the inlet, exit, and halfway point and (d) axial methane conversion

4.5 Changes to Shell Side Variables

In this section, changes are made to the shell side variables at the inlet of the RSC. As these variables cannot be controlled in the integrated system, the changes are considered to be disturbances rather than step changes in controlled inputs. However, one case study is presented where the flow rates on the shell side are decreased by 50% to simulate load-following scenarios of advanced gasifiers that can operate dynamically.

4.5.1 Fluctuations in Gasifier Exit Temperature

The gasifier exit temperature which is the inlet shell gas temperature was subjected to a +25 K disturbance for 300s. The response of different variables on the shell and tube side is shown in Figure 30. Figure 30A shows the tube gas phase temperature at different lengths along the axial domain. It can be seen that the change in gas phase temperature is only around 8 K along the entire length. Also, for the response to be reflected at the tube exit takes considerable time owing to the co-current configuration. The results show that the integrated system is capable of handling the temperature disturbance as the exit shell gas temperature increases by only about 6 K before returning to the previous steady-state point shown in Figure 30B. Figure 30C and Figure 30D show that the tube wall temperature and catalyst core temperature are not affected by much. The outer tube wall temperature at the inlet shows a maximum change of 19 K before returning to the nominal operating temperature. Furthermore, the mole fraction profiles on both the shell and tube exit do not show any change and the system is able to survive the temperature disturbance easily even when operating in open loop. Though a larger disturbance than 25 K could have been simulated, it is rare that significant changes to the gasifier exit temperatures occur during operation even at reduced loads [12].

A similar disturbance was introduced for the counter-current configuration and the response is shown in Figure 31. Figure 31A shows the effect of the disturbance on the tube gas phase temperature at different positions along the axial length. Unlike the co-current configuration, where the effect is observed across the entire length, the effect is seen only at the tube exit because of the mode of operation with the tube exit being close to the point of disturbance. In addition, the shell exit temperature changes by a maximum of 2 K showing that the system is able to handle the disturbance effectively. Figure 31C shows that the outer tube wall temperature near the tube exit exceeds the design limit by a maximum of 20 K for a period of 220s during which the disturbance occurs. Though the

catalyst core temperature and exit mole fraction profiles on the shell and tube side stay approximately constant, the ability of the counter-current configuration to handle the disturbance depends on the tube material that will be used.

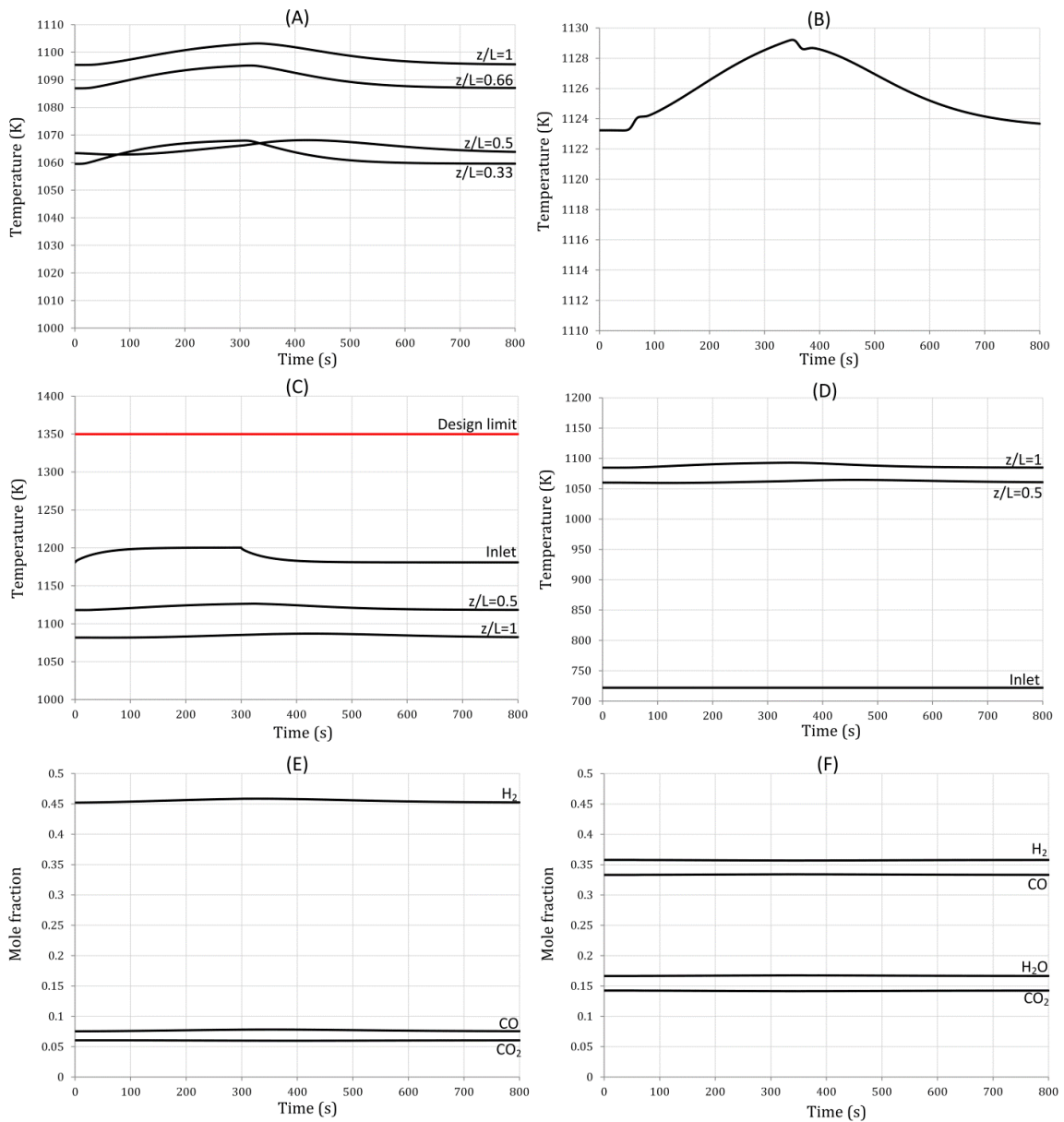


Figure 30: Effect of +25 K disturbance in inlet shell temperature for 300s in co-current configuration on (a) tube gas temperature at different axial points, (b) exit shell gas temperature, (c) tube wall temperature at the inlet, exit, and halfway point, (d) catalyst core temperature at the inlet, exit, and halfway point, (e) exit tube syngas mole fraction and (f) exit shell syngas mole fraction

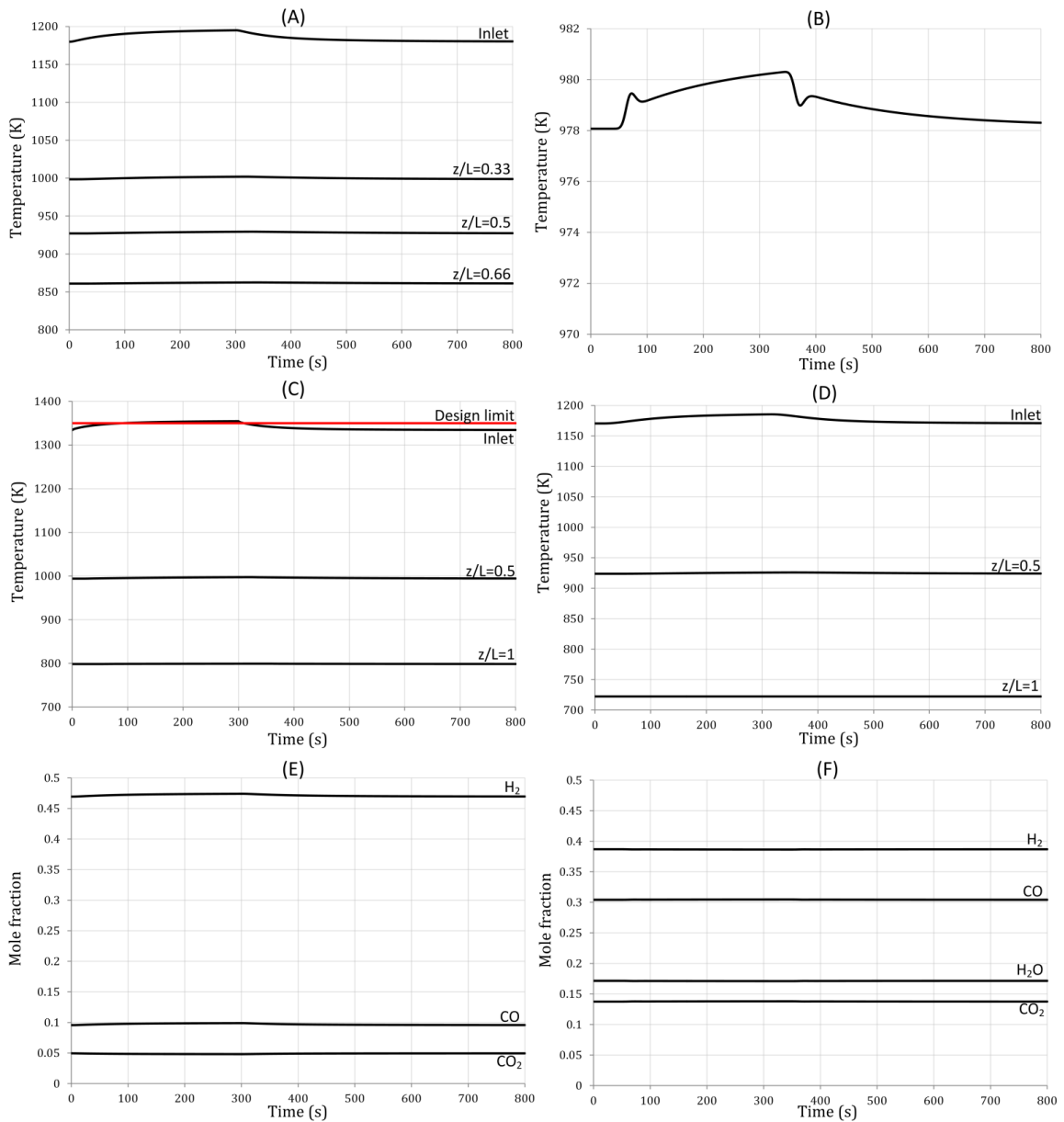


Figure 31: Effect of +25 K disturbance in inlet shell temperature for 300s in counter-current configuration on (a) tube gas temperature at different axial points, (b) exit shell gas temperature, (c) tube wall temperature at the inlet, exit, and halfway point, (d) catalyst core temperature at the inlet, exit, and halfway point, (e) exit tube syngas mole fraction and (f) exit shell syngas mole fraction

4.5.2 Disturbance in the Gasifier Syngas Flowrates

A shell-side inlet flow rate disturbance of 5% was simulated for both the co-current and counter-current configurations for 300s and the response of the key variables is shown in Figure 32 and Figure 33 respectively. The exit shell and tube gas temperatures, shown in Figure 32A for the co-current configuration, change marginally by a maximum of 8 and 5 K, while the outer tube wall temperature and catalyst core temperatures along the axial length show negligible change from their steady-state values. The disturbance has a minor effect on the SMR reactions inside the tubes as shown by the exit mole fraction profiles in Figure 33D. The counter-current configuration also responds in a similar way and is able to survive the disturbance in open loop with no loss in performance.

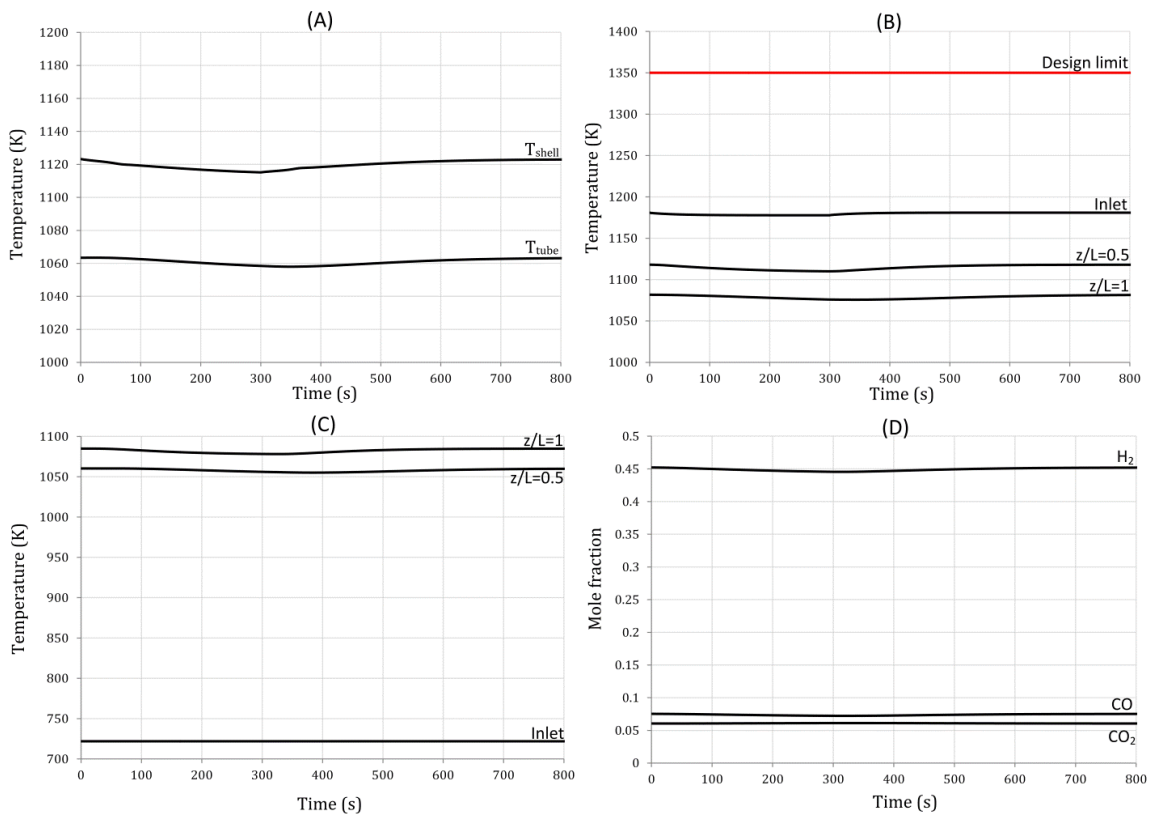


Figure 32: Effect of 5% disturbance in inlet shell flow rate for 300s in co-current configuration on (a) exit gas temperature leaving the tube and shell, (b) tube wall temperature at the inlet, exit, and halfway point, (c) catalyst core temperature at the inlet, exit, and halfway point and (d) tube side exit syngas mole fraction.

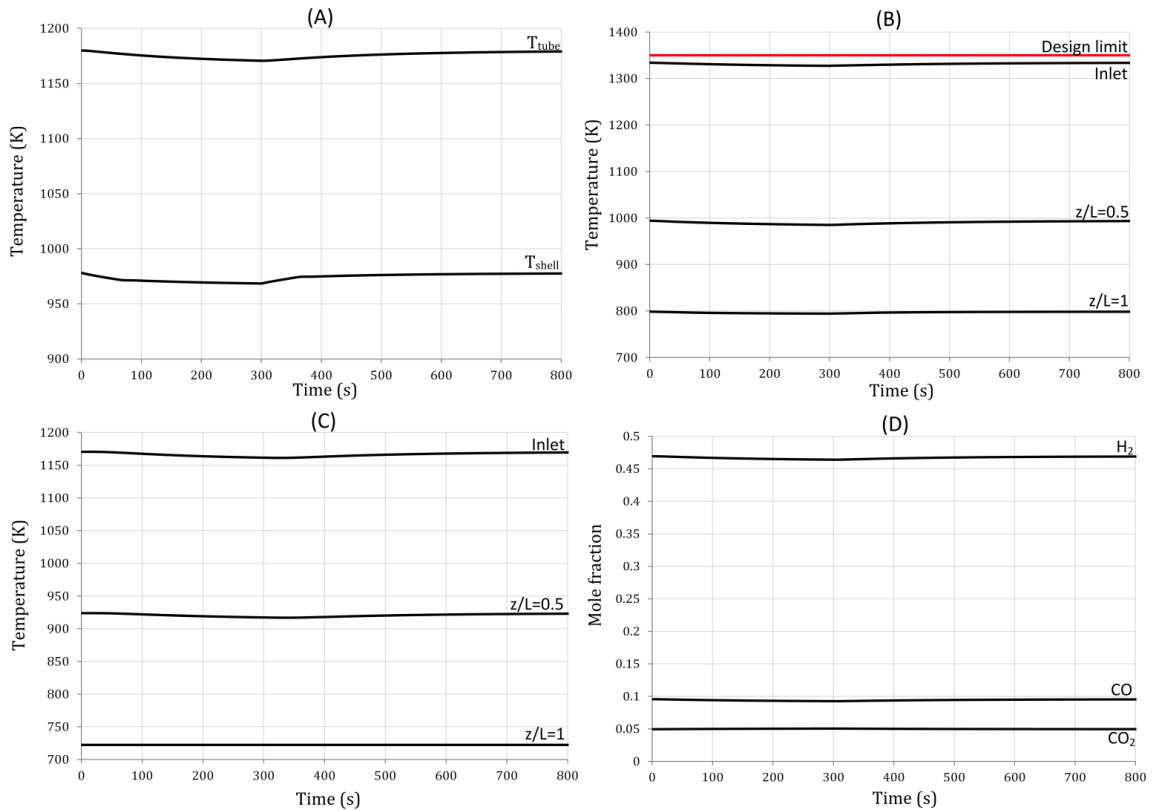


Figure 33: Effect of 5% disturbance in inlet shell flow rate for 300s in counter-current configuration on (a) exit gas temperature leaving the tube and shell, (b) tube wall temperature at the inlet, exit, and halfway point, (c) catalyst core temperature at the inlet, exit, and halfway point and (d) tube side exit syngas mole fraction.

4.5.3 Step Decrease in Gasifier Feed (50% drop)

A step decrease of 50% in the coal-derived syngas at the RSC inlet was simulated. For the co-current configuration, the resulting effect on key variables is shown in Figure 34. Figure 34A shows that the exit gas phase temperatures in both shell and tube decrease slowly and take 1000s to reach new steady-states. The coal-derived syngas is further cooled to around 1000 K owing to higher residence time in the RSC and no change in flow rates on the tube side. Following a similar trend, the tube wall temperature and catalyst core temperature also decrease as shown in Figure 34B and Figure 34C. With the heat supply to the tubes decreasing owing to reduced throughput on the shell side, the methane conversion drops significantly to 50%. However the response here is in open-loop, and it will be interesting future work to see if an efficient control system can

maintain the desired exit methane conversion and product mole fraction by regulating the inlet feed flow rate to the tubes.

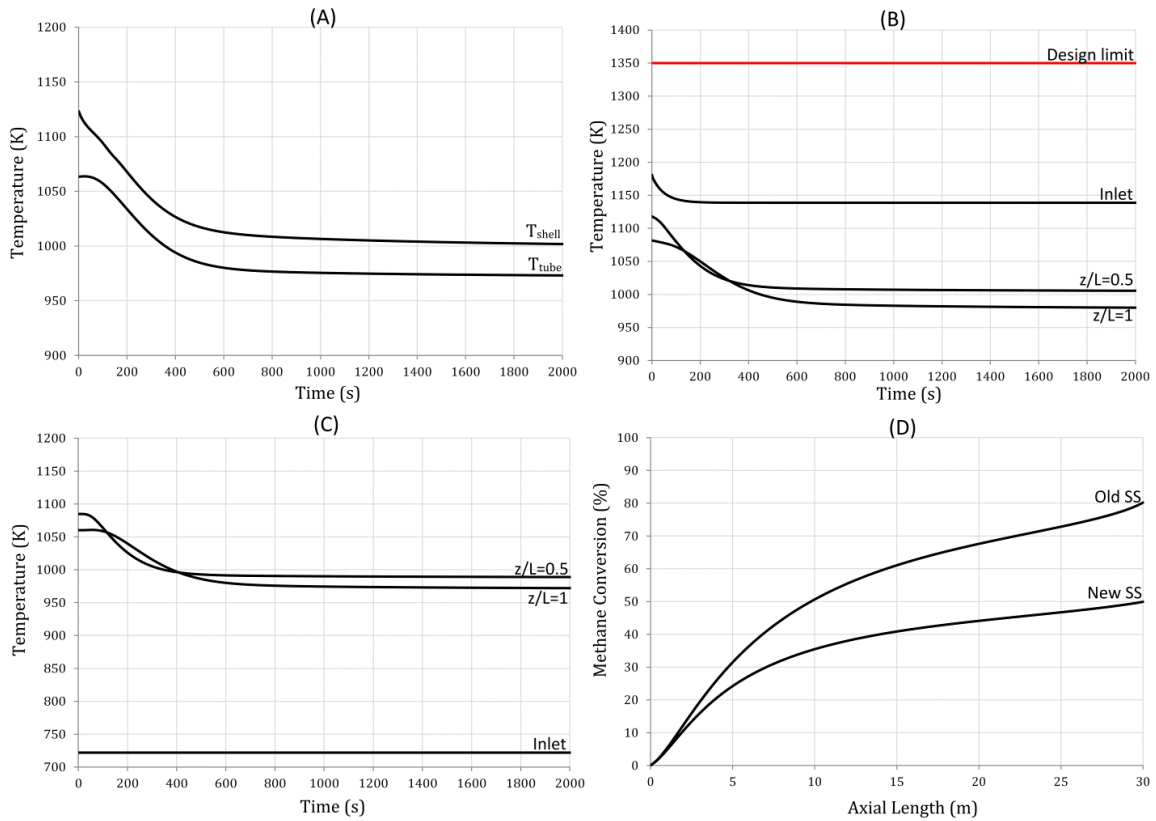


Figure 34: Effect of step decrease in coal-derived syngas feed by 50% for co-current configuration on (a) exit gas temperature leaving the tube and shell, (b) tube wall temperature at the inlet, exit, and halfway point, (c) catalyst core temperature at the inlet, exit, and halfway point and (d) axial methane conversion

For the counter-current configuration, the system response to a similar change is shown in Figure 35. The shell gas temperature decreases by 125 K to 850 K while the exit tube gas temperature drops to 1060 K. Figure 35B shows that the maximum tube wall temperature at the tube exit moves further away from the design limit temperature and reaches 1240 K. Though the magnitude of change is different from the co-current mode, the trends are similar with the catalyst core and tube wall temperatures decreasing. Also, the methane conversion drops as expected but the change is higher at 33% points. Both sets of simulations demonstrate that in the event the gasifier is to be turned down for load following purposes or in the event of a failure of one of the coal hoppers where the feed drops significantly, the integrated system can operate safely.

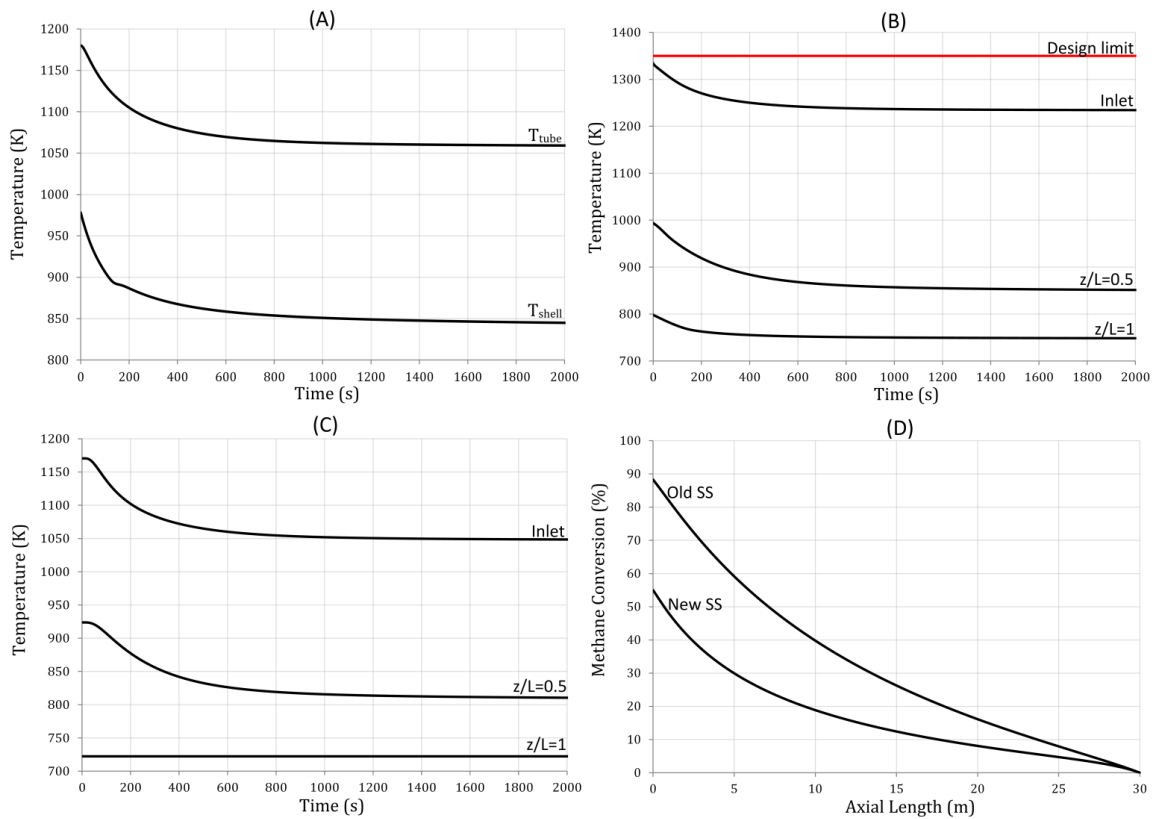


Figure 35: Effect of step decrease in coal-derived syngas feed by 50% for counter-current configuration on (a) exit gas temperature leaving the tube and shell, (b) tube wall temperature at the inlet, exit, and halfway point, (c) catalyst core temperature at the inlet, exit, and halfway point and (d) axial methane conversion

4.6 Open Loop Start-up of the Co-current Configuration

The simulations for the transient modes of operation in the previous sections demonstrated that the co-current configuration is safer to operate in transient modes than the counter-current configuration for flexible polygeneration. However, the transient modes are initiated from an operating steady-state that was established in our previous study. Though the designs show flexible operation, the question remains if the integrated system can reach the operating steady-state from a cold start condition. Furthermore, the start-up procedures for the gasifier and steam methane reformer are complex even when operated independently and hence, the start-up procedure for the integrated system needs to be investigated. In the current study the start-up procedure for the integrated system has been adopted from existing industrial practices that are used for gasifier and steam

reformer start-ups. This methodology helps to establish a realistic start-up procedure for the integrated system.

Typically, for an entrained-bed gasifier, the start-up is done by slowly increasing the refractory temperature over a period of two days. Natural gas burners are employed to increase the system temperature and coal feed is introduced once the gasifier operating temperatures are reached. The critical constraint during the start-up is the maximum allowed heating rate of the refractory layer of the gasifier which is usually limited to 10-20°C/min [13]. Monaghan and Ghoniem [12] simulated the start-up of a GE entrained bed gasifier using dynamic models that were implemented in Aspen custom modeller such that the heating rate is less than 10°C/min for the refractory. However, in all of the aforementioned references there were no details about the operation of the radiant syngas cooler during the start-up. It is assumed that the radiant cooler is brought online at some point during the start-up until which the quench cooler is employed to cool the natural gas combustion gases.

Contrary to the gasifier start-up, the steam reformer start-up is relatively fast but it involves a series of steps to ensure that the reformer tubes are not damaged. The first step in the reformer start-up usually involves nitrogen circulation through the reformer tubes [14], [15]. Simultaneously, the furnace burners are ignited and the system temperature is slowly increased such that no hot spots are formed on the tube walls. Steam is then introduced into the tubes but is only done when the reformer tube exit temperature is higher than that of the dew point of the steam being introduced. This is important to ensure that steam does not condense on the catalyst which may later expand when heat duty to the reformer is increased resulting in an explosion and damaging the tubes [16]. After steam injection, the reformer is allowed to reach the operating temperatures at which point natural gas is slowly introduced. During this phase, a high H₂O/C ratio is maintained. The natural gas feed is then slowly increased to the rated capacity and the steam injection is altered to meet the desired H₂O/C ratio at the inlet.

For the integrated system, the start-up procedure has been established based on the procedures that are currently implemented for the individual systems. However, for the integrated system there are some limitations: First, unlike in a conventional reformer where the furnace temperature can be controlled, the shell side temperature cannot be controlled during the start-up which may affect the reformer operation. Second, the start-up time scales for the reformer and the gasifier are different which means that the reformer comes online before the gasifier. In this study, the gasifier was not modelled but the gasifier exit temperature serves as inlet conditions for the radiant cooler. The gasifier exit temperature was simulated using regressed models as a function of time based on the

simulation data from Monaghan and Ghoniem [12], [17] for a GE entrained-bed gasifier. The gasifier exit temperature increase rapidly for the first hour when natural gas and air is combusted in the burner, after which the temperature gradually increases until coal feed is introduced. For the reformer, the following sequences of steps are followed:

- (i) Nitrogen is introduced to the reformer tubes and continued until the tube gas exit temperature is greater than 575 K.
- (ii) Nitrogen flow to the tubes is decreased and steam at 550 K is introduced. This was continued until the tube gas exit temperature reached 750 K.
- (iii) Natural gas at 50% of the steady-state capacity (530 kmol/h) is then introduced. The steam flow through the tubes is maintained such that the H_2O/C ratio at the inlet is equal to 5.
- (iv) The H_2O/C is reduced to the operating range of 3.3 after one hour. The natural gas supply is maintained at 50% until the gasifier operating temperature is reached.
- (v) Once the gasifier is online, the natural gas supply to the reformer tubes is increased to 80% of the steady-state operating capacity as the heat load to the reformer tubes increases.
- (vi) The reformer is then slowly brought to 100% capacity with a series of step changes in natural gas flow rates that is made in one hour intervals.

Figure 36 shows the shell and reformer gas temperature profiles during the start-up. The reduced order model for the RSC inlet temperature ensures that the trajectory is similar to that occurring during a gasifier start-up. It can be seen that the tube gas exit temperature increase rapidly in the first two hours that allows for the natural gas feed to be introduced within three hours from start-up. The high H_2O/C ratio when natural gas is introduced initially increases the rate of the exothermic water gas shift reaction and thereby increases the reformer gas temperature for a brief period of time. Figure 37 shows the effect of the increased rate of water gas shift reaction on the tube gas mole fraction profiles during this period. The amount of CO_2 at the exit increases rapidly when high H_2O/C ratio is maintained and starts to decrease when the ratio is reset to 3. As the temperature continues to increase gradually, the rate of endothermic reforming reaction increases. The gasifier operating temperature is reached around 21 hours into the start-up at which point natural gas combustion is stopped and coal water slurry is introduced into the gasifier. This change is introduced as a step change in the simulation even though the process takes 2-3 hours during the actual start-up. However, the step change is sufficient to detect any violations in operating constraints. At this stage, the natural gas feed to the reformer tubes is increased to 80% of the capacity at steady-state. The natural gas feed is then gradually increased every hour to the operating capacity of 1061 kmol/hr and the reformer exit temperature continues to drop as the methane conversion increases. The

integrated system takes approximately 40 hours to reach operational steady-state from a cold start initial condition.

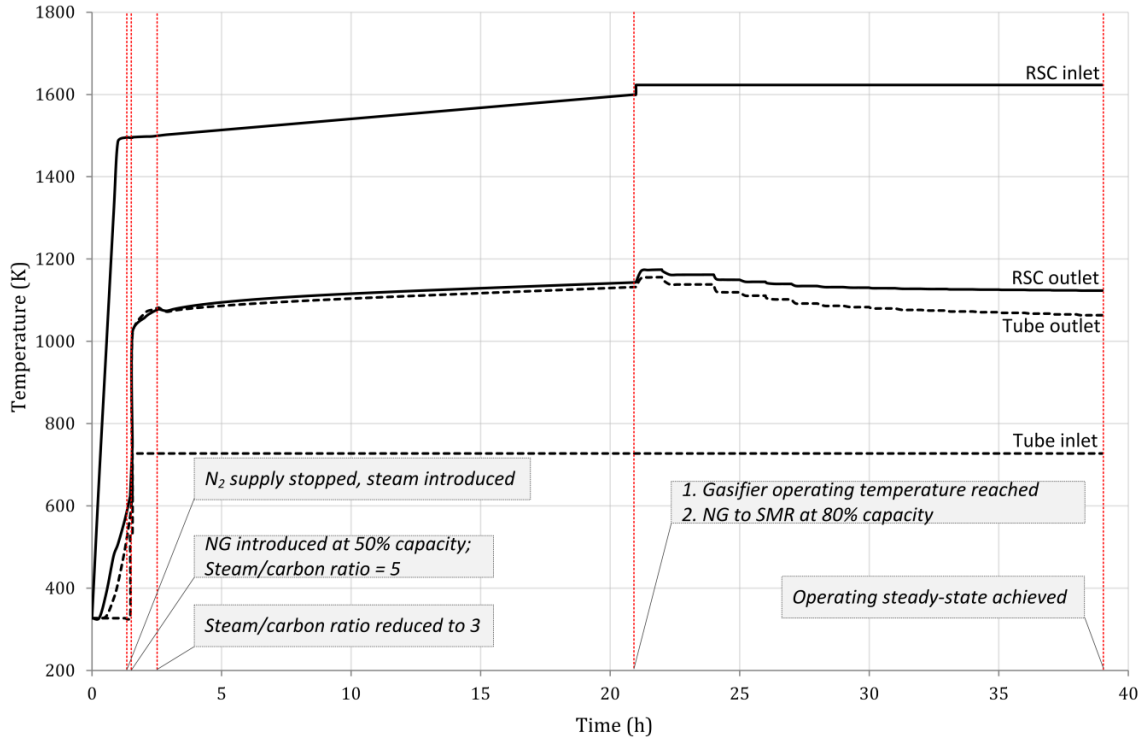


Figure 36: Shell gas and reformer gas temperature profiles during start-up

Figure 38 shows the catalyst core temperature profiles during start-up at different locations along the length of reformer tubes. The profiles show hot spots at $t=21$ hours when the gasifier comes online and when the natural gas feed to the reformer is increased. It can also be observed that the location of the hot spot along the axial direction changes during the course of the start-up. During the first 20 hours of the start-up, the hottest region is nearer to the exit of the reformer. However, the increase in natural gas flow rates when the gasifier comes online results in a higher pressure drop in the reformer tubes. This low pressure near the exit of the reformer further favors the reforming reaction which decreases temperature of the catalyst core near the reformer outlet. Though hot spots are observed during start-up, the temperature gradient is low and shows that the start-up can be done without any damage to the catalyst bed.

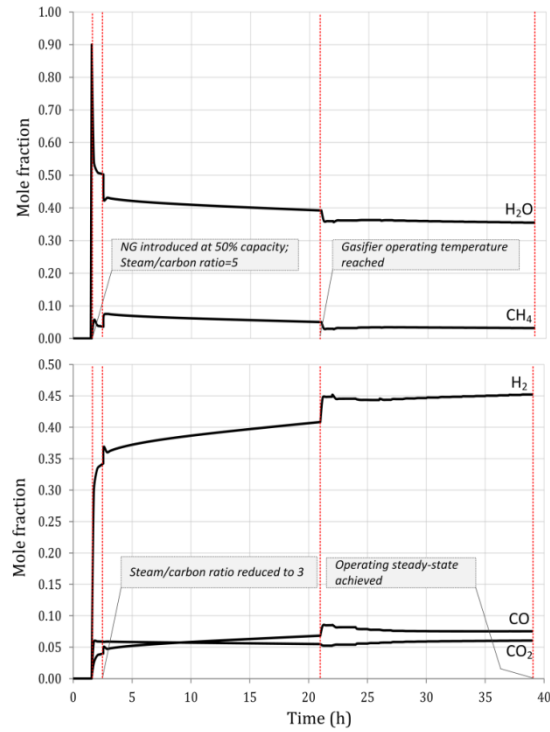


Figure 37: Tube gas mole fraction profiles at reformer exit during start-up

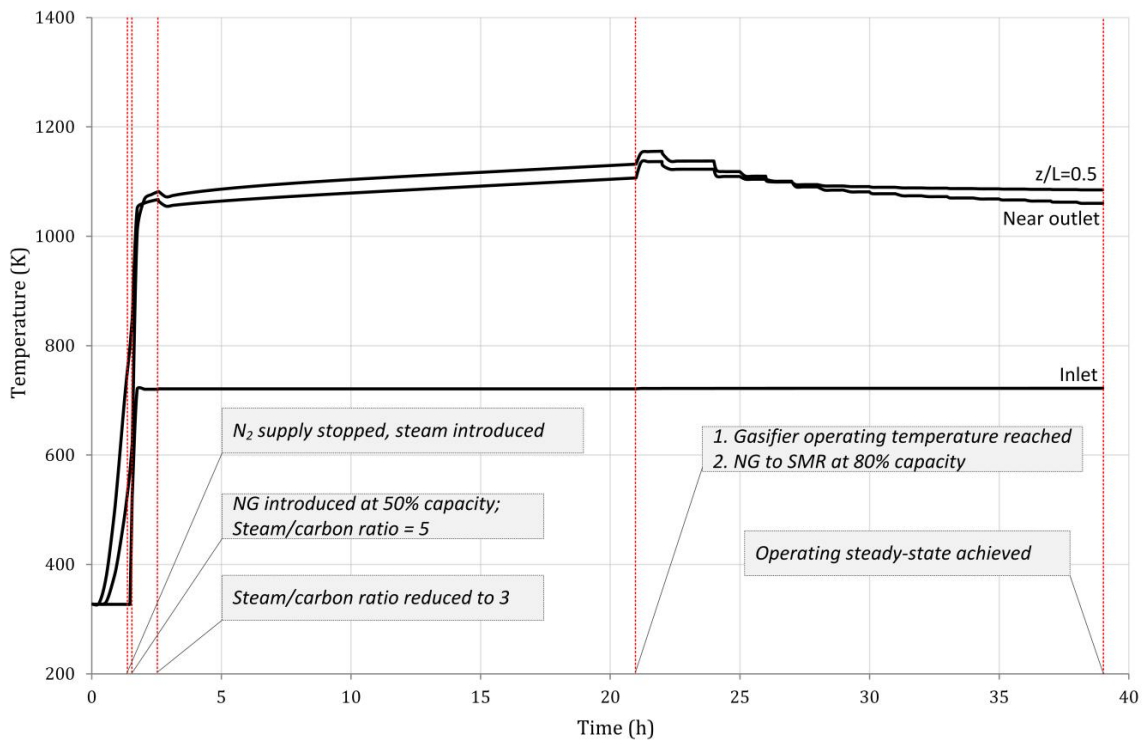


Figure 38: Catalyst core temperature profiles along the reformer tubes during start-up

The other key operational constraint is the maximum tube wall temperature. Figure 39 shows the maximum tube wall temperature during the start-up phase. The maximum temperature does not exceed the design limit temperature of 1350 K for the integrated system. During the start-up phase, the maximum temperature reaches 1214 K when the gasifier comes online but later decreases to a steady-state value of 1180 K as the reformer nears the design capacity.

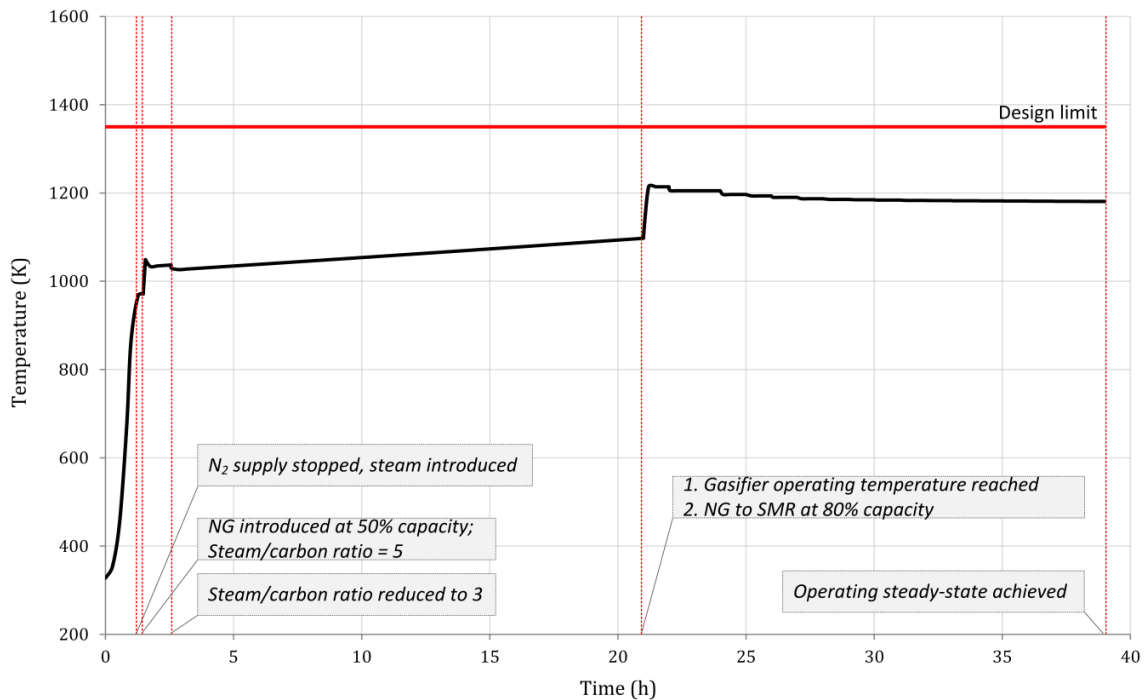


Figure 39: Maximum tube wall temperature profile during start-up

4.7 Conclusions

The first-principles based model that was previously developed for the integrated RSC and SMR was utilized in this work to study the dynamic operability. The system was subjected to step changes in manipulated variables on the reformer side to assess the impact on the integrated system performance. For example, it was observed that the inlet H_2O/C ratio could be an important manipulated variable to control the product H_2/CO molar ratio. The system was also subjected to reduced natural gas and steam feeds (a 25% decrease from the nominal operating point) to the SMR tubes to determine the

dynamic flexibility of the integrated system. The open-loop simulations helped build an understanding of the integrated system dynamics and also helped identify variables that were more likely to violate the operating constraints.

Though the feasibility of the integrated RSC/SMR concept at steady-state was previously demonstrated, it did not shed light in terms of operational safety and flexibility. The results presented in this work show that the co-current configuration, though having reduced methane conversion of 80% compared to the 88% methane conversion in counter-current configuration and smaller processing capacity by design, is more flexible than the counter-current configuration for operations in a transient mode where the shift to a new operating point is feasible. Also, the start-up procedure established for the co-current configuration showed the possibility of safely starting up the integrated system where the natural gas reformer comes online within a few hours from a cold start condition. One of the major drawbacks observed for the counter-current configuration was the limited margin available to withstand disturbances because of the proximity of the maximum tube wall temperature at 1334 K near the RSC inlet to the design limit of 1350 K. At present, it can be concluded that the co-current configuration is the safer and more flexible design option for the proposed integrated system. This design conclusion for the integrated system is consistent with the design philosophy for conventional top-fired steam reformers. In conventional reformers, the feed to the tubes is introduced at the top where the tube wall temperatures are high, ensuring that rate of cooling are highest at the hottest parts of the reformer. However, it is possible that a new design variant of the counter-current configuration could be used which provides additional cooling to the top of the wall through some other means. This would increase the safety margin for the tube wall temperatures while also maintaining the benefits of higher methane conversions. Alternatively, it may be possible to design a control system which is able to reject the disturbances safely for counter-current mode, which is the subject of future work.

4.8 Acknowledgements

Financial support from an Imperial Oil University Research Award, NSERC Discovery Grant and NSERC – Collaborative Research and Development grant are gratefully acknowledged.

4.9 References

- [1] “Tampa Electric Polk Power Station Integrated Gasification Combined Cycle Project - Final Technical Report,” U.S. DOE and Tampa Electric Company, 2002.
- [2] T. A. Adams II and P. I. Barton, “Combining coal gasification and natural gas reforming for efficient polygeneration,” *Fuel Process. Technol.*, vol. 92, no. 3, pp. 639–655, Mar. 2011.
- [3] J. H. Ghouse, D. Seepersad, and T. A. Adams, “Modelling, simulation and design of an integrated radiant syngas cooler and steam methane reformer for use with coal gasification,” *Fuel Process. Technol.*, vol. 138, pp. 378–389, 2015.
- [4] Y. Chen, T. A. Adams II, and P. I. Barton, “Optimal Design and Operation of Flexible Energy Polygeneration Systems,” *Ind. Eng. Chem. Res.*, vol. 50, pp. 4553–4566, 2011.
- [5] W. Cho, T. Song, A. Mitsos, J. T. Mckinnon, G. H. Ko, J. E. Tolsma, D. Denholm, and T. Park, “Optimal design and operation of a natural gas tri-reforming reactor for DME synthesis,” *Catal. Today*, vol. 139, pp. 261–267, 2009.
- [6] Y. K. Salkuyeh and T. A. Adams, “Combining coal gasification, natural gas reforming, and external carbonless heat for efficient production of gasoline and diesel with CO₂ capture and sequestration,” *Energy Convers. Manag.*, vol. 74, pp. 492–504, 2013.
- [7] C. Higman and S. Tam, “Advances in Coal Gasification, Hydrogenation, and Gas Treating for the Production of Chemicals and Fuels,” *Chem. Rev.*, vol. 114, no. 3, pp. 1673–1708, Oct. 2013.
- [8] “gPROMS.” Process Systems Enterprise.
- [9] C. J. Lim and J. R. Grace, “On the Reported Attempts to Radically Improve the Performance of the Steam Methane Reforming Reactor,” *Can. J. Chem. Eng.*, vol. 74, 1996.
- [10] J. Xu, C. M. Y. Yeung, J. Ni, F. Meunier, N. Acerbi, M. Fowles, and S. C. Tsang, “Methane steam reforming for hydrogen production using low water-ratios without carbon formation over ceria coated Ni catalysts,” *Appl. Catal. A Gen.*, vol. 345, no. 2, pp. 119–127, Aug. 2008.
- [11] P. J. Robinson and W. L. Luyben, “Simple Dynamic Gasifier Model That Runs in Aspen Dynamics,” *Ind. Eng. Chem. Res.*, vol. 47, no. 20, pp. 7784–7792, Oct. 2008.

- [12] R. F. D. Monaghan and A. F. Ghoniem, “Simulation of a Commercial-Scale Entrained Flow Gasifier Using a Dynamic Reduced Order Model,” *Energy & Fuels*, vol. 26, no. 2, pp. 1089–1106, Feb. 2012.
- [13] K. V.S. and B. I.P., “Determining the maximum possible rates of single sided heating of refractories,” *Ogneupory*, no. 4, pp. 51–55, 1971.
- [14] Asia Industrial Gases Association, “Safe Startup and Shutdown Practices for Steam Reformers.” 2013.
- [15] European Industrial Gases Association AISBL, “Combustion Safety for Steam Reformer Operation.”
- [16] M. Rogers, “Lessons Learned From an Unusual Hydrogen Reformer Furnace Failure,” Fort McMurray, Alberta, 2005.
- [17] R. F. D. Monaghan, “Dynamic Reduced Order Modeling of Entrained Flow Gasifiers by,” MIT, 2010.

CHAPTER 5

Application and Optimal Designs of Proposed Integrated System for Biomass Based Polygeneration

The contents of this chapter have been accepted in the following peer reviewed conference proceeding:

J.H. Ghose, T.A. Adams II, Optimal Design of an Integrated Radiant Syngas Cooler and Steam Methane Reformer using NLP and Meta-heuristic Algorithms, Computer Aided Chemical Engineering, 2016 (Accepted)

5.1 Extension of the integrated design to a biomass gasifier

Owing to the successful demonstration of operational feasibility and design of an integrated coal gasifier and steam methane reformer, an integrated biomass gasifier and steam methane reformer was proposed for a polygeneration system producing liquid fuels. For a gasifier that processed 100 TPH of biomass feed, an integrated design was required that provided a minimum methane conversion of 65% and a cooling duty of 40 MW. Based on the results from Chapters 3 and 4, the co-current design was chosen as the preferred design for the biomass based gasifier. A base-case design was established, using the heuristics outlined previously, that met the process specifications. The base-case design parameters are outlined in Table 7. The design was able to achieve a methane conversion of 70% and provided 41 MW of cooling to the biomass derived syngas. The reformer exit temperature was 1090 K and the pressure drop across the tubes was 7.8 bar when processing 630 kmol/hr of natural gas through the tubes.

Table 7: Base-case design parameters for an integrated SMR and biomass gasifier

Parameter	Value
Length (m)	20
Shell Diameter (m)	4.572
Refractory Thickness (m)	0.15
Tube Diameter (cm)	8.4
Tube Thickness (mm)	8
Number of tubes	138

5.2 The Need for Optimal Designs

The base-case designs are principally based on design heuristics (with trial and error) commonly used for designing catalytic reformers and radiant coolers. Furthermore, until now only retro-fit designs were pursued where the dimensions of the shell were kept consistent with existing designs. Though several feasible designs were established, many of the degrees of freedom were not sufficiently explored and therefore the existing results are suboptimal. Therefore, an optimization-based approach was used in this study to optimize the design parameters shown in Figure 40. Note that only co-current configuration was considered as they are more feasible to operate than the counter-current designs. As the model was implemented in gPROMS, the deterministic solver (NLP) feature within gPROMS was utilized at first to optimize the design. However, though efficient and applied widely, the success of most NLP solvers is highly dependent on

providing feasible initial guesses that necessitates a good understanding of the process being modelled *a priori*. Furthermore, such techniques are inept at handling inherent model discontinuities. Procedures for finding good initial guesses, especially for large first principle models, are cumbersome. Meta-heuristic techniques like Particle Swarm Optimization (PSO), Differential Evolution (DE) and Simulated Annealing (SA) have been used successfully for large scale models with the aforementioned problems. The major drawback with such techniques is the large computation time required to find an optimal solution. However, the meta-heuristic techniques can be implemented quickly and are highly parallelizable that can effectively use the multicore processors available on personal computers today. In this study, parallel computing versions of DE and PSO were utilized. Therefore, the primary objective in this study is to optimize the integrated radiant syngas cooler and steam methane reformer design using both deterministic and meta-heuristic techniques, and determine which optimization method is the most suitable for problems of this type.

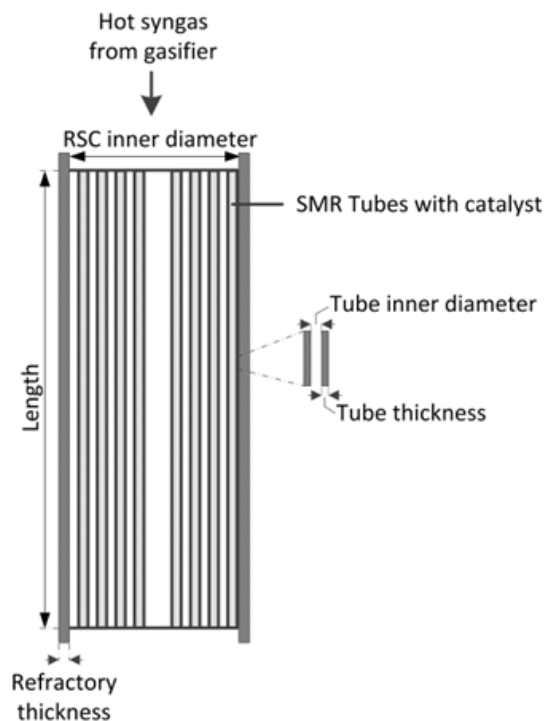


Figure 40: Design variables for the proposed co-current integrated RSC-SMR design

5.2.1 Estimating the Capital Cost

Because the proposed integrated device is still at the conceptual stage, vendor quotes cannot be used for capital cost estimates. However, the cost of the individual components required, such as the costs for the materials used for SMR tubes or the refractory bricks, is readily available. Although cost estimates of this type have inherent inaccuracies, they are still useful for comparing one design to another, such that the design with the minimum capital cost estimate should be close to design with the true minimum cost. The capital cost includes the sum of the cost of tubes and the refractory that is calculated based on the weight of material required. The cost was estimated based on the amount of material required for the major parts of the integrated device, such as the tubes and the refractory bricks. The amount of material required for each of these components is a function of the physical dimensions of the integrated device that forms the decision variables for the optimization problem; the inner tube diameter, tube wall thickness, radiant cooler shell inner diameter, refractory thickness, and length of tubes. The optimization model was formulated as follows with constraints imposed for performance (methane conversion) and for material limitations (maximum tube wall and average outer refractory temperature):

Min. Capital Cost

$$s. t. \text{ Methane Conversion} \geq 70\%$$

$$\text{All Local Tube Wall Temperatures} \leq 1200 \text{ K}$$

$$\text{Average Outer Refractory Temperature} \leq 575 \text{ K}$$

Model Equations

The model equations include the mass, energy and momentum balance equations that govern the integrated system implemented in gPROMS. The total number of equations for the dynamic, distributed model equal more than 200,000 after spatial discretisation. Though the model that was developed is dynamic, this study focusses on optimizing the design for performance at steady-state. For more detail, the reader is advised to refer to the previous study [1]. The bounds on the decision variables are provided in Table 8.

Table 8: Lower and upper bounds for the design parameters

Parameter	Lower Bound	Upper Bound
Tube diameter (cm)	7.8	10.2
Tube thickness (mm)	8	15
Shell Diameter (m)	2.5	4.6
Refractory thickness (m)	0.1	0.3
Length (m)	10	30

5.2.2 Deterministic Optimisation Using gPROMS

In gPROMS, dynamic models can be used for steady-state optimisation and two methods are recommended in the software documentation. One method sets the initial condition to be “STEADY-STATE” for the dynamic model. However, the initialisation fails often if the model is large and complex. The other method allows for the dynamic model to be started from any consistent set of initial conditions (that does not need to be at steady state) until steady-state is attained. This is done by selecting the optimisation entity to be “STEADY_STATE” or by using the dynamic optimisation but specifying an end point constraint towards the end of the control interval (the time required for attaining steady-state). When using the optimisation feature in gPROMS, it is important for the user to note that it ignores any commands under the “SCHEDULE” section. Therefore, if the model was written with a series of schedule or switch commands for simulation purposes (commonly applied to help initialise the system); the optimiser will ignore it all. In this study, the latter method was used, where the desired inequality constraints are specified only at the end of the control interval. The NLP solver within gPROMS uses the Sequential Quadratic Programming (SQP) method [2]. However, a good initial condition is required because during optimization, the simulation must be able to transition from that one initial condition to many different steady states depending on the current values of the decision variables.

5.2.3 Implementation of Meta-heuristic Programming on gPROMS Models

As mentioned previously, the first principles model was implemented in gPROMS. The algorithms for DE and PSO were coded in MATLAB using the built-in parallel computing features. The code was then interfaced with gPROMS using gO:MATLAB. The general strategy is shown in Figure 41 and more details on linking gPROMS and MATLAB can be found in the appendix.

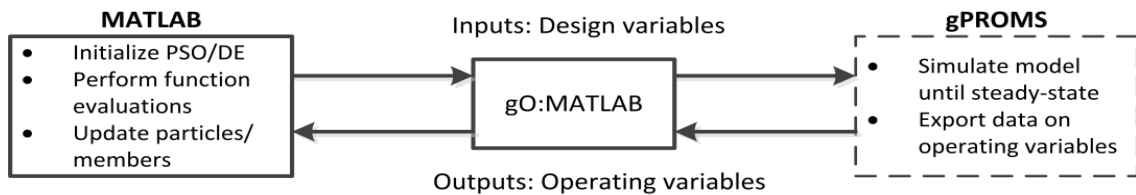


Figure 41: Meta-heuristic programming implementation on a gPROMS model

During implementation, every node in the parallel computing pool requires an independent license to run gO:MATLAB. Therefore, the number of clusters that could be used in this study was constrained by the number of licenses we had for gO:MATLAB: two. To test the effectiveness of using two nodes, a trial run was done where the model in gPROMS was run with forty different operating parameters with and without parallel computing. Furthermore, the effect of restarting gPROMS before every run when a new input is sent was studied. If the model in gPROMS is not coded with a looping feature, the model will have to be restarted for every new simulation when inputs change making it computationally inefficient. However, in the event of a simulation failure, gO:MATLAB automatically restarts the model and is ready to receive the next input. Figure 42 shows the computation time required for these cases. It can be observed that irrespective of the restart feature, the CPU time required to run forty simulations reduces by 45% when the number of processors is doubled. The results also show the importance of efficient coding; for example, avoiding restarts of the gPROMS model provides the same performance as that of a gPROMS model that requires recurring restarts when parallel computing is used.

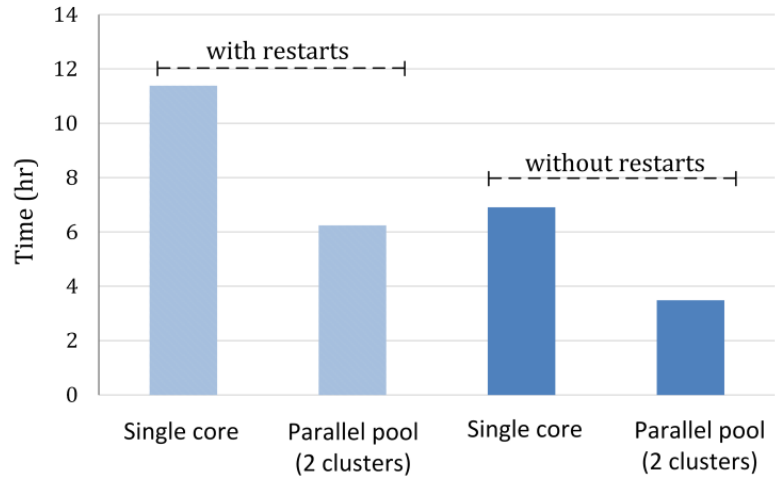


Figure 42: Effect of parallel computing on wall clock time

For the sake of brevity, the algorithms for PSO and DE are not going to be explained in detail. The reader is advised to refer to the books by Price et al. [3] and Gendreau and Potvin [4] for details on the DE and PSO algorithms respectively. The constrained variables were checked for violations after each function evaluation and the objective function was penalized if violations occurred. Also, the initial particles/members (30 for both PSO and DE) were initialized within their bounds but during successive iterations, it is possible that these bounds are violated and several methods exist to reset the variables. In this study, the particles/members were reset randomly within the bounds for DE. For PSO, the sticky boundary condition was adopted, where the particles were reset to the lower or upper bound depending upon the proximity to the bounds. The maximum number of iterations was set at 40 which was one of the termination criteria. The other termination criterion was the proximity of the members or particles at the end of each iteration, and was set at 0.001.

5.2.4 Optimization Results using NLP Solver in gPROMS

The optimization results using the NLP solver in gPROMS for all the cases considered are given in

Table 9 along with the base-case design from the previous work. For case 1, the problem was formulated for a retrofit design as done in our previous study i.e. the shell diameter and refractory thickness were not included in the decision variables. The improvement in capital cost is only 6% when compared to the base-case design. The results validate the design heuristics used for our base-case designs providing a design close to the optimal

solution. In case 2, the retrofit constraint was removed allowing for changes in the dimensions of the shell and refractory. The capital cost reduces significantly and the improvement from base-case design is 60%. The resulting design is compact with the tube length reduced by 44% and the shell diameter by 28%. For case 3, the methane conversion constraint was increased by 10% points to 80%. The resulting problem is feasible and the optimal design parameters are very similar to the results from case 2 except longer tubes are required, leading to a larger residence time that facilitates increased methane conversion. However, it should be noted that the pressure drop across the tube was higher than that of the base-case design. This aids with the methane conversion as lower pressure promotes the reforming reaction but this may be sub-optimal at the systems level. The capital cost is still lower than the base case by 41%. The computation time required for these runs was around 12-18 hours each.

Table 9: Optimal solutions using NLP solver in gPROMS

Parameter	Base Case	Case 1 (retrofit)	Case 2 (new design)	Case 3 (new design, Higher conversion)
Length (m)	20	18.6	12	17
Shell Diameter (m)	4.572	4.572	3.30	3.24
Refractory Thickness (m)	0.15	0.15	0.15	0.15
Tube Diameter (cm)	8.4	9	7.8	7.8
Tube Thickness (mm)	8	8	8	8
Capital (M\$)	25	23.5	10	15
Improvement over base case (%)	-	6	60	41

5.2.5 Optimization Results using Meta-Heuristic Algorithms – DE and PSO

For the meta-heuristic techniques, the particles were initialised randomly within their respective lower and upper bounds using the “rand” function in MATLAB. It should be noted that for the results discussed below, the initial particles did not include the base-case design variables as one of the particles. Though including the base-case values is highly recommended when initializing the members/particles, it was not considered in this study so as to test if the difficult job of finding a good design to use an initial guess could be avoided. For brevity, only the high-conversion scenario described in section 5.2.4 is shown. The results are summarized in Table 10 and are compared to the optimal

solution when using NLP in gPROMS (Case 3 in Table 9). For DE (Case 4), the optimal solution improves the capital cost by 9% and the wall time required even with parallel computing is 11 days. The design variables are very similar to that of the optimal solution using gPROMS except for the length of tubes. Also, the tube length is more than the base-case length of 20 m that might have been avoided by including the base-case design as one of the initial particles. PSO with 30 particles (Case 5) fails to find a better solution than the base case. At termination, the best solution is worse than the base-case design by 38%. However, the major advantage observed was the computation time required when compared to DE. PSO required less than half of the time for DE with the same number of particles. This advantage allows increasing the number of particles in the search space and hence for Case 6, the number of particles was increased by 33% to 40. The PSO is able to find a very good solution close to that of the deterministic solution, which is impressive considering that the heuristic-based design was not used as an initial guess. The wall time was 5 days for Case 6, which would be almost half the wall time as a multi-start method which used the deterministic NLP solver, the same number of initial guesses (40), and two parallel computing nodes.

Table 10: Optimal solutions of the high-conversion scenario using DE and PSO

Parameter	gPROMS NLP (Case 3)	DE (Case 4)	PSO	
			Case 5	Case 6
Length (m)	17	21.3	24.2	18.1
Shell Diameter (m)	3.24	3.59	4.24	3.37
Refractory Thickness (m)	0.15	0.148	0.27	0.16
Tube Diameter (cm)	7.8	7.96	8.4	7.96
Tube Thickness (mm)	8	8	9	8
Capital (M\$)	14.78	22.8	34.6	16.23
Improvement over base case	41	9	-38	35
Wall Time (days)	0.5	11	4	5

5.2.6 Effect of Compact Designs on Performance

From the optimisation results, it can be observed that the optimal designs favour compact designs with smaller tube and gasifier diameters. A sensitivity analysis was done to understand the effect of smaller tube and gasifier diameters on the performance. In the first case study, the tube diameter was changed from 0.084m (base-case) to 0.078m keeping the other design parameters constant. By reducing the tube diameters, more tubes can be placed within the RSC shell. In Table 11, the effect of this change on number of tubes, inlet mole flow per tube and superficial velocity is presented. It can be seen that

though the molar flow rate per tube decreases, the reduced cross sectional area increases the inlet velocity of the gas in the tubes. Figure 43A and Figure 43B show the effect of the smaller tube diameter on pressure and Reynolds number of the gas phase within the tubes. The pressure drop through the tube increases for tubes with a smaller diameter owing to the increased superficial velocity. The low pressure towards the exit of the reactor tube favours higher methane conversion (the forward reaction) based on Le Châtelier's principle. Furthermore, the higher velocity within the tubes increases the turbulence which aids in heat and mass transfer. Figure 43C shows that owing to the increased turbulence in smaller tubes, the total heat transferred to the catalyst phase increases. In addition, the mass transfer coefficient of methane, shown in Figure 43D, increases by 27% at the center of the tube.

Table 11: Effect of tube diameter on design and operating parameters

Tube diameter	0.084 m	0.078 m
Number of tubes	138	147
NG feed per tube (mol/s)	4.20	3.95
CSA (m ²)	0.0055	0.0048
Superficial velocity (inlet) (m/s)	1.57	1.71

Similarly, for the second case study, the RSC diameter was changed from 4.6m to 3.5m. Though the tube diameter is kept constant, the reduction in RSC diameter reduces the cross sectional area which limits the number of tubes that can be placed within the shell. Table 12 shows the effect of this change on the number of tubes, the molar flow per tube and the inlet velocity of gas in tubes. Figure 44A and 44B show a similar effect on the tube gas pressure and the Reynolds number. It is interesting to note that the smaller gasifier diameter has a more pronounced effect on the tube side pressure drop and Reynolds number than that observed for a smaller tube diameter. Furthermore, the total heat transferred to the catalyst increases (as observed previously) but is higher which may be due to the increased heat transfer on the outside of the tubes from the shell side gas. A similar increase is also observed with regard to the mass transfer coefficient of methane from the gas to catalyst phase. Due to these effects, the methane conversion increases by 0.6 percentage points (for change in tube diameter) and by one percentage point (for change in shell diameter). These results validate the solutions obtained through optimization and also help understand the interacting effects of the tube and gasifier diameter on the performance of the integrated system.

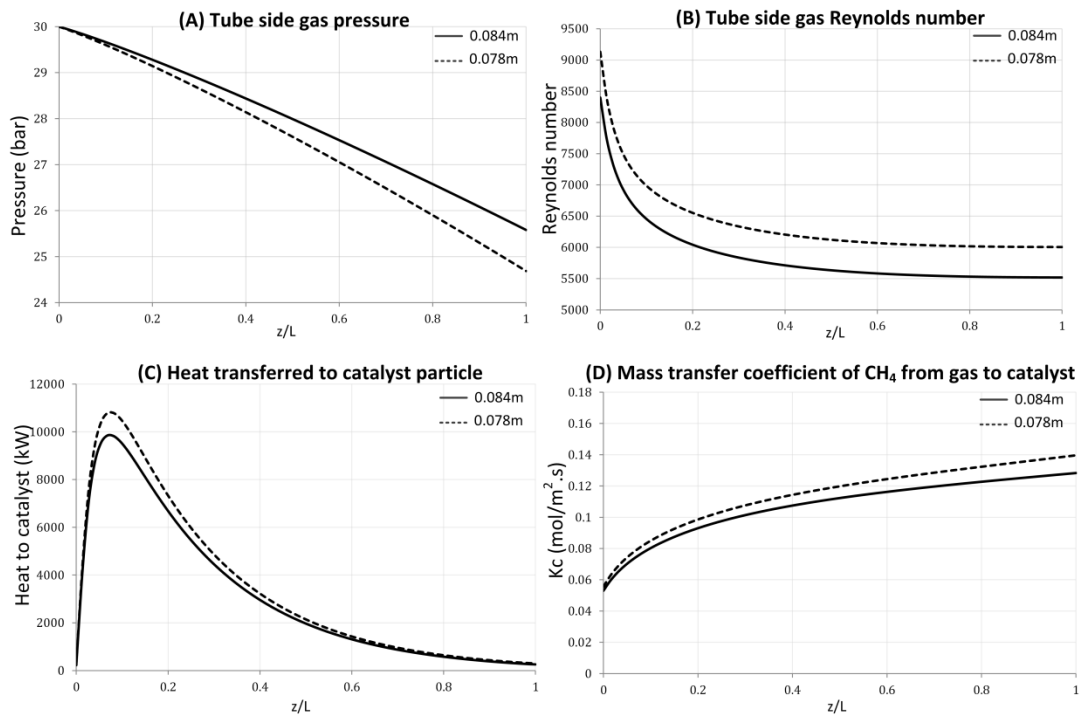


Figure 43: Effect of tube diameter on (A) tube gas phase pressure, (B) tube gas phase Reynolds number, (C) heat transferred from gas to catalyst and (D) mass transfer coefficient of CH₄ from gas to catalyst

Table 12: Effect of RSC diameter on design and operating parameters

RSC diameter	4.6 m	3.5 m
Number of tubes	138	104
NG feed per tube (mol/s)	4.20	5.58
CSA (m ²)	0.0055	0.0055
Superficial velocity (inlet) (m/s)	1.57	2.10

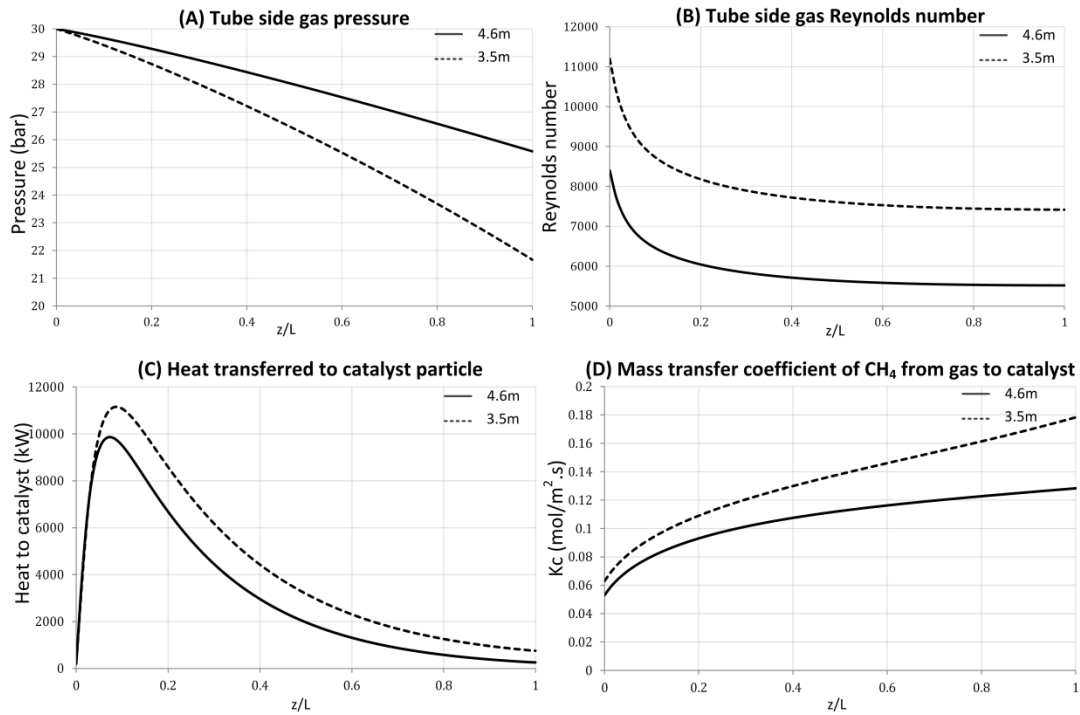


Figure 44: Effect of RSC diameter on (A) tube gas phase pressure, (B) tube gas phase Reynolds number, (C) heat transferred from gas to catalyst and (D) mass transfer coefficient of CH_4 from gas to catalyst

5.3 Conclusions

In this study, a base-case design was established for the integrated system to be used with a biomass gasifier. Furthermore, optimal designs for the integrated system were explored using both deterministic and meta-heuristic techniques. The optimal solutions obtained using both the methods showed significant improvement in the capital cost by as much as 40%. Furthermore, the use of using parallel computing with meta-heuristic techniques showed improvement in computation time by 50%. Among the meta-heuristic methods considered in this study, PSO was found to be inherently faster than DE that allowed using more number of particles in the search space, thus leading to better solutions. The evolutionary algorithms expend a lot of time towards the end finding the optimum and the classical optimization techniques should be used wherever applicable. However, methods like DE and PSO are useful when good initial guesses are not known, provided sufficient computing power is available, and when the deterministic techniques are difficult to implement and initialize. The results of the meta-heuristic methods can then be used as initial guesses for the NLP solver.

5.4 References

- [1] J. H. Ghouse, D. Seepersad, and T. A. Adams, “Modelling, simulation and design of an integrated radiant syngas cooler and steam methane reformer for use with coal gasification,” *Fuel Process. Technol.*, vol. 138, pp. 378–389, 2015.
- [2] “gPROMS.” Process Systems Enterprise.
- [3] K. Price, R. M. Storn, and J. A. Lampinen, *Differential evolution: a practical approach to global optimization*. Springer Science & Business Media, 2006.
- [4] M. Gendreau and J.-Y. Potvin, *Handbook of metaheuristics*, vol. 2. Springer, 2010.

CHAPTER 6

Conclusions and Recommendations

6.1 Conclusions

In this thesis, the technical feasibility of integrating two independent and complex processes; gasification and steam reforming of methane, for specific application in polygeneration of synthetic fuels, chemicals and electricity was studied. The genesis of this idea was in the seminal work done by Adams and Barton [1] in 2009 in which they concluded that the proposed integration increased the total plant efficiency by 2% points. However, in their study, the design and feasibility of operating such an integrated system was not studied in any level of detail. This thesis has conclusively shown that the proposed integration is not only feasible but has also established designs for the proposed system by employing mathematical models based on first-principles.

The first step in developing a mathematical model for the proposed integrated system was to develop a model for the catalytic steam reforming process that allowed tracking of the spatial and temporal variations at the particle level. The model developed in this work for the steam methane reforming process eliminated the need for experiments to find a catalyst-specific effectiveness factor that is commonly used to account for diffusional limitations. The model instead used catalyst properties (particle diameter, porosity, tortuosity and density) that are generally provided by the vendor to model the heterogenous system. Also, the common assumption of an isothermal catalyst particle for steam reforming was excluded given the requirement to study the operational feasibility of the proposed system. The model was validated with four independent data sets pertaining to industrial reformers – a rarity in similar works in the literature, and the model prediction ranged from an accurate prediction to a maximum relative error of 5.2% in predicting the methane conversion. The model also highlighted the importance of tracking the catalyst core temperature for transient modes of operation. For example, a simulated disturbance in inlet steam supply showed that the catalyst core temperatures can fluctuate by as much as 44 K in a span of 3 minutes from the time of disturbance. This ability to track catalyst core temperature is a significant advantage given online measurement is unavailable or rather, impossible to measure.

The reforming model was then coupled with the model developed for the radiant syngas cooler of an entrained-bed gasifier. The model for the radiant cooler was also validated with the available data from literature. The model validation for the independent systems (reforming and radiant cooler) was critical because experimental data for the integrated system is currently unavailable but the validation was important given the objective of this thesis was to study the technical feasibility of the proposed integrated system. Also, due to the novelty of the proposed integrated system, design heuristics were established

so as to find working base-case designs assuming a retro-fit approach to existing gasifiers initially. Two different flow configurations were studied (co-current and counter-current) and each had their respective advantages and disadvantages. While both designs were able to achieve a methane conversion of 80%, the counter-current design not only processed 10% more natural gas owing to the constant temperature gradient throughout the length of the reactor but also provided 25% more cooling duty. However, the disadvantage was the high maximum tube wall temperature for the counter current design (1334 K in one case- study) when compared to the co-current design.

Though both the co-current and counter-current designs showed promise at steady state, the comprehensive transient study done in this work showed that the co-current design will be the preferred choice if the system is required for a truly flexible polygeneration plant that can change its capacity and product portfolio. The proximity of the tube wall temperature to the maximum allowable limit of 1350 K limited the counter-current design to accommodate transitions to new operating steady-states or its ability to handle disturbances. Even under open loop, the co-current design safely transitioned to a new steady-state when the reformer feed was reduced by 25%. This transition helped change the H₂/CO ratio of the blended syngas and also reduce the syngas available for DME and FT synthesis by 15% and 30% respectively.

Three key results emerged from this study: (i) the integration helped avoid substantial CO₂ emissions (12.5 g-CO₂ per mole of CH₄ processed for 80% methane conversion) in a polygeneration plant that used an external reformer in place of the integrated system; (ii) the integrated system provided flexibility such that the blended syngas H₂/CO ratio could be altered from 1.1 to 6 by simply changing the blending strategy for the individual syngas streams; (iii) the flexibility in capacity and H₂/CO ratio could be further altered by transitioning to a new operating steady-state. Furthermore, the safe operability of the co-current design was established by simulating a cold start-up of the integrated system.

The versatility of the integrated system was demonstrated by extending the design to a biomass based gasifier. A base-case design (co-current) was established using the design heuristics developed in this work. One of the limitations of the base-case designs was that the resulting designs were sub-optimal. Therefore, to understand the efficacy of the design procedures, a formal optimization methodology was employed to determine optimal designs using both deterministic and stochastic techniques. The results showed that the base-case designs were very similar to the optimal designs when a retro-fit approach was taken (shell diameter and refractory thickness were fixed). This showed that the heuristics developed in this work were very good and yielded near optimal designs. However, improvement in capital cost by as much as 40% was realised when a

new design was desired without retro-fit constraints. Furthermore, this work also demonstrated that stochastic techniques like PSO and DE can be employed using parallel computing on complex multi-scale models to get results at par with those obtained using deterministic techniques.

In summary, this thesis has not only demonstrated the operational feasibility of integrating gasification and steam methane reforming in a single unit but has also identified working designs, operating constraints and flexibility limits in terms of capacity and products. This work has also laid the groundwork necessary to study such complex heat integrated reforming systems using rigorous mathematical models for applications specific to polygeneration plants. In addition, commercialization of this technology is possible in the future as a patent (USA/Canada) has been filed to protect the intellectual property in this work [2].

6.2 Recommended Future Work

In this work, the primary focus was to demonstrate the feasibility of the proposed integrated system for a coal-based gasifier. Owing to the many advantages shown in this work for the integrated system, the design can be extended to petcoke-based gasifiers for use in polygeneration. Petcoke is a carbon intensive feedstock that is usually discarded as waste by refineries or is combusted in fired heaters. The option to use petcoke as a fuel source is limited by the strict environmental regulations as petcoke contains high levels of sulphur. However, the production of petcoke continues to rise as modern refineries process large quantities of heavy crude owing to dwindling supplies of light crudes around the world [3]. This makes it an excellent feedstock option for polygeneration especially when used in conjunction with natural gas. The rigorous models developed in this work can be used to accurately predict the system performance that would lead to more accurate prediction of plant efficiency and the net present value at the systems level.

Another possible direction for future research would be to explore the feasibility of changing the type of reformer within the shell. In this study, conventional steam reforming was studied but future work could look at extending this to include Membrane Reforming (MR) and Sorption Enhanced Reforming (SER). Both of the afore-mentioned processes aim to increase the rate of the forward reactions by decreasing the concentration of either hydrogen or carbon monoxide. In membrane reformers, hydrogen is selectively removed through a membrane, while in SER carbon monoxide is adsorbed on adsorbents like calcium oxide that is placed on the catalyst support. This will increase

the rate of the forward endothermic reactions that will further cool the shell side coal/biomass derived syngas. Furthermore, this will help increase the H₂/CO ratio of the reforming derived syngas beyond the range presented in this work. The potential disadvantage may be the reduced carbon that remains in the product syngas as carbon monoxide that may negatively impact the carbon conversion efficiency from feed to finished products at the plant level. It will be interesting to study these systems to identify the temperature limitations (especially for membrane reforming) and also compare their performance with the conventional reforming strategy used in this work.

One of the assumptions in this work is that the tubes are homogenous at any given axial position of the reactor. Though a common assumption, even for catalyst tubes placed inside a fired furnace box for conventional steam methane reformers, it is important to verify this assumption before pilot-scale studies are done. To this end, complex CFD models could be employed to study the heat distribution within the shell. The different models developed for the tube side (gas and catalyst phase) can still be used and coupled to the CFD model of the shell as gPROMS allows interfacing with commercial CFD simulation tools. Furthermore, the CFD study will help improve the design such that the heat distribution is even for all tubes within the shell.

All of the above-mentioned options focus on employing computational tools to further study or improve the integrated system. The ultimate objective should be to test the efficiency of the system by building it at a pilot-scale. Prior to this work, the proposed integrated system was a black box where the design and operating characteristics were not understood but this work has helped answer the key questions on operational feasibility and design. This was achieved by employing mathematical models and hence it is important to acknowledge that the predictions of the performance using models, however accurate, will have some level of uncertainty. It is therefore important to build the system to study the performance thoroughly before commercialization is considered. The models developed in this work could aid in the preliminary design of a pilot-scale facility and the experimental data collected will also help validate the model.

6.3 References

- [1] T. A. Adams II and P. I. Barton, "Combining coal gasification and natural gas reforming for efficient polygeneration," *Fuel Process. Technol.*, vol. 92, no. 3, pp. 639–655, Mar. 2011.
- [2] J. H. Ghouse and T. A. Adams II, "Method and Apparatus for Producing Synthesis Gas," 15/091,773.2016.
- [3] B. N. Murthy, A. N. Sawarkar, N. a. Deshmukh, T. Mathew, and J. B. Joshi, "Petroleum coke gasification: A review," *Can. J. Chem. Eng.*, vol. 92, no. 3, pp. 441–468, Mar. 2014.

APPENDIX

A.1 Physical Properties and Correlations used in the SMR model

The physical properties and correlations used in this work for the SMR model (Chapter 2) are presented in this section.

Diffusion of component i in a multicomponent mixture is given as follows [1]:

$$D_{i,m} = \frac{1-y_i}{\sum_{\substack{j=1 \\ j \neq i}}^{N_c} \frac{y_j}{D_{ij}}} \quad (\text{A.1})$$

where $D_{i,m}$ is the diffusivity of component i in the gas mixture and y is the mole fraction of the component i or j . The binary diffusivity for the pair CH_4 - i ($i=\text{H}_2\text{O}$, CO , H_2 , CO_2 , N_2) is calculated using the following relationship [2]:

$$D_{ij} = \frac{0.00266T_g^{\frac{3}{2}}}{P_g M_{ij}^{\frac{1}{2}} \sigma_{ij}^2 \Omega_D} \quad (\text{A.2})$$

where D_{ij} is the diffusion coefficient is in cm^2/s , T_g is the temperature of the gas stream in K, P_g is the pressure of the gas stream in *bar*, σ_{ij} is the characteristic length in Å , Ω_D is diffusion collision integral (dimensionless) defined as [1]:

$$\Omega_D = \frac{1.06036}{\left(\frac{kT_g}{\sqrt{\epsilon_i \epsilon_j}}\right)^{0.15610}} + \frac{0.1930}{\exp\left(0.47635 \left(\frac{kT_g}{\sqrt{\epsilon_i \epsilon_j}}\right)\right)} + \frac{1.03587}{\exp\left(1.52996 \left(\frac{kT_g}{\sqrt{\epsilon_i \epsilon_j}}\right)\right)} + \frac{1.76474}{\exp\left(3.89411 \left(\frac{kT_g}{\sqrt{\epsilon_i \epsilon_j}}\right)\right)} \quad (\text{A.3})$$

where k is the boltzmanns constant and ϵ is the characteristic Lennard-Jones energy (dimensionless) and

$$M_{AB} = \frac{2}{\frac{1}{M_A} + \frac{1}{M_B}} \quad (\text{A.4})$$

where M_A, M_B are molecular weights of A and B . The binary diffusivity for other component pairs are estimated with the corresponding equations described below and data for parameters a , b , c and d in equation A.5, A.6 and A.7 is given in Table A.1 [3]:

$$D_{ij} = \left(\frac{aT_g^b}{P_g} \right) \left(\ln \left(\frac{c}{T_g} \right) \right)^{-2d} \exp \left(-\frac{e}{T_g} - \frac{f}{T_g^2} \right) \quad (\text{A.5})$$

$$D_{ij} = \frac{b}{P_g} \quad (\text{A.6})$$

$$D_{ij} = \frac{aT_g + b}{P_g} \quad (\text{A.7})$$

where D_{ij} is in cm^2/s , T_g is in K and P_g is in bar .

Table A. 1 - Binary diffusivity constants for component pairs

Component Pair	a	b	c	d	e	f	Equation
$H_2 - CO$	15.39E-3	1.548	0.316E8	1	-2.80	1067	A.5
$H_2 - CO_2$	3.14E-5	1.75	-	0	11.7	0	A.5
$H_2 - H_2O$	-	1.020	-	-	-	-	A.6
$H_2 - N_2$	6.007E-3	-0.99311	-	-	-	-	A.7
$CO - CO_2$	3.15E-5	1.57	-	0	113.6	0	A.5
$CO - H_2O$	0.187E-5	2.072	-	0	0	0	A.5
$CO - N_2$	0	0.322	-	-	-	-	A.7
$CO_2 - H_2O$	9.24E-5	1.5	-	0	307.9	0	A.5
$CO_2 - N_2$	3.15E-5	1.57	-	0	113.6	0	A.5
$H_2O - N_2$	0.187E-5	2.072	-	0	0	0	A.5

The effective diffusivity of a component inside the catalyst pores is defined as [1]:

$$D_{e,i,mix} = \frac{D_{i,m}\theta_c}{\tau} \quad (\text{A.8})$$

where $D_{e,i,mix}$ is the effective diffusivity of component i in a multi-component mixture, θ_c is the catalyst porosity (dimensionless) and τ is the tortuosity (dimensionless) of the catalyst. A porosity $\theta = 0.519$ and tortuosity of $\tau = 2.74$ has been used in the current work, which is appropriate for industrial SMR nickel-alumina catalysts [4].

The specific heat capacity of the gas mixture is computed as follows [1]:

$$C_{p,mix} = \sum_{i=1}^{N_c} C_{p_i} y_i \quad (\text{A.9})$$

where $C_{p,mix}$ is the specific heat capacity of the multicomponent mixture and C_{p_i} is the specific heat capacity of component i in $cal/mol K$ computed using the following

relationship and data for parameters a, b, c and d in equation A.10 is given in Table A.2 [1].

$$C_{p_i} = a + bT + cT^2 + \frac{d}{T^2} \quad (\text{A.10})$$

Table A. 2 - Specific heat capacity constants for components [1]

Component	a	b	c	d
CH_4	5.34	0.0115	0	0
H_2O	8.22	0.00015	1.34E-6	0
CO	6.6	0.0012	0	0
H_2	6.62	0.00081	0	0
CO_2	10.34	0.00274	0	-195500
N_2	6.50	0.001	0	0

The gas mixture viscosity is computed using the following correlation[2]:

$$\mu_g = \sum_{i=1}^{N_c} \frac{(y_j \mu_i)}{\sum_{j=1}^{N_c} y_j \left(\frac{M_j}{M_i}\right)^{0.5}} \quad (\text{A.11})$$

where μ_g is the gas mixture viscosity, μ_i is the viscosity of component i in Ns/m^2 and M is the molecular weight of component i or j . The viscosity of the component is computed using the following relationship and data for parameters a, b, c and d in equation A.12 is given in Table A.3 [1]:

$$\mu_i = \frac{aT_g^b}{1 + \frac{c}{T_g} + \frac{d}{T_g^2}} \quad (\text{A.12})$$

Table A. 3- Viscosity constants for components [1]

Component	a	b	c	d
CH_4	5.2546E-7	0.59006	105.67	0
H_2O	1.7096E-8	1.1146	0	0
CO	1.127E-6	0.5338	94.7	0
H_2	1.797E-7	0.685	-0.59	140
CO_2	2.148E-6	0.46	290	0
N_2	6.5592E-7	0.6081	54.714	0

The gas mixture thermal conductivity is computed using the following correlation[2]:

$$\lambda_g = \sum_{i=1}^{N_c} \frac{y_i \lambda_i}{\sum_{j=1}^{N_c} y_j A_{ij}} \quad (\text{A.13})$$

where λ_g is the thermal conductivity of the gas mixture, λ_i is the thermal conductivity of the component i in $w/m K$ and A_{ij} is the binary interaction parameters computed using Mason and Saxena's method [2]. The thermal conductivity of component i is computed using the following relationship and data for parameters a, b, c and d in equation A.14 is given in Table A.4 [1]:

$$\lambda_i = \frac{aT_g^b}{1 + \frac{c}{T_g} + \frac{d}{T_g^2}} \quad (\text{A.14})$$

Table A. 4-Thermal conductivity constants for components [1]

Component	a	b	c	d
CH_4	8.3983E-6	1.4268	-49.654	0
H_2O	6.204E-6	1.3973	0	0
CO	5.9882E-4	0.6863	57.13	501.92
H_2	2.653E-3	0.7452	12	0
CO_2	3.69	-0.3838	964	1.86E6
N_2	3.3143E-4	0.7722	16.323	373.72

The physical and thermal properties for the solid catalyst used in SMR reactors are presented in Table A.5:

Table A. 5-Properties for solid catalyst

Parameter	Value
$D_p (m)$	0.017
$\theta_c (dimensionless)$	0.519 [4]
$\tau (dimensionless)$	2.74 [4]
$\rho_c (Kg/m^3)$	2355.2 [5]
$C_{p_c} (J/Kg K)$	1107 [6]
$\lambda_c (w/m K)$	0.3489 [7]

The most widely used tubes in steam reforming process are austenitic cast steel tubes [8]. The physical and thermal properties for cast steel tubes made up of alloy IN 519 has been used in this work and tabulated in Table A.6 [9]:

Table A. 6- Tube material properties [9]

Parameter	Value
$\rho_t (Kg/m^3)$	7880
$C_{p_t} (J/Kg K)$	741
$\lambda_t (w/m K)$	28.5

A.2 Gas Emissivity Calculations for the RSC Model

The emissivity of the gas on the shell side used in Chapter 3 is outlined below.

The emissivity of carbon dioxide and water vapour is given by the following equation [10]:

$$\epsilon_i = \exp[\sum_{i=0}^M \sum_{j=0}^N c_{ij} \left(\frac{T_s}{T_o}\right)^j (\log(p_i L))^i] \left\{ 1 - \frac{(a-1)(1-P_E)}{a+b-1+P_E} \exp[-c(\log(P_i L)_m)^2] \right\} \quad (A.15)$$

where p_i is the partial pressure of component i , L is the mean beam length and c_{ij} , a , b , c and P_E are parameters.

The values for c_{ij} for water vapour and carbon dioxide are given in Table A.7 and Table A.8 respectively.

Table A.7: Water Vapour (m=2 and n=2 where m represents rows and n represents columns)

	0	1	2
0	-2.2118	-1.1987	0.035596
1	0.85667	0.93048	-0.14391
2	-0.10838	-0.17156	0.045915

Table A.8: Carbon dioxide (m=2 and n=3)

	0	1	2	3
0	-3.9893	2.7669	-2.1081	0.39163
1	1.2710	-1.1090	1.0195	-0.21897
2	-0.23678	0.19731	-0.19544	0.044644

The other parameters in equation A.15 are defined as follows:

Table A.9: Parameters for equation A.15

Parameter	Water Vapour	Carbon Dioxide
P_E	$\frac{\left(p_{total} + \frac{2.56p_{H_2O}}{\sqrt{\frac{T_s}{T_o}}} \right)}{p_o}$	$\frac{p_{total} + 0.28p_{CO_2}}{p_o}$
$(p_iL)_m$	$13.2 \left(\frac{T_s}{T_o} \right)^2$	$0.225 \left(\frac{T_s}{T_o} \right)^2$
a	$1.88 - 2.053 \log \left(\frac{T_s}{T_o} \right)$	$1 + \frac{0.1}{\frac{T_s}{T_o}^{1.45}}$
b	$\frac{1.10}{\frac{T_s}{T_o}^{1.4}}$	0.23
c	0.5	1.47

where $T_o = 1000 K$ and $p_o = 1 bar$.

For carbon monoxide, the emissivity is calculated using the following equation [11]:

$$\log \epsilon_{CO} = \frac{a + \sum_{i=1}^3 [b_i T_s^i + d_i (\log p_{CO} L)^i]}{1 + \sum_{i=4}^6 [b_i T_s^{i-3} + d_i (\log p_{CO} L)^{i-3}]} \quad (A.16)$$

The constants for equation A.16 are given in Table A.10 [11].

Table A.10: Constants for computing the emissivity of carbon monoxide

Parameter	Value
a	-2.429
b_1	1.992×10^{-3}
b_2	-1.072×10^{-6}
b_3	0
d_1	2.662×10^{-1}
d_2	1.468×10^{-1}
d_3	0

b_4	8.726×10^{-5}
b_5	0
b_6	0
d_4	8.134×10^{-2}
d_5	-1.926×10^{-2}
d_6	0

The combined emissivity including water vapour, carbon dioxide and carbon monoxide is given by the following equation:

$$\epsilon_g = \epsilon_{CO_2} + \epsilon_{H_2O} + \epsilon_{CO} - \Delta\epsilon \quad (\text{A.17})$$

where $\Delta\epsilon$, that accounts for the band overlap between carbon dioxide and water vapour, and is given by [10]:

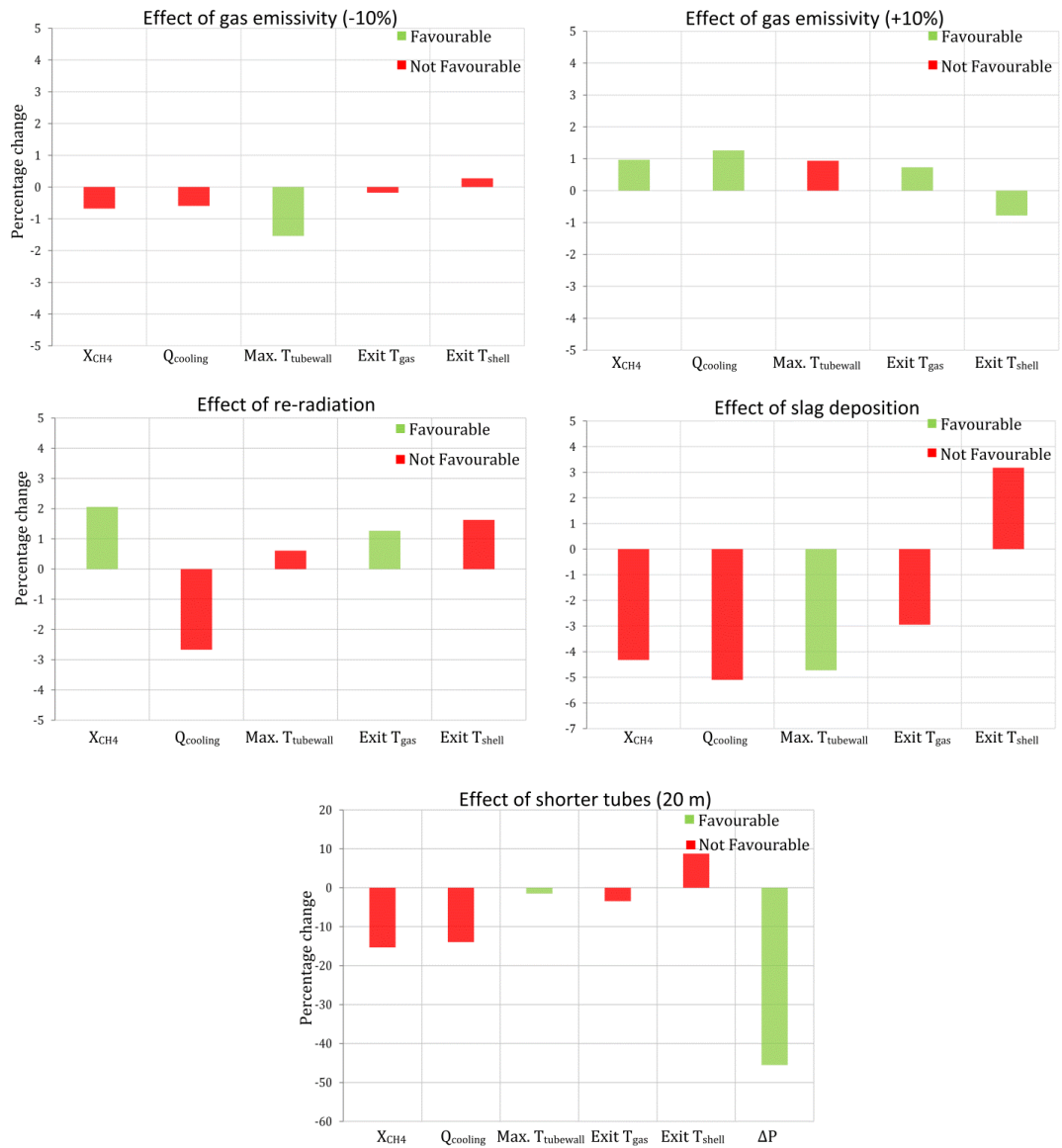
$$\Delta\epsilon = \left(\frac{\left(\frac{p_{H_2O}}{p_{H_2O} + p_{CO_2}} \right)}{10.7 + 101 \left(\frac{p_{H_2O}}{p_{H_2O} + p_{CO_2}} \right)} - 0.0089 \left(\frac{p_{H_2O}}{p_{H_2O} + p_{CO_2}} \right)^{10.4} \right) (\log(p_{H_2O} + p_{CO_2}) L)^{2.76} \quad (\text{A.18})$$

The total gas phase emissivity that includes the emissivity of the particle is calculated as follows:

$$\epsilon_{g,total} = \epsilon_g + \epsilon_p - (\epsilon_g \epsilon_p) \quad (\text{A.19})$$

The particle emissivity used in this work is 0.3 [12]. It should be noted that the gas emissivity was calculated at the inlet conditions and assumed constant along the entire length of the RSC.

A.3 Sensitivity Analysis on Model Parameters for Counter-current Configuration



A.4 Procedure to Link Matlab with gPROMS (v4.0) Using gO:Matlab

Requirements:

1. **gPROMS v4.0 (or the current version)** should be installed on your computer. Please know the version (32/64 bit) that is currently installed.
2. **MATLAB 2014** or previous versions. NOTE: **gPROMS v4.0 release notes** states that it is compatible with MATLAB 2014 (both 32/64 bit) but previous versions like gPROMS 3.7 or older did not support 64 bit. However, if gPROMS that is installed is 32 bit, then MATLAB 32 bit installation is required and same goes for the 64 bit version.

Procedure (for 32 bit version):

1. Setting the **SYSTEM ENVIRONMENT VARIABLE:**

Click start, in the search bar search for “environment variable” and click ENTER. Click on “EDIT THE SYSTEM ENVIRONMENT VARIABLES” option. Click on “ENVIRONMENT VARIABLES” and under the system variables, check if the variable GPROMSHOME is set to the path (during installation): “*C:\Program Files (x86)\PSE\gPROMS-core_4.0.0.54901*”. If not, set it to the required path.

2. Setting the **PATH VARIABLE:**

Under the SYSTEM ENVIRONMENT VARIABLES (specified in 1), select the variable called as “PATH”. You will notice that the variable value refers to a lot of other programs installed on your computer. Add the following path to this list using a semi-colon at the end of the previous program path: “*C:\Program Files (x86)\PSE\gPROMS-core_4.0.0.54901\bin*”.

3. Required changes within **MATLAB:**

In MATLAB, click on “SET PATH” under the “HOME” tab. Click on “ADD FOLDER” and add the following path: “*C:\Program Files (x86)\PSE\ModelBuilder_4.0.0.54901\gOMATLAB*”.

Things to know:

1. Check release notes for gPROMS

It is good practice to read the release notes when installing new versions of gPROMS. This document provides details of gPROMS compatibility with other softwares.

2. Older installed versions of gPROMS can cause problems

Please check while setting up the GPROMSHOME and PATH variables that they are pointing to the most recent version of gPROMS. Note that even when older versions of gPROMS are uninstalled, the PATH variable will still include references to the older versions. Remove the older references for this variable.

Testing successful installation

1. In the MATLAB command window, type the following command and press enter:

gOMATLAB('startONLY')

2. If the installation was successful, you should get “ans=1”. Usually, when using any gOMATLAB command, if you get a value other than 1 it signals an error in executing that particular command. Refer to the gO:MATLAB documentation for more details on error diagnostics.
3. If the installation was unsuccessful, you will probably encounter the following error:

Invalid MEX-file <mexfilename>:
The specified module could not be found.

This error means compatibility issues with the .dll file in gPROMS folder (C:\Program Files (x86)\PSE\ModelBuilder_4.0.0.54901\gOMATLAB) and MATLAB. Please check if both, gPROMS and MATLAB, are 32 bit or 64 bit.

4. If the error is unresolved, please check whether the SYSTEM ENVIRONMENT VARIABLES (GPROMSHOME AND PATH) has been set to the correct path. Again, make sure that older references under the PATH variable have been deleted.

References

- [1] R. Perry and D. Green, *Perry's chemical engineers' handbook*, 8th ed. New York: McGraw-Hill, 2008.
- [2] R. C. Reid, J. M. Prausnitz, and B. E. Poling, *The properties of gases and liquids*, 4th ed. McGraw-Hill Book Company, NY, 1987.
- [3] T. A. Adams II and P. I. Barton, "A dynamic two-dimensional heterogeneous model for water gas shift reactors," *Int. J. Hydrogen Energy*, vol. 34, no. 21, pp. 8877–8891, Nov. 2009.
- [4] A. D. Nandasana, A. K. Ray, and S. K. Gupta, "Dynamic Model of an Industrial Steam Reformer and Its Use for Multiobjective Optimization," *Ind. Eng. Chem. Res.*, vol. 42, no. 17, pp. 4028–4042, Aug. 2003.
- [5] J. Xu and G. F. Froment, "Methane steam reforming: II. Diffusional limitations and reactor simulation," *AIChE J.*, vol. 35, no. 1, pp. 97–103, Jan. 1989.
- [6] E. L. G. Oliveira, C. a. Grande, and A. E. Rodrigues, "Methane steam reforming in large pore catalyst," *Chem. Eng. Sci.*, vol. 65, no. 5, pp. 1539–1550, Mar. 2010.
- [7] M. Defalco, L. Dipaola, and L. Marrelli, "Heat transfer and hydrogen permeability in modelling industrial membrane reactors for methane steam reforming," *Int. J. Hydrogen Energy*, vol. 32, no. 14, pp. 2902–2913, Sep. 2007.
- [8] J. Łabanowski, "Evaluation of reformer tubes degradation after long term operation," *J. Achiev. Mater. Manuf. Eng.*, vol. 43, no. 1, pp. 244–251, 2010.
- [9] "IN-519 cast chromium-nickel-niobium heat-resisting steel," *INCO Databook*, 1976.
- [10] C. E. Baukal, *Heat Transfer In Industrial Combustion*. New York: CRC Press, 2000.
- [11] A. K. Mehrotra, K. Karan, and L. A. Behie, "Estimate Gas Emissivities for Equipment and Process Design," *Chem. Eng. Prog.*, vol. 91, pp. 70–77, 1995.
- [12] H. Watanabe and M. Otaka, "Numerical simulation of coal gasification in entrained flow coal gasifier," *Fuel*, vol. 85, pp. 1935–1943, 2006.